ELECTRICAL AND THERMAL PROPERTIES OF YTTRIA-STABILISED ZIRCONIA (YSZ)-BASED CERAMIC MATERIALS

A thesis submitted to The University of Manchester for the degree of

Doctor of Philosophy

in the Faculty of Engineering and Physical Science

2011

Fan YANG

Materials Science Centre, School of Materials

List of Contents

Word count: 40,352

Abstract

Electrical and Thermal Properties of Yttria-Stabilised Zirconia (YSZ)-based Ceramic Materials

Fan Yang

The University of Manchester for the degree of Doctor of Philosophy in the Faculty of Engineering and Physical Sciences

2011

Electrical and thermal conductivities of the yttria-stabilised zirconia/alumina (YSZ/Al_2O_3) composites and the yttria-zirconia-ceria ($YSZ\text{-}CeO_2$) solid solutions are studied in this thesis.

The electrical conductivity of the YSZ/Al_2O_3 composites decreases with an increase in the volume fraction of Al_2O_3 and exhibits typical percolation behaviour. The electrical conductivity of the YSZ/Al_2O_3 interface is higher than that of the YSZ grain boundary, but lower than that of the YSZ grains.

The thermal conductivity of the YSZ/Al_2O_3 composites increases with an increase in the Al_2O_3 volume fraction, and it can be fitted well to the Maxwell theoretical model, which indicates the absence of obvious interfacial thermal resistances in the composites. The low interfacial thermal resistance of the YSZ/Al_2O_3 interface is due to the "clean" and coherent nature of the YSZ/Al_2O_3 interface, along with the small difference between the elastic properties of YSZ and Al_2O_3.

The electrical conductivity of the $[(ZrO_2)_{1-x}(CeO_2)_x]_{0.92}(Y_2O_3)_{0.08}$ ($0 \leq x \leq 1$) solid solutions has a "V-shape" variation as a function of the mole ratio of CeO_2 (x). In the ZrO_2-rich region ($x < 0.5$), CeO_2 doping increases the concentration of defect associates which limits the mobility of the oxygen vacancies; in the CeO_2-rich region ($x > 0.5$), the increase of x increases the lattice parameter, which enlarges the free channel for oxygen vacancy migration. A comparison of the $YSZ\text{-}CeO_2$ solid solutions with the $YSZ\text{-}HfO_2$ series indicates the ionic radius of the tetravalent dopant determines the composition dependence of the ionic conductivity of the solid solutions.

The thermal conductivity of the $[(ZrO_2)_{1-x}(CeO_2)_x]_{0.92}(Y_2O_3)_{0.08}$ ($0 \leq x \leq 1$) solid solutions also has a "V-shape" variation as a function of the mole ratio of CeO_2 (x), which indicates an incorporation of Zr^{4+} and Ce^{4+} can effectively decrease the thermal conductivity of the end members YSZ and yttria-doped ceria (YDC). In the ZrO_2-rich region ($0 \leq x \leq 0.5$), the thermal conductivity is almost temperature independent; in the CeO_2-rich region ($0.5 \leq x \leq 1$), it decreases obviously with increasing temperature. By calculating the phonon scattering coefficients, it is concluded that the composition dependence of the thermal conductivity in the ternary solid solutions is dominated by the mass difference between Zr and Ce at the cation sites, whereas the temperature dependence is determined by the order/disorder of oxygen vacancies at the anion sites.

Declaration

No portion of the work referred to in this thesis, "**Electrical and thermal properties of yttria-stabilised zirconia (YSZ)-based ceramic materials**", has been submitted in support of an application for another degree or qualification of this or any other university or other institute of learning.

Copyright statement

i. The author of this thesis (including any appendices and/or schedules to this thesis) owns certain copyright or related rights in it (the "Copyright") and s/he has given The University of Manchester certain rights to use such Copyright, including for administrative purpose.

ii. Copies of this thesis, either in full or in extracts and whether in hard or electronic copy, may be made only in accordance with the Copyright, Designs and Patents Act 1988 (as mended) and regulations issued under it or, where appropriate, in accordance with licensing agreements which the University has from time to time. This page must form part of any such copies made.

iii. The ownership of certain Copyright, patents, designs, trade marks and other intellectual property (the "Intellectual Property") and any reproductions of copyright works in the thesis, for example graphs and tables ("Reproductions"), which may be described in this thesis, may not be owned by the author and may be owned by third parties. Such Intellectual Property and Reproductions cannot and must not be made available for use without the prior written permission of the owner(s) of the relevant Intellectual Property and/or Reproductions.

iv. Further information on the conditions under which disclosure, publication and commercialization of this thesis, the Copyright and any Intellectual Property and/or Reproductions described in it may take place is available in the University IP Policy (see http://campus.manchester.ac.uk/medialibrary/policies/intellectual-property.pdf), in any relevant Thesis restriction declarations deposited in the University Library, The University Library's regulations (see

http://www.manchester.ac.uk/library/aboutus/regulations) and in The University's policy on Presentation of Theses.

Acknowledgement

I would like to express my sincere gratitude to my supervisor, Professor Ping Xiao, for his supervision and support on my PhD research, and for his patience and encouragement when I was going through tough times. His enthusiasm and motivation on scientific research always impress me and give me a deep and long-term influence on my determination of being a researcher. Also I would like to thank him for the financial support during my PhD studies.

I would like to give special thanks to my senior colleague Dr. Xiaofeng Zhao for his kind help on my experiments and valuable suggestion on my project. He passes his experiences uncensoredly, even in a tiny aspect like polishing substrates, to me – a newbie of ceramic research. He never laughs at my silly questions; instead, he always encourages my ideas and gives critical suggestions. He is more like the second supervisor to me and he has set me an example of being a good researcher.

I would like to thank the technician staffs in Materials Science Centre for their help on my experiments, especially Mr. Andy Wallwork on laser flash technique, Mr. Andrew Forrest on specific heat capacity measurement, Dr. Judith Shackleton and Dr. Gary Harrison on X-ray diffraction test and analysis, Mr. Michael Faulkner on SEM and Mr. Kenneth Gyves on micro-indentation.

My thanks also go to all the members of the ceramic coating group and all the friends of Methodist International House (MIH). Your names are not listed here but they are imprinted in my heart forever. With your companies, I am able to finish my study and live happily in this country. I am proud to say friendship is the most precious gains I obtain here.

Last but not least, I would like to thank my dearest parents for their everlasting love and support. Thank you for bringing me to this world, to experience happiness and sadness, to share laughter and tear, and to see people coming and going in my life.

List of figures

Chapter 1

Chapter 2

Chapter 3

Chapter 4

Chapter 5

Chapter 6

List of tables

List of Publications

1. **F. Yang**, X. Zhao and P. Xiao, Bulk conduction and relaxation in $[(ZrO_2)_{1-x}(CeO_2)_x]_{0.92}(Y_2O_3)_{0.08}$ ($0 \leq x \leq 1$) solid solutions at intermediate temperatures, Journal of Power Sources **196** (2011) 4943-4949.
2. **F. Yang**, X. Zhao and P. Xiao, Thermal conductivities of YSZ/Al_2O_3 composites, Journal of the European Ceramic Society **30** (2010) 3111-3116.
3. **F. Yang**, X. Zhao and P. Xiao, Electrical properties of YSZ/Al_2O_3 composite and YSZ/Al_2O_3 interface studied by impedance spectroscopy and finite element modelling, Solid State Ionics **181** (2010) 783-789.
4. X. Zhao, **F. Yang** and P. Xiao, Stress-enhanced growth rate of alumina scale formed on FeCrAlY alloy, Scripta Materialia **63** (2010) 117-120.
5. **Yang F**, Shinmi A and Xiao P, Electrical and dielectric properties of thermally grown oxide (TGO) on Fecralloy substrate studied by impedance spectroscopy, Advanced Ceramic Coatings and Interfaces IV **30** (2009) 87-95.
6. Tan J, Meadows P J, Zhang D, Chen X, Lopez-Honorato E, Zhao X, **Yang F**, Abram T and Xiao P, Young's modulus measurements of SiC coatings on spherical particles by using nanoindentation, Journal of Nuclear Materials **393** (2009) 22-29.
7. **Yang F** and Xiao P, Nondestructive evaluation of thermal barrier coatings using impedance spectroscopy, International Journal of Applied Ceramic Technology **6** (2009) 381-389.
8. **F. Yang**, X. Zhao and P. Xiao, Composition and temperature effect on thermal conductivities of $[(ZrO_2)_{1-x}(CeO_2)_x]_{0.92}(Y_2O_3)_{0.08}$ ($0 \leq x \leq 1$) solid solutions, Acta Materialia, Revision.

Chapter 1

Introduction

1.1 Yttria-stabilised zirconia (YSZ)

1.1.1 Crystal structure and phase transformation of YSZ

ZrO_2 is one of the most important ceramic materials because of its wide applications. Pure ZrO_2 has three polymorphs at atmospheric pressure: monoclinic (*m*) [space group $P2_1/c$], tetragonal (*t*) [space group $P4_2/nmc$] and cubic (*c*) [space group *Fm3m*], as shown in Figure 1.1 [1]. Monoclinic is the stable phase at room temperature, which transforms to tetragonal phase at about 1170 ºC. The tetragonal phase remains stable up to 2370 ºC and transforms to cubic phase, which is stable until reaching the melting point at 2680 ºC.

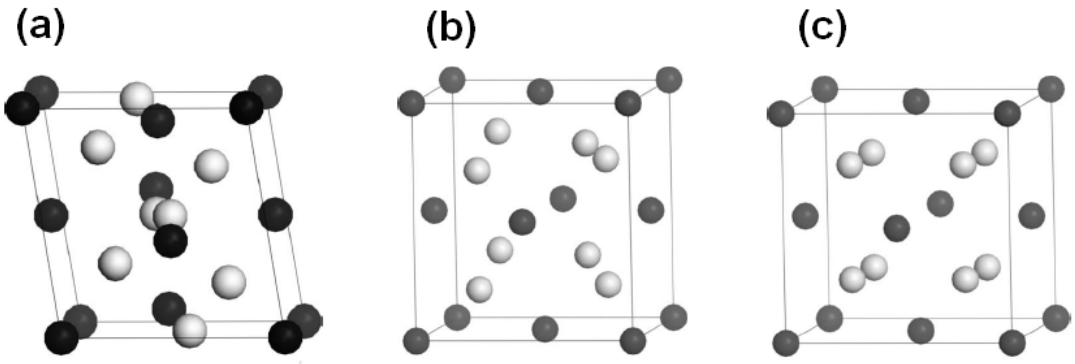

Figure 1.1 Crystal structure of ZrO_2: (a) monoclinic (b) tetragonal and (c) cubic. The grey spheres represent oxygen atoms, and the black ones represent zirconium atoms. [1]

The high temperature phases of ZrO_2 can be stabilised to room temperature by the addition of other oxides such as Y_2O_3, MgO or CaO, among which Y_2O_3 is the most commonly used stabiliser. Depending on the concentration and the type of the stabiliser, zirconia ceramics may conveniently be classified into three major types according to the crystal structure: fully stabilised zirconia (FSZ), partially stabilized zirconia (PSZ) and tetragonal zirconia polycrystals (TZP) [2]. In FSZ, zirconia is in its cubic phase, which is widely used in oxygen sensors and fuel cell electrolytes. The PSZ consists of nanosized tetragonal or monoclinic particles that have precipitated out in a cubic matrix. TZPs are monoliths of tetragonal phase, which may contain a secondary cubic phase.

Figure 1.2 shows the phase diagram of the ZrO_2-Y_2O_3 binary solid solution (zirconia-rich corner) [3]. FSZ can be obtained at room temperature with large concentration of yttria, i.e., 8 mol% Y_2O_3-stabilised zirconia (14.8 mol% $YO_{1.5}$) [4].

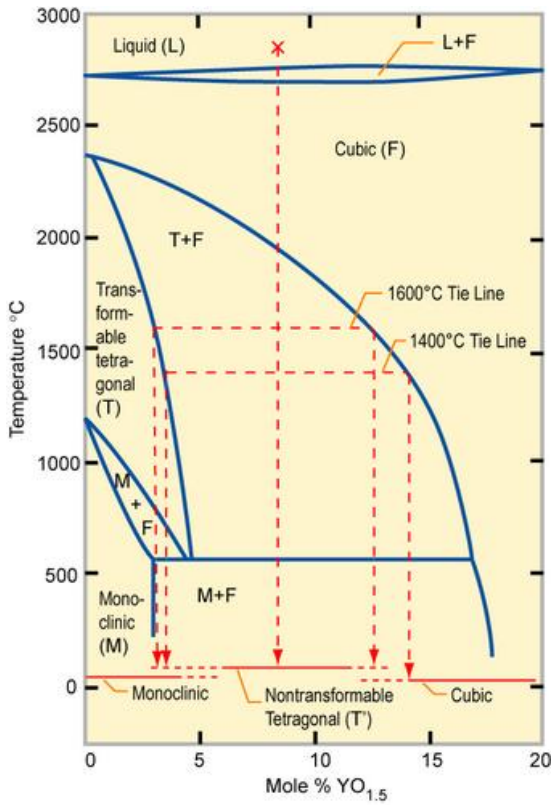

Figure 1.2 Phase diagram of the ZrO_2-Y_2O_3 binary system (the zirconia rich corner). [3]

1.1.2 Applications of YSZ

YSZ has some unique physical properties and therefore it has wide applications. For example, it can be used as implant biomaterials like tooth crowns and hip implants because of its high hardness and chemical inertness [5]. It can be used as the electrolyte material in oxygen sensors [6] or solid oxide fuel cells (SOFCs) [7, 8] due to its good ionic conductivity. It is also widely used as thermal barrier coatings (TBCs) material because of its low thermal conductivity. In the following two sessions, the two most important applications of YSZ, the SOFCs and the TBCs, are briefly introduced.

(1) Solid oxide fuel cells

Solid oxide fuel cells (SOFCs) offer a clean, low-pollution technology to electrochemically generate electricity. They provide many advantages over traditional energy conversion systems including high efficiency, reliability, modularity, fuel adaptability and very low levels of NO_x and SO_x emissions [9].

An SOFC consists of two porous electrodes separated by a dense, oxide ion conducting electrolyte, as shown in Figure 1.3 [9]. At the cathode side, oxygen reacts with incoming electrons from the external circuit to form oxygen ions, which migrate to the anode through the solid electrolyte. At the anode side, oxygen ions react with fuel, generally H_2 (and/or CO), producing water and CO_2 and liberating electrons. Electrons (electricity) flow from the anode through the external circuit to the cathode.

8 mol% YSZ is the most widely used material for the electrolyte in SOFCs because of its sufficient ionic conductivity, chemical stability and mechanical strength [9, 10]. The only deficiency of YSZ is that its ionic conductivity is not high enough to meet the demand of lower operation temperature. Therefore, modifying YSZ to increase its ionic conductivity is an important issue in SOFCs.

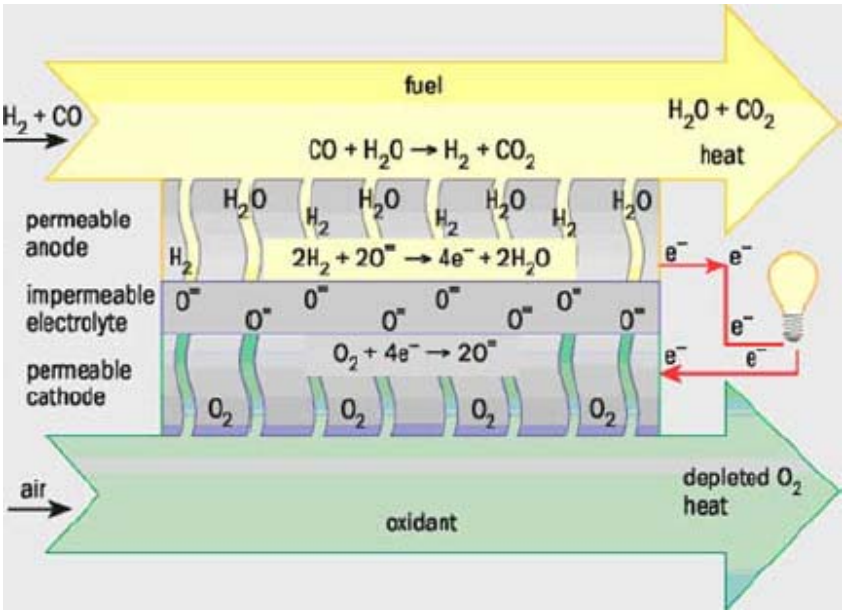

Figure 1.3 Structure and operating principle of a solid oxide fuel cell. [9]

(2) Thermal Barrier Coatings

Thermal barrier coatings (TBCs) have been widely used in the hot section of aero-turbine engines to increase turbine efficiency and to extend the life of metallic components [11-13]. TBCs have a multilayer structure, typically consisting of a ceramic topcoat, a metallic bond coat, a superalloy substrate and a thermally grown oxide (TGO) layer formed at the top coat/bond coat interface due to the oxidation of the bond coat at high temperatures. A schematic view of a TBC system, along with the requirement of each component, is shown in Figure 1.4 [14].

The function as a thermal barrier in a TBC system is fulfilled by the ceramic topcoat. The topcoat materials should be thermally insulating and therefore prohibit heat transfer from the hot gas in the engine to the surface of the coated superalloy components. 6 – 8 wt% (3.5 – 4.5 mol% Y_2O_3) YSZ is the start-of-art TBC material because it provides the best performance in high-temperature applications such as diesel engines and gas turbines [15]. It has a temperature-independent low thermal conductivity, depending on the yttria concentration and the fabrication method [16-18]. It also has a relatively high coefficient of thermal expansion, which is close to that of the nickel based superalloy [19]. Furthermore, it has been proved to have better corrosion resistance against the corrosion of Na_2SO_4 than other stabilised zirconia materials [15].

Although the thermal conductivity of YSZ is not the lowest among other oxides, in terms of the comprehensive properties, YSZ shows the best performance and it is at the moment the first choice of TBC material. The research of thermal conductivity of YSZ, e.g., the thermal conduction mechanisms, the methods to decrease the thermal conductivity, the development of double-layer topcoat (e.g., pyrochlore oxides/YSZ), etc., is a major issue in developing TBCs.

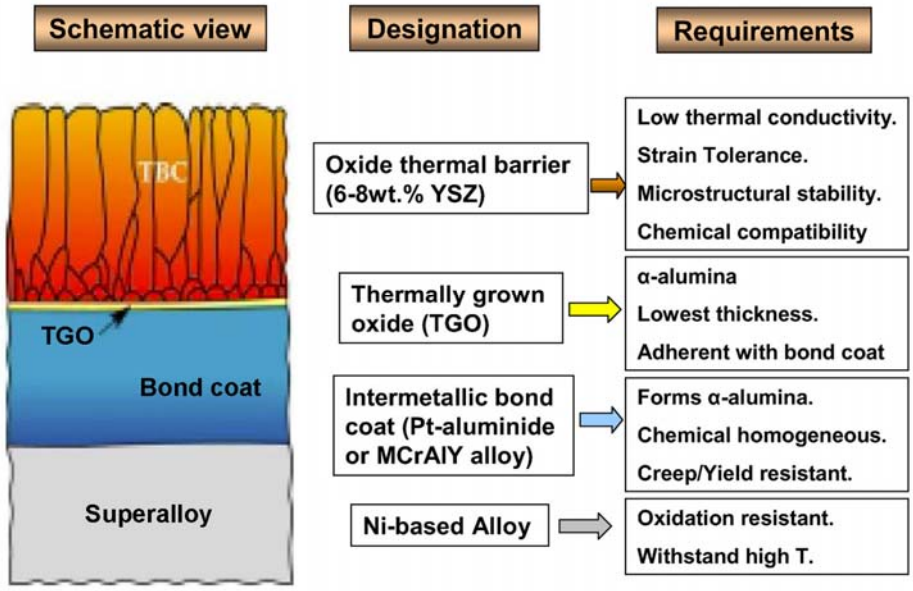

Figure 1.4 The four major elements and their requirements of a thermal barrier coating system. [14]

1.2 Goals of the dissertation

Due to its applications as an electrolyte material in SOFCs and the top coat material in TBCs, understandings on the electrical (ionic) and thermal properties of YSZ are important for a basic understanding of the functionality of SOFCs and TBCs. Therefore, all the work carried out in this thesis is related to these two properties, aiming to further understand the fundamentals of conduction mechanisms of YSZ-based ceramic materials.

Two material systems are chosen to investigate in this thesis. One is the YSZ/Al_2O_3 composites. The reasons for choosing this system are: (1) YSZ and Al_2O_3 are the most

widely used ceramic materials and their composites may combine the merits of YSZ and Al_2O_3 and have potential in practical applications; (2) YSZ and Al_2O_3 are immiscible to each other and can generate clean heterogeneous YSZ/Al_2O_3 interface, which makes the system suitable for fundamental studies of the dual-phase composites; (3) Al_2O_3 is the main composition of the TGO, which is a critical component of TBCs system. Our previous studies generate questions on the role of top coat/TGO interface on the thermal conduction in TBCs. YSZ/Al_2O_3 composites can be a model system to figure out the effect of the interface on the thermal conduction.

The second system is the ZrO_2-CeO_2-Y_2O_3 ternary solid solutions. This system is of our interests due to the following reasons: (1) Doped zirconia and doped ceria are the most important ionic conductors using as electrolyte materials in SOFCs. The intermixing of ZrO_2 and CeO_2 in the solid solutions does not introduce extra oxygen vacancies, which is suitable for investigating the homovalent doping effect in solid solutions; (2) Ce^{4+} is both heavier in mass and larger in size than Zr^{4+}. It is interesting to investigate how the mass and the ionic size influence the thermal conductivity of the ternary solid solutions.

The structure of the thesis is as following. In Chapter 2, the fundamentals of electrical and thermal conduction mechanisms in YSZ are reviewed, which provide basic understanding and are helpful in further discussions of the YSZ-based materials.

In Chapter 3, the electrical properties of YSZ/Al_2O_3 composites, with a focus on the YSZ/Al_2O_3 interface are studied from impedance spectroscopy coupled with finite element modelling. The thermal properties of YSZ/Al_2O_3 composites, also focusing on the YSZ/Al_2O_3 interface, are described in Chapter 4.

Chapter 5 and 6 are based on the electrical and thermal properties of the ZrO_2-CeO_2-Y_2O_3 ternary solid solutions, in which the effect of homovalent doping (intermixing of Zr and Ce) on the electrical and thermal properties is discussed.

In Chapter 7, the main results and conclusion are summarized, along with the inspirations obtained from current studies and the outlook for further research.

References

[1] X. Luo, W. Zhou, S. V. Ushakov, A. Navrotsky and A. A. Demkov, *Monocline to tetragonal transformations in hafnia and zirconia: A combined calorimetric and density functional study*, Physical Review B **80** (2009) 134119.

[2] J. Chevalier and L. Gremillard, *The tetragonal-monoclinic transformation in zirconia: Lessons learned and future trends*, Journal of the American Ceramic Society **92** (2009) 1901-1920.

[3] http://www.doitpoms.ac.uk/tlplib/fuel-cells/sofc_electrolyte.php?printable=1.

[4] K. Erich and Y. Ma, *Debye temperature, anharmonic thermal motion and oxygen non-stoichiometry in yttria stabilized cubic zirconia*, Journal of Physics: Condensed Matter **10** (1998) 3823-3832.

[5] J. Zhou, J. Mah, P. Shrotriya, C. Mercer and W. O. Soboyejo, *Contact damage in an yttria stabilized zirconia: Implications for biomedical applications*, Journal of Materials Science: Materials in Medicine **18** (2007) 71-78.

[6] W. C. Maskell, *Progress in the development of zirconia gas sensors*, Solid State Ionics **134** (2000) 43-50.

[7] T. Hibino, A. Hashimoto, T. Inoue, J. Tokuno, S. Yoshida and M. Sano, *A low-operating-temperature solid oxide fuel cell in hydrocarbon-air mixtures*, Science **288** (2000) 2031-2033.

[8] S. C. Singhal, *Solid oxide fuel cells for stationary, mobile, and military applications*, Solid State Ionics **152-153** (2002) 205-410.

[9] S. C. Singhal, *Solid oxide fuel cells*, The Electrochemical Society INTERFACE **16** (2007) 41-44.

[10] R. M. Ormerod, *Solid oxide fuel cells*, Chemical Society Reviews **32** (2003) 17-28.

[11] R. A. Miller, *Current status of thermal barrier coatings- an overview*, Surface and Coatings Technology **30** (1987) 1-11.

[12] N. P. Padture, M. Gell and E. H. Jordan, *Thermal barrier coatings for gas-turbine engine applications*, Science **296** (2002) 280-284.

[13] D.R. Clarke and C. G. Levi, *Materials design for the next generation thermal barrier coatings*, Annual Review of Materials Research **33** (2003) 383-417.

[14] X. Zhao, PhD Thesis, University of Manchester 2007.

[15] X. Q. Cao, R. Vassen and D. Stoever, *Ceramic materials for thermal barrier coatings*, Journal of the European Ceramic Society **24** (2004) 1-10.

[16] J. F. Bisson, D. Fournier, M. Poulain, O. Lavigne, R. Mevrel, *Thermal conductivity of yttria-zirconia single crystals determined with spatially resolved infrared thermography*, Journal of the American Ceramic Society **83** (2000) 1993-1998.

[17] D. R. Clarke and S. R. Phillpot, *Thermal barrier coating materials*, Materials Today **8** (2005) 22-29.

[18] X. Huang, D. Wang, M. Lamontagne and C. Moreau, *Experimental study of the thermal conductivity of metal oxides co-doped yttria stabilized zirconia*, Materials Science and Engineering B **149** (2008) 63-72.

[19] U. Schulz C. Leyens, K. Fritscher, M. Peters, B. Saruhan-Brings, O. Lavigne, J. M. Dorvaux, M. Poulain, R. Mevrel and M. Caliez, *Some recent trends in research and technology of advanced thermal barrier coatings*, Aerospace Science and Technology **7** (2003) 73-80.

Chapter 2

Literature review

PART 1. Electrical conduction mechanism of YSZ

2.1 Ionic conduction in fluorite-type oxides

The history of fast ionic conductors can be traced back to 1839, when Faraday observed high ionic conductivity in lead fluoride (PbF_2) at high temperature. Thereafter the investigation of ionic conduction in the oxides with fluorite-type structure was largely inspired. Nowadays the fluorite-type oxide ionic conductors have been widely used as electrolyte materials in solid oxide fuel cells (SOFCs), oxygen pumps and oxygen sensors [1].

2.1.1 Defect fluorite structure and defect chemistry

As illustrated in Figure 2.1, fluorite-structured oxides are of the type MO_2, where M is a tetravalent cation (Zr, Ce, etc). M atoms in a face-centered pattern contain a cube of oxygen atoms. Fluorite has a simple structure belonging to space group $Fm3m$. A structural unit cell contains fully four M and eight oxygen ions, maintaining the 1:2 stoichiometry.

When lower-valent (divalent or trivalent) oxides are doped into MO_2, the host cations are replaced by lower-valent cations, and oxygen vacancies are consequently generated in the anion sublattice to compensate the charge missing. The defect chemistry of the above solid reactions is described by the following equations:

$$XO \xrightarrow{MO_2} X_M^{''} + V_O^{\bullet\bullet} + O_O^{\times}, \tag{2.1a}$$

$$R_2O_3 \xrightarrow{MO_2} 2R_M^{'} + V_O^{\bullet\bullet} + 3O_O^{\times}, \tag{2.1b}$$

where X presents divalent metal (Ca, Mg, etc.) and R presents trivalent metal (Y, Sm, Gd, etc.).

However, due to Coulomb and elastic attractive forces between the negatively charged substitutional defects ($X_M^{''}$ or $R_M^{'}$) and the positively charged oxygen vacancies ($V_O^{\bullet\bullet}$), it is possible to form defect associates:

$$X_M^{''} + V_O^{\bullet\bullet} \rightarrow \left(X_M^{''} V_O^{\bullet\bullet}\right)^{x}, \tag{2.2a}$$

$$R_M^{'} + V_O^{\bullet\bullet} \rightarrow \left(R_M^{'} V_O^{\bullet\bullet}\right)^{\bullet}. \tag{2.2b}$$

At high dopant concentrations, more complex defect associates can be generated:

$$2R_M^{'} + V_O^{\bullet\bullet} \rightarrow \left(R_M^{'} V_O^{\bullet\bullet} R_M^{'}\right)^{x}. \tag{2.3}$$

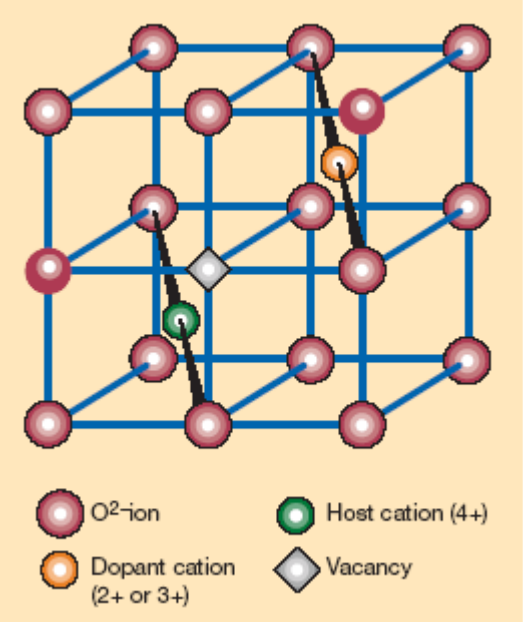

Figure 2.1 The fluorite structure of solid oxides. [2]

2.1.2 Ionic conductivity and activation energy

Under an elevated temperature, the oxygen ions in the fluorite-type oxides can overcome an energy barrier, known as the activation energy, to move diffusively by hopping to the neighbouring vacant sites. The ionic conductivity has the Arrhenius expression, given by:

$$\sigma = \frac{A}{T}\exp\left(\frac{-E_a}{k_B T}\right), \tag{2.4}$$

where A is the pre-exponential factor, T is the absolute temperature, k_B is the Boltzmann constant and E_a is the activation energy. Because the temperature dependence is dominated by the exponential term, the expression for conductivity is also frequently written as [3]:

$$\sigma = \sigma_0 \exp\left(\frac{-E_a}{k_B T}\right). \tag{2.5}$$

The activation energy is the utmost important factor that influences the ionic conductivity due to the exponential dependence. It can be obtained from the slope of the $log\sigma$ versus T^{-1} plot. At high temperatures, E_a corresponds to the migration enthalpy (ΔH_m). In the intermediate temperature range, E_a consists of migration enthalpy (ΔH_m) for the oxygen ion and the association enthalpy (ΔH_a) of the local defect structures. In a general expression, the activation energy is the sum of the migration enthalpy and the association enthalpy, written as [4]:

$$E_a = \Delta H_m + \frac{n}{2}\Delta H_a, \tag{2.6}$$

where n equals 1 for divalent dopants and 2 for trivalent dopants [4]. Kilner and Brook [5] pointed out that ΔH_m is determined by the host oxides whereas the ΔH_a is determined by the dopant level and distribution [6].

The pre-exponential factor, A, includes the other factors that influence the ionic conductivity, expressed as [7]:

$$A = \frac{n(ze)^2 \gamma d^2 \omega_0}{6k_B}, \tag{2.7}$$

where n is the concentration of mobile charge carriers, ze is the electric charge, γ is the correlation factor, d is the ion mean jump distance and ω_0 is related to the phonon frequency of the lattice vibrations.

Eq.(2.5) indicates that high ionic conductivity can be achieved by maximizing σ_0 and minimizing E_a. Two parameters, d and n, are critical to maximize σ_0, as indicated by Eq.(2.7). The factors that control the ionic conductivity are summarized in the following section.

2.1.3 Factors controlling the ionic conductivity

2.1.3.1 Ionic size of dopant cation

Van Gool [8] and Pouchard and Hagenmuller [9] have outlined some criteria that should favour high ionic conductivity in fluorite oxides, which are 1) High concentration of mobile charge carriers, i.e., oxygen vacancies; 2) The lattice energy of the dopant is equal to or only slightly different from that of the host oxides; 3) Weak bonding energy resulting in relatively low melting point; 4) Open paths between oxide ion sites. Among the above the mobile charge carrier concentration and the open path between oxide ion sites have been considered as the most important factors, which are both dominated by the ionic size of the dopant cation.

Kilner and Brook [5] proposed that maximum ionic conductivity in oxide fluorites could be achieved when the addition of dopant causes minimum elastic strain in the host crystal lattice. Kim [4] proposed a critical ionic radius (r_c), with which the dopant causes neither expansion nor contraction in the host fluorite oxide lattice. Cation with ionic radius equal to r_c should be the ideal dopant to show the highest ionic conductivity.

Mogensen *et al.* [10] summarized the values of Kim's r_c for four different fluorites, as listed in Table 2.1, where some near matching trivalent ions are also included. Also it is found from the table that neither the lattice energy nor the melting point of the host material has obvious correlation with the ionic conductivity. Thus, the ionic radius of the dopant is the dominant parameter that determines the concentration and the mobility of mobile oxygen vacancies.

Table 2.1 A collection of values relevant to the oxide ionic conductivity of doped fluorites $M_{1-x}Ln_xO_{2-\delta}$. [10]

Host cation, M^{4+}	Zr^{4+}	Ce^{4+}	Hf^{4+}	Th^{4+}
Radius of M^{4+} in eight-fold coordination (Å)	0.84	0.97	0.83	1.05
Critical ionic radius r_c (Å)	0.95	1.04	0.94	1.10
Near matching ion, Ln^{3+} and radius (Å)	Yb^{3+} 0.99	Gd^{3+} 1.05	Yb^{3+} 0.99	Nd^{3+} 1.11
Born-Haber lattice energy of MO_2 (MJ/mol)	5.4	5.1	5.6	5.3
Melting point of MO_2 (ºC)	2680	2750	2770	3390
Conductivity of $M_{0.8}Ln_{0.2}O_{1.9}$ at 800 ºC (mS/cm)	40	40	30	

Omar *et al.* [11] studied the relationship between the trivalent dopant cation size and the ionic conductivity and the activation energy in doped ceria, as shown in Figure 2.2. They found the maximum ionic conductivity is achieved in Nd-doped ceria instead of Gd-doped ceria as predicted by Kim's critical ionic radius theory. Also they found the migration enthalpy is dependent on dopant type, which is also against the previous reported data. They concluded that the ionic conductivity is not a function solely elastic strain, and r_c is not sufficient to predict the ionic conductivity in doped ceria.

Yamamoto *et al.* [12] studied the ionic conductivity of trivalent doped ZrO_2 and found a continuous decrease of conductivity with an increase in the dopant cation radius, as shown in Figure 2.3. Since their measurement was carried out at high temperature, the activation energy equals the migration enthalpy, which increases with an increase in the dopant cation radius. The highest ionic conductivity, as well as the lowest migration enthalpy, is obtained in Sc-doped ZrO_2, in which the dopant cation (Sc^{3+}) has the closest size as the Zr^{4+}. Similar results have also been reported by Stafford *et al.* [13] that the activation energy increases monotonously with an increase in the dopant cation size, and therefore a decrease in ionic conductivity in doped ZrO_2.

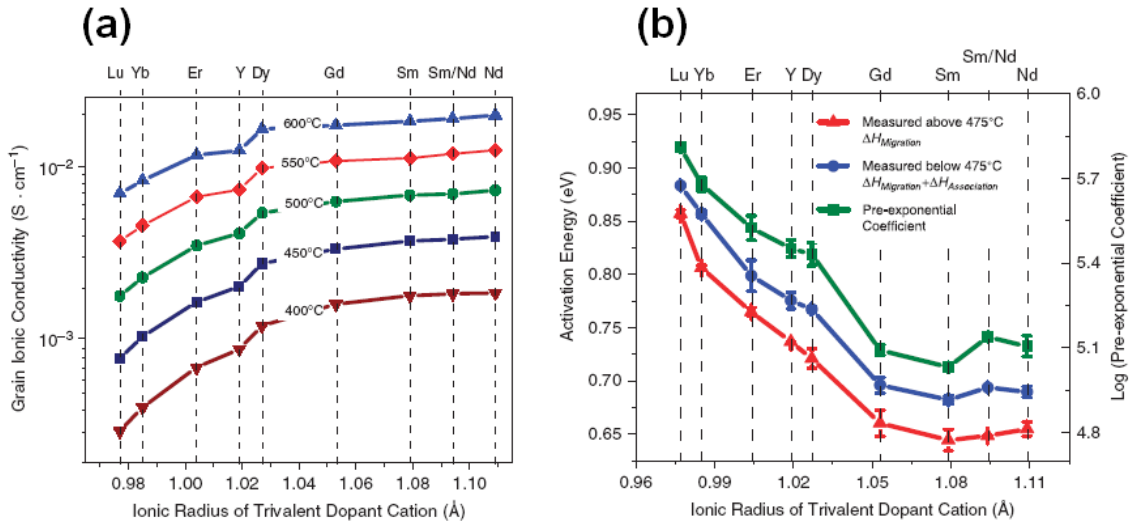

Figure 2.2 (a) Ionic conductivity of doped ceria with different trivalent dopant (10 mol% dopant content) at different temperatures; (b) Migration and association enthalpies for oxygen vacancy diffusion, and pre-exponential coefficient in doped ceria. [11]

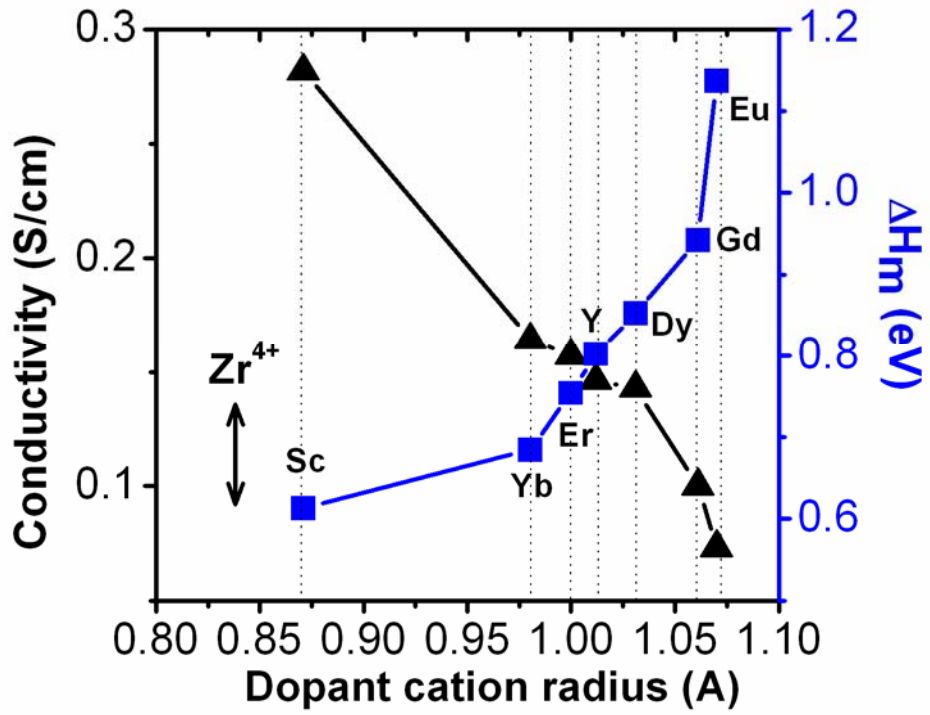

Figure 2.3 Maximum conductivity in Ln_2O_3 doped ZrO_2 systems at 1273 K, and the migration enthalpies as function of dopant cation radius. After [12, 14].

Although there remain unclear issues, previous research results do indicate the importance of dopant cation size on the ionic conductivity and the activation energy in fluorite-type oxides. Now it is generally accepted that undistorted lattice results in the highest concentrations of oxygen vacancies and the highest mobility of the charge carriers, and thus the highest ionic conductivity.

2.1.3.2 Dopant concentration

Dopant concentration directly determines the oxygen vacancy concentration, as indicated by the defect reaction described in Eq.(2.1). A high dopant concentration leads to a high charge carrier concentration and thus a high ionic conductivity. However, on the other hand, high dopant concentration decreases the mobility of oxygen vacancies by the formation of defect associates, as described in Eq.(2.2) and (2.3). Therefore, there exists an optimum dopant concentration to obtain the highest ionic conductivity. As shown in Figure 2.4, the highest ionic conductivity and the lowest activation energy are obtained in ~ 5 mol% Y_2O_3 doped CeO_2.

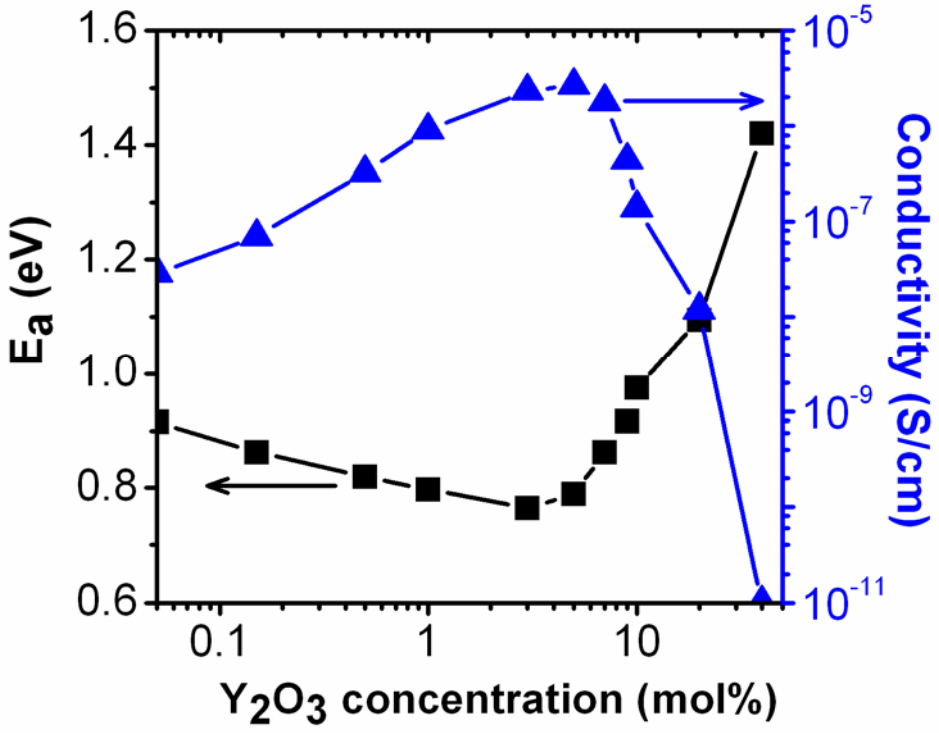

Figure 2.4 Variation of activation energy and the ionic conductivity at 182 ºC as a function of yttria concentration in ceria. After [15].

In ZrO_2 or HfO_2, similar phenomena have also been observed [16, 17]. The highest ionic conductivity is obtained in 8 mol% YSZ and 10 mol% yttria stabilised hafnia (YSH), respectively. However, there are phase changes when the dopant concentration increases in YSZ and YSH, which makes the systems complicated to attribute the ionic conductivity increase to the dopant concentration change only. However, in fully-stabilised cubic YSZ and YSH, further increase of yttria deteriorates the ionic conductivity, which can be attributed to the formation of defect associates.

In 2.1, the fundamentals of the ionic conduction in fluorite-type oxides are briefly introduced and the main factors that determine the ionic conductivity are summarized. In the next following parts, the ionic conductivity of YSZ, the most widely used electrolyte material for SOFCs, will be introduced.

2.2 Ionic conduction of YSZ

YSZ is a typical fluorite-type ionic conductor. Oxygen vacancies, generated by the substitution of Zr^{4+} by Y^{3+}, move diffusively under the electric field as charge carriers. The fundamentals of the ionic conduction in bulk YSZ have no difference with those in other fluorite-type oxide conductors. Therefore, in this session, only several factors that influence the ionic conductivity of YSZ are briefly specified. The main focus is on the grain boundary blocking effect, which is an important factor that determines the ionic conductivity of YSZ.

2.2.1 Effect of yttria concentration and temperature

The ionic conductivity increases with increasing Y_2O_3 concentration until about 8 - 9 mol% Y_2O_3 is reached, further increases in dopant concentration decrease the conductivity. Arachi *et al.* [16] found the highest ionic conductivity of 0.14 S/cm at 1000 ºC in 8 mol% YSZ, as shown in Figure 2.5. This indicates that the concentration of free oxygen vacancies decreases when the dopant concentration is greater than 8 mol%, suggesting the formation of defect associates $Y_{Zr}^{'} + V_O^{\bullet\bullet} \longrightarrow \left(Y_{Zr}^{'} V_O^{\bullet\bullet}\right)^{\bullet}$ becomes significant at high-dopant concentrations.

On the other hand, it is also noticeable that the Arrhenius plot shows a curvature as indicated by the red lines in Figure 2.5. The activation energy at low temperatures (below 650 ºC) is higher than that at high temperatures, which indicates that the formation of defect associates are conspicuous at low temperatures. As described in Eq.(2.6), the association enthalpy can be obtained by comparing the activation energies at high and low temperatures. Arachi *et al.* [16] reported a value of 0.28 eV for the association enthalpy.

Both the yttria concentration effect and the temperature effect indicate that the defect associates are important to the ionic conductivity of YSZ.

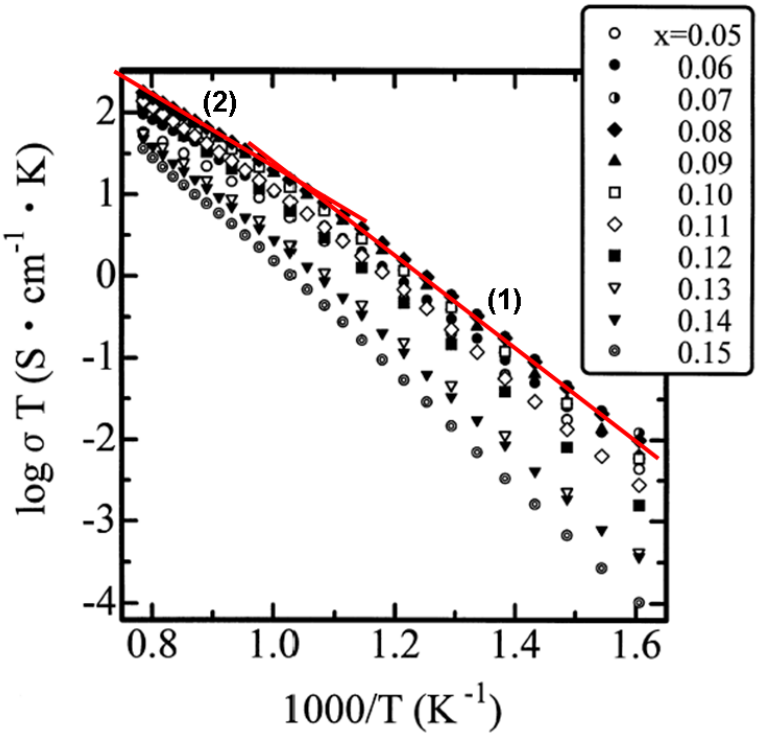

Figure 2.5 Temperature and composition dependences of the ionic conductivity for $(ZrO_2)_{1-x}(Y_2O_3)_x$. [16] The red lines indicate the slope change on the Arrhenius plot.

2.2.2 Effect of grain size

The influence of grain size on the bulk conductivity of YSZ is shown in Figure 2.6. The bulk conductivity initially increases with increasing grain size and then keeps constant.

As pointed out by Guo and Waser [18], the increase of bulk conductivity with increasing grain size is probably due to the grain-size-dependent grain-boundary segregation [19]: the grain boundary area reduces as the grain size increases, therefore, less solute within grains is "drained" to the grain boundaries [18]. For 8 mol% YSZ, the bulk conductivity is independent on the average grain size when it is larger than 5 μm.

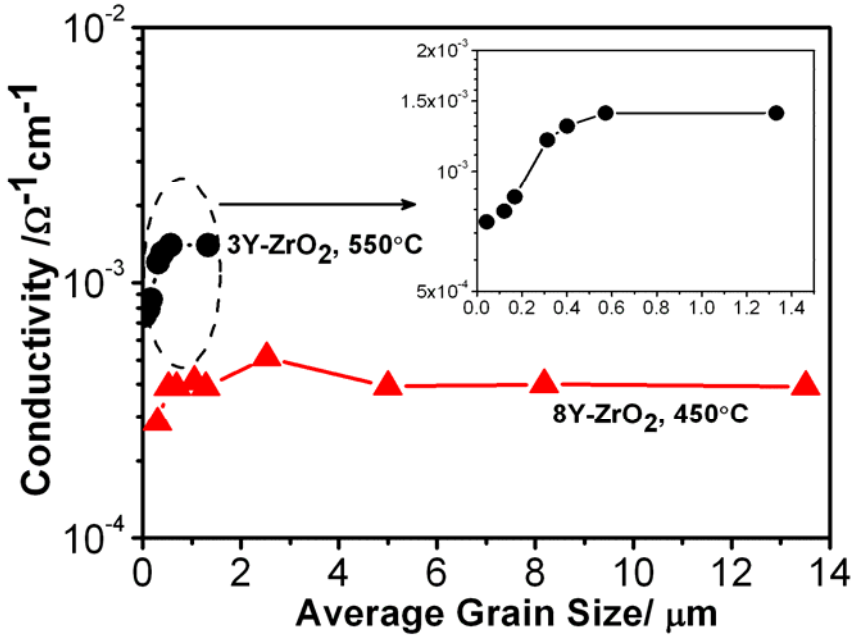

Figure 2.6 Bulk conductivity as a function of average grain size for 3 mol% Y_2O_3-doped ZrO_2 (3Y-ZrO_2) at 550 ºC (black circle, after [20]), 8.2 mol% Y_2O_3-doped ZrO_2 (8Y-ZrO_2) at 450 ºC (red triangle, after [18, 21]).

2.2.3 Effect of grain boundary

Grain boundary is a crucial part of the microstructure of a polycrystalline material, and it plays an important role in the ionic conduction of YSZ. In the past decade, the electrical properties of the YSZ grain boundaries attracted much interest and have been extensively studied. Now it has been well accepted that the grain boundaries of YSZ block the ionic transport across them (blocking effect) that the specific grain-boundary conductivity of YSZ is usually at least two orders of magnitude lower than that of the bulk [22], as shown in Figure 2.7.

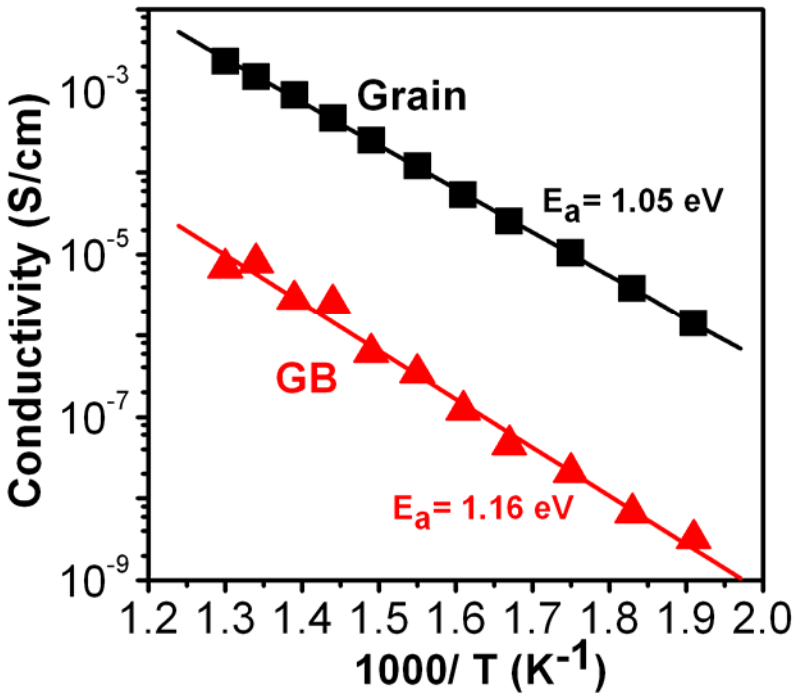

Figure 2.7 Bulk and grain-boundary conductivities of 8 mol% YSZ of high purity as a function of temperature. After [22].

2.2.3.1 Origin of the blocking effect

The grain-boundary blocking effect originates from two aspects. In the early studies, the blocking effect was usually attributed to the impurity segregations at grain boundaries, especially the intergranular siliceous phase [23-47]. However, later studies found the blocking effect still exists in highly pure YSZ materials in which the siliceous phase is not observed. The oxygen vacancy depletion in the grain-boundary space charge layer was proposed as another origin of the blocking effect [20, 22, 48-58]. Now it has been accepted as the decisive reason for the low grain-boundary conductivity.

(1) Impurities at grain boundaries

Based on the TEM observations of the siliceous phase morphology, a model has been proposed to explain the role of siliceous phase on the ionic conduction path of the grain boundary. As illustrated in Figure 2.8(a), the grain-to-grain contact is interrupted by the siliceous phase inclusions. Because of the very low ionic conductivity of the siliceous phase, the ionic conduction across the grain boundaries can occur only through the

grain-to-grain contact. The resistive siliceous phase restricts the ionic transport across the grain boundary by reducing the grain-to-grain contact area.

On the other hand, finite element calculations by Fleig and Maier [59] show the highly resistive phase has additional contribution to the grain-boundary resistance by the constriction of current lines, as shown in Figure 2.8(b). In the case of a circular grain-to-grain contact area, the resistance resulting from the current constriction by the siliceous phase, $R_{gb}^{(1)}$, can be calculated by:

$$\frac{R_{gb}^{(1)}}{< R_{bulk} >} = f_{geo} \frac{d_g}{w}, \tag{2.8}$$

where $<R_{bulk}>$ is the resistance of a grain, w is the diameter of the grain-to-grain contact area, d_g is the average grain size, and f_{geo} is the geometric correction factor, given by:

$$f_{geo} = \frac{1 - w/d_g}{1 + w/(2d_g)}. \tag{2.9}$$

The above two equations indicate the morphology and location determines the blocking effect contributed by the grain-boundary siliceous phase.

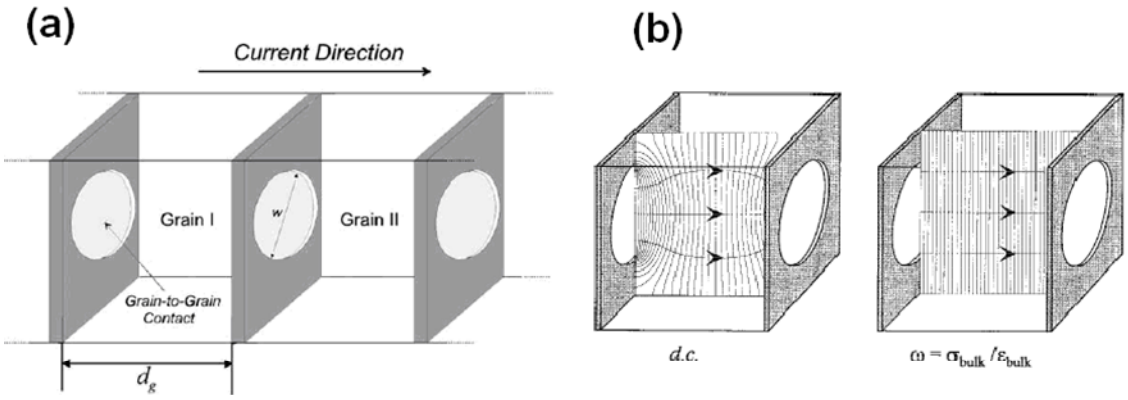

Figure 2.8 (a) Schematic representations of grain boundaries with highly resistive siliceous phase. [18] (b) Frequency-dependent potential distributions within a single grain showing the effect of the highly resistive phase. The distortion of the current line at low frequency leads to additional resistance to the grain boundary. [59]

(2) Oxygen vacancy depletion in the space charge layer

In the electrical point of view, an "electrical grain boundary" includes a grain boundary core and two adjacent space charge layers, as illustrated in Figure 2.9(a). The thickness of an "electrical grain-boundary" is expressed as $\delta_{gb} = 2\lambda^* + b$, where λ^* is the width of the space charge layer, and b is the thickness of the grain-boundary core. The YSZ grain boundary core has a high concentration of oxygen vacancies and it is positively charged, which has been proven by several theoretical studies [60-64] as well as experimental evidence [65] in other electroceramics. The positive charge of the grain boundary core is compensated by the accumulation of yttrium and the depletion of oxygen vacancies in the space charge layers. The oxygen vacancy profile is schematically presented in Figure 2.9(b).

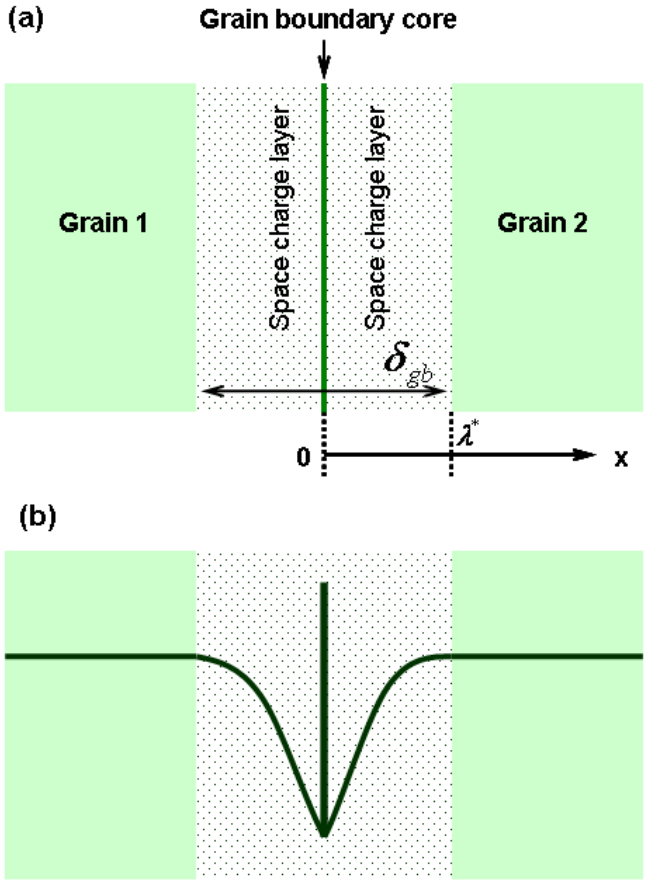

Figure 2.9 (a) Schematic representation of an "electrical grain boundary". At the interface between the space charge layer and the grain-boundary core $x = 0$, while far into the bulk $x = \infty$; (b) Oxygen vacancy concentration profiles in the space charge layers and grain-boundary core. After [18].

The concentration of the oxygen vacancy in the space charge layer can be expressed by:

$$\frac{c(x)}{c(\infty)} = \exp(-\frac{ze\Delta\varphi(x)}{k_B T}), \tag{2.10}$$

where $\Delta\varphi(x)$ is the electrostatic potential in relation to the bulk, z is the charge number ($z = 2$ for oxygen vacancies) and x is defined in Figure 2.9(a). Eq.(2.10) can be written as:

$$\sigma(x) = \sigma_{bulk} \exp(-\frac{ze\Delta\varphi(x)}{k_B T}), \tag{2.11}$$

where $\sigma(x)$ is the conductivity at x, σ_{bulk} is the bulk conductivity. The resistance of a space charge layer is:

$$< R_{gb}^{(2)} >= \frac{1}{\sigma_{gb}^{(2)}} \frac{\lambda^*}{S} = \frac{1}{\sigma_{bulk} S} \int_0^{\lambda^*} \exp(\frac{ze\Delta\varphi(x)}{k_B T}) dx \ . \tag{2.12}$$

The resistance of the bulk with the same size (area S and width λ^*) is:

$$R_{bulk} = \frac{1}{\sigma_{bulk}} \frac{\lambda^*}{S} \ . \tag{2.13}$$

The width of the space charge layer λ^* is expressed by:

$$\lambda^* = 2L_D (\frac{e\Delta\varphi(0)}{k_B T})^{1/2} \ . \tag{2.14}$$

where L_D is the Debye length, given by:

$$L_D = (\frac{k_B T \varepsilon}{2e^2 c_{Y_{Zr}^{'}}(\infty)})^{1/2} \ , \tag{2.15}$$

where $c_{Y_{Zr}^{'}}(\infty)$ is the concentration of yttrium in the bulk. $\Delta\varphi(0)$ is the electrostatic potential of the grain boundary core relative to the bulk (Schottky barrier height), and ε is the dielectric constant.

From Eq.(2.12) to (2.15), the relationship between σ_{gb} and σ_{bulk} can be established as [22, 66]:

$$\frac{\sigma_{bulk}}{\sigma_{gb}} = \frac{\exp(ze\Delta\varphi(0)/k_B T)}{2ze\Delta\varphi(0)/k_B T} . \tag{2.16}$$

Considering the grain boundary structure in Figure 2.8(a), the space charger layer only occurs around the grain-to-grain contact area. Thus the grain-boundary resistance, $R_{gb}^{(2)}$, can be written as:

$$\frac{R_{gb}^{(2)}}{< R_{bulk} >} = \frac{\exp(ze\Delta\varphi(0)/k_BT)}{2ze\Delta\varphi(0)/k_BT}\frac{8\lambda^*}{\pi w^2}d_g . \quad (2.17)$$

To summarize, the low conductivity of YSZ grain boundary originates from two effects. One is the current constriction by the resistive siliceous phase (extrinsic effect), and the other one is the oxygen vacancy depletion in the space charge layer (intrinsic effect). The total grain boundary resistance (R_{gb}) is therefore a sum of the above two resistances, i.e.,

$$R_{gb} = R_{gb}^{(1)} + R_{gb}^{(2)} . \quad (2.18)$$

2.2.3.2 Factors that influence the grain boundary conductivity

(1) Impurity concentration

The impurity concentration can be represented by the value of w/d_g. A large value of w/d_g indicates a low impurity concentration, whereas a small w/d_g indicates a high impurity concentration. The influence of impurity concentration (w/d_g) on each contribution of grain boundary resistance ($R_{gb}^{(1)}$ and $R_{gb}^{(2)}$) is illustrated in Figure 2.10, where it shows both $R_{gb}^{(1)}$ and $R_{gb}^{(2)}$ decrease with an increase of w/d_g.

In the case of very low impurity concentration, $w/d_g \approx 1$. From Eq. (2.8) and (2.9), it can be derived that $R_{gb}^{(1)} \approx 0$. The contribution from the impurity phase to the grain boundary resistance is negligible. Therefore, $R_{gb} \approx R_{gb}^{(2)}$, which is determined by the Schottky barrier height $\Delta\varphi(0)$ and will be discussed later. On the contrary, when the impurity concentration is extremely high (e.g. $w/d_g \leq 0.052$), considering reasonable $\Delta\varphi(0)$ values of 0.25 – 0.30 V for 8 mol% YSZ, the grain boundary resistance is also dominated by the oxygen vacancy depletion in the space charge layer. However, since the coverage of the grain boundaries by the siliceous phase is too high, this case is unlikely to happen in the reality. Excluding the above two extreme situation, in a wide range of normal impurity concentration, the w/d_g value is within the shaded area in Figure 2.10. The relative magnitude of $R_{gb}^{(1)}$ and $R_{gb}^{(2)}$ is determined by the Schottky barrier height $\Delta\varphi(0)$. When $\Delta\varphi(0)$ is low (e.g., 0.25 V), $R_{gb}^{(1)} > R_{gb}^{(2)}$, the siliceous phase

contributes more to the grain boundary resistance than the space charge effect. However, with an increase of Δφ(0), the concentration range within which $R_{gb}^{(1)} > R_{gb}^{(2)}$ becomes narrower, thus the space charge effect becomes more and more effective. When Δφ(0) is very high (e.g., 0.35 V) the space charge effect is dominant in the grain boundary resistance at all impurity concentrations.

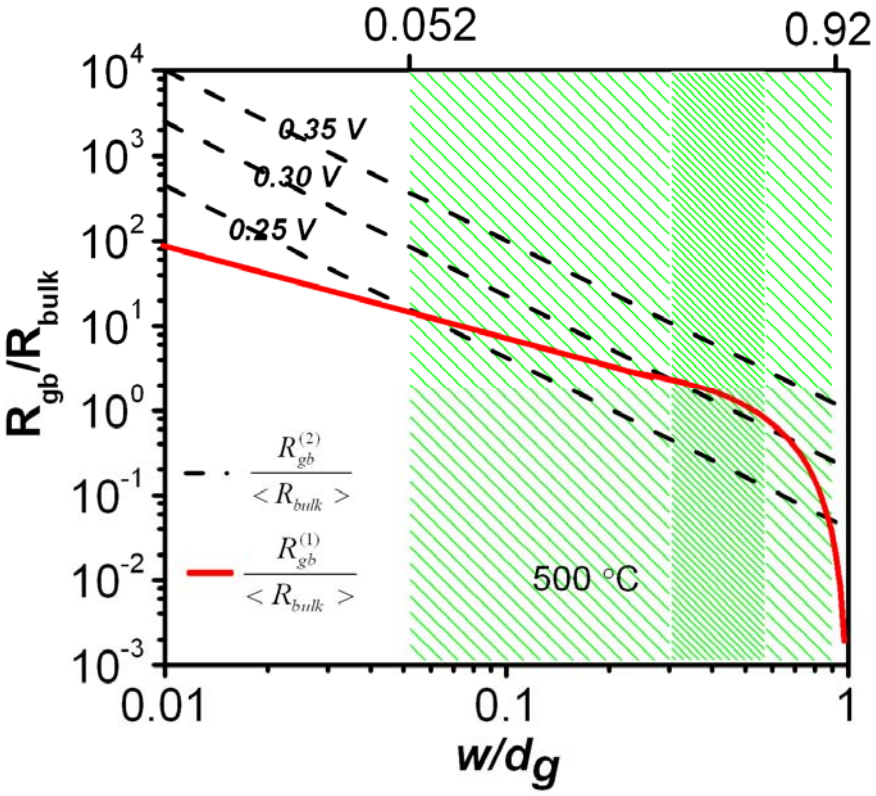

Figure 2.10 Calculated $R_{gb}^{(1)} / < R_{bulk} >$ and $R_{gb}^{(2)} / < R_{bulk} >$ at 500 ºC as a function of w/d_g for 8 mol% YSZ. After [56].

(2) Schottky barrier height

Schottky barrier height determines the "intrinsic" grain boundary conductivity (contribution from the space charge effect), as described by Eq.(2.16). It also determines the relative magnitude of $R_{gb}^{(1)}$ and $R_{gb}^{(2)}$ at a certain impurity level, as stated in the previous paragraph. Numerical analysis of Eq.(2.16) shows the grain boundary

conductivity decreases with an increase in the Schottky barrier height providing the bulk conductivity is constant, as displayed in Figure 2.11.

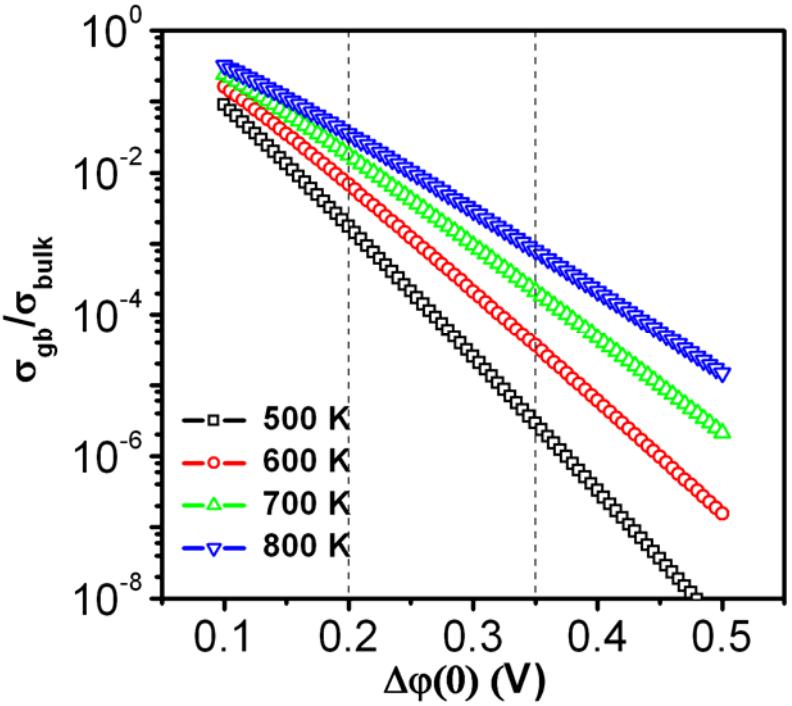

Figure 2.11 $\sigma_{gb}/\sigma_{bulk}$ as a function of the Schottky barrier height Δφ(0). The range within the two dash lines is the reasonable Δφ(0) for 8 mol% YSZ.

(3) Grain size

Within a wide grain size range (tens of nanometers to tens of micrometers), the specific grain boundary conductivity decreases with an increase in the average grain size in YSZ and other element doped-ZrO_2, as illustrated in Figure 2.12. The decrease of grain boundary conductivity is more pronounced when the grain size is small (less than 2 μm for YSZ and less than 4 μm in CaO-doped zirconia). Guo and Zhang [20] calculated the Schottky barrier height and the concentration of oxygen vacancies as a function of average grain size. They found the Schottky barrier height increases with increasing grain size, which leads to a decrease of the oxygen vacancy concentration in the space charge layer and consequently results in the decreasing grain boundary conductivity.

Further decrease of grain size to less than 10 nanometers in YSZ will cause the overlap of the neighbouring space-charge layers (usually the width of a space charge layer in

YSZ is around 5 nm). In this case the electrical conductivity can be very different from the coarse-grained materials. However, such a tiny grain size is difficult to obtain in sintered YSZ bulk samples (the material of interest in this thesis), further discussion won't be carried out here.

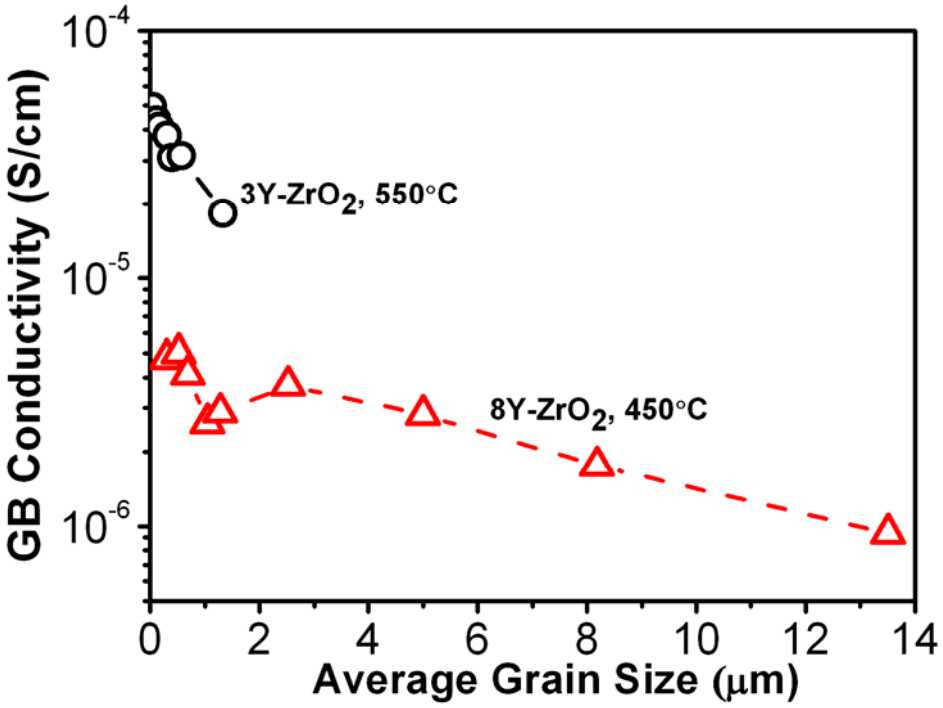

Figure 2.12 Specific grain boundary conductivity as a function of average grain size for 3 mol% Y_2O_3-doped ZrO_2 (3Y-ZrO_2) at 550 ºC (black circle, after [20]), 8.2 mol% Y_2O_3-doped ZrO_2 (8Y-ZrO_2) at 450 ºC (red triangle, after [18, 21]).

2.3 Characterisation of electrical properties -- Impedance spectroscopy

2.3.1 Fundamentals [67]

When a small amplitude sinusoidal voltage signal $v(t) = V_m \sin(\omega t)$, where ω is the angular velocity ($\omega = 2\pi f$, where f is the frequency), is applied to a material, a steady state current $i(t) = I_m \sin(\omega t + \theta)$ will be generated. Here θ is defined as the phase angle, which represents the phase difference between the current and the voltage. The ratio of the applied voltage to the current is known as the impedance of the material, defined as $Z(\omega) = v(t)/i(t)$, with a modulus of $|Z(\omega)| = V_m / I_m$ and a phase angle, θ.

Impedance is a vector quantity which can be expressed by the sum of a real part Z' and an imaginary part Z'', $Z = Z' - jZ''$. The imaginary number $j = \sqrt{-1}$ indicates an anti-clockwise rotation by π/2 relative to the real axis. The magnitude and direction of the impedance, Z, can be represented by a planar vector in a right-hand orthogonal system, as plotted in Figure 2.13.

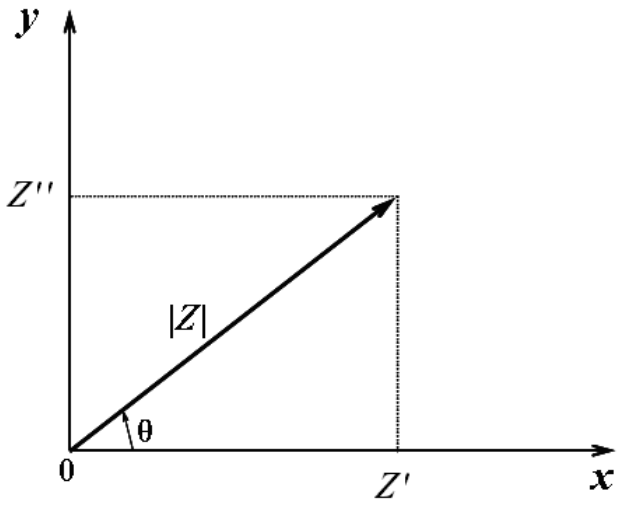

Figure 2.13 The impedance Z plotted as a planar vector.

From Figure 2.13, the relationships among the parameters can be obtained:

$$\begin{aligned} Z' &= |Z|\cos\theta \\ Z'' &= |Z|\sin\theta \\ |Z| &= \sqrt{(Z')^2 + (Z'')^2} \\ \theta &= \tan^{-1}(Z''/Z') \end{aligned} \quad (2.19)$$

2.3.2 Impedance response of dielectric materials

For an ideal dielectric material, the electrical response to an AC voltage can be represented by a R (Resistor)-C (Capacitor) parallel circuit (illustrated in Figure 2.14(a)). The impedance is expressed as:

$$\frac{1}{Z} = \frac{1}{R} + j\omega C \,. \tag{2.20}$$

Therefore:

$$Z = \frac{R}{1+\omega^2 C^2 R^2} - j\frac{\omega C R^2}{1+\omega^2 C^2 R^2} = Z' - jZ'' ; \tag{2.21}$$

$$(Z'')^2 + (Z' - \frac{R}{2})^2 = (\frac{R}{2})^2 \,. \tag{2.22}$$

Consequently, the Nyquist plot (Z'' versus Z') for the R-C parallel circuit is a single semicircle with the centre located at (R/2, 0) (shown in Figure 2.14(b)). The diameter of the semicircle equals the resistance of the sample. When Z'' reaches the maximum value R/2, the angular velocity $\omega_{max} = 1/(RC)$, corresponds to a relaxation frequency $f = \omega_{max}/(2\pi)$, which is an important parameter related to the physical nature of the material.

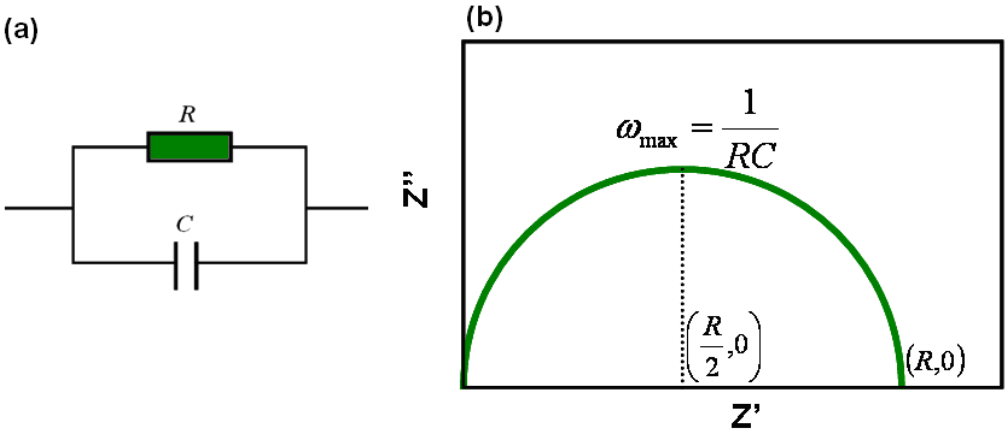

Figure 2.14 Schematic of (a) equivalent circuit (b) Nyquist plot of an ideal dielectric material.

However, when there exists chemical inhomogeneity or geometrical non-uniformity in a material, the capacitance response is often not as a pure capacitor. This deviation can be modelled by using a constant phase element (CPE) instead of an ideal capacitor in the equivalent circuit. The impedance of a CPE, Z_{CPE}, is given by [67-69]:

$$Z_{CPE} = \frac{1}{Q(j\omega)^n} = Q^{-1}\omega^{-n}[\cos(\frac{n\pi}{2}) + j\sin(\frac{n\pi}{2})]^{-1} \,, \tag{2.23}$$

where Q is a parameter independent of frequency. When n = 0, the CPE represents a pure resistor and Q equals $\frac{1}{R}$. When the exponential factor n = 1, the CPE functions as an ideal capacitor and Q is equal to the capacitance C. In the case of non-ideal capacitive response, the value of Q can not be used to represent the capacitance of the material. An equivalent capacitance C is adopted to represent the capacitive behaviour, which is defined as [70]:

$$C = R^{(1-n)/n} Q^{1/n}. \tag{2.24}$$

2.3.3 Typical impedance spectra of YSZ

A typical impedance spectroscopy (Nyquist plot) of YSZ is shown in Figure 2.15. Three arcs are displayed on the Nyquist plot, from high frequency to low frequency (left to right), corresponding to the responses from grain, grain boundary and electrode, respectively. The equivalent circuit, therefore, is three R-CPE elements in parallel connection, as shown in the inset. From the impedance spectroscopy and equivalent circuit fitting, the resistance and capacitance of YSZ grain and grain boundary can be obtained. The conductivity of grain and grain boundary can be calculated using the following equations [18]:

$$\sigma_{Grain} = \frac{1}{R_{Grain}} \frac{d}{A}, \tag{2.25}$$

$$\sigma_{GB} = \frac{1}{R_{GB}} \frac{C_{Grain}}{C_{GB}} \frac{d}{A}, \tag{2.26}$$

where d is the sample thickness, A is the cross section area of the sample. The dielectric constant of the sample can also be obtained, by:

$$\varepsilon_r = \frac{C_{Grain}}{\varepsilon_0} \frac{n d_{Grain}}{A}, \tag{2.27}$$

where d_{Grain} is the average grain size, and n the number of grains to be trespassed in the current direction. The dielectric constant of YSZ grain boundary is approximately the same as that of grain [22,71].

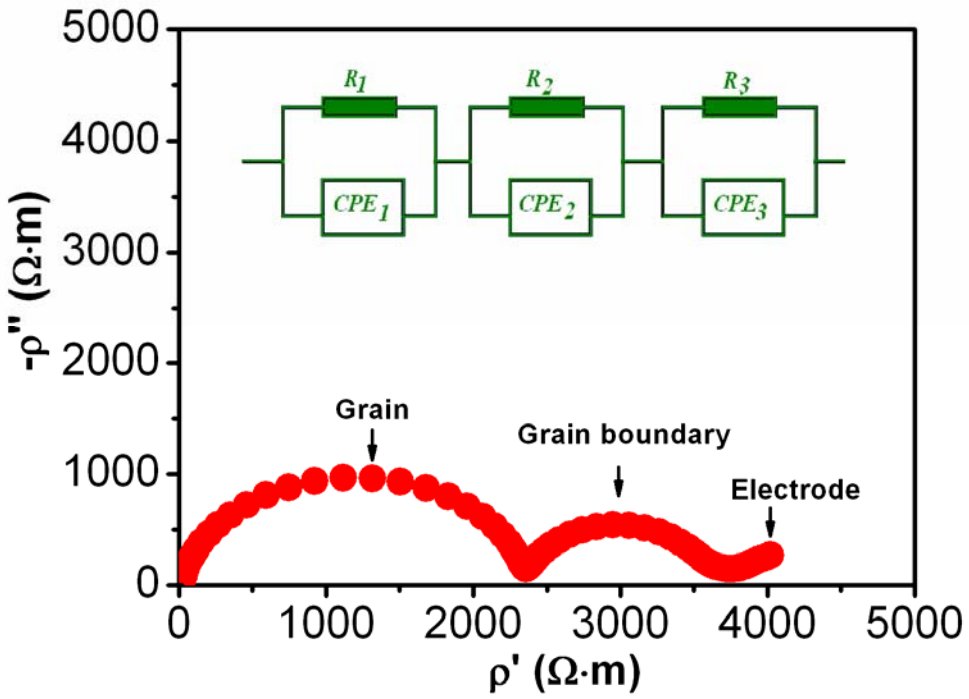

Figure 2.15 Typical impedance spectroscopy (Nyquist plot) and equivalent circuit of YSZ (8 mol% YSZ, cold-pressed and sintered at 1500 ºC, measured at 300 ºC).

2.3.4 Finite element modelling

The finite element method (FEM) (sometimes referred to as finite element analysis) is a numerical technique for finding approximated solution of partial differential equations (PDE) as well as of integral equations. The application of FEM in impedance spectra simulation was firstly proposed by Fleig *et al.* The fundamentals are described below [72, 73].

The impedance can be determined by the calculation of the exact potential distribution within the sample. This implies the numerical solving of the underlying differential equation. As long as time-dependent magnetic fields can be neglected, the Poisson's equation can be written in terms of a scalar electrical potential:

$$divgrad\Phi(r,t) = -\frac{1}{\varepsilon_0 \varepsilon_r}\rho(r,t), \qquad (2.28)$$

where Φ is the electrical potential, ε_0 is the vacuum dielectric constant, ε_r is the relative dielectric constant, and ρ is the charge density. In a two-dimensional case, if we ignore

the space charges and only take the surface charges into account, Eq.(2.28) can be reduced to Laplace's equation:

$$\frac{\partial^2 \Phi}{\partial x^2} + \frac{\partial^2 \Phi}{\partial y^2} = 0. \tag{2.29}$$

For an applied AC voltage $U_0 e^{j\omega t}$ of angular frequency ω between the two electrodes the potential Φ within the sample is given in complex representation by

$$\hat{\Phi}(r,t) = \hat{\varphi}(r) e^{j\omega t} \equiv \left|\hat{\varphi}(r)\right| e^{j(\omega t + \alpha(r))}, \tag{2.30}$$

provided the deviations from equilibrium are small (linear regime).

The boundary conditions are defined as the follows:

(1) Dirichlet boundary condition, which means the electrical potential of the electrode (position-independent) is identical to the potential of the solid electrolyte, is applied to the electrode/solid electrolyte interface, where the electrochemical effects are ignored.

(2) Neumann boundary condition: $grad\Phi \cdot \vec{n} = 0$, where $\vec{n}$ is the normal vector of the relevant interface or surface. Dielectric displacement currents crossing the free surfaces are neglected (analogous to an ideal plate capacitor).

(3) Inner interface: the continuity of the normal component of the complex current density must be warranted:

$$\hat{k}_1 grad\hat{\Phi}_1 \cdot \vec{n} = \hat{k}_2 grad\hat{\Phi}_2 \cdot \vec{n}. \tag{2.31}$$

The complex conductivity $\hat{k}$ is defined by:

$$\hat{k} = \sigma + j\omega\varepsilon_0\varepsilon_r, \tag{2.32}$$

with σ being the conductivity and ω the angular frequency of the applied AC voltage. Eq.(2.31) can be derived by combining Poisson's equation (Eq.(2.28)) and the continuity equation for the Faraday current density (total current density minus displacement current density, i.e., true conducting current density -- $\sigma grad\hat{\Phi}$)

$$div(\sigma grad\hat{\Phi}) = \frac{\partial \hat{\rho}}{\partial t}, \tag{2.33}$$

using Eq.(2.30) and integrating over the surface of a thin volume element at the phase boundary.

For the potential difference $\hat{U}$ between the two electrodes, the total complex impedance can be calculated as:

$$\hat{Z} = \frac{\hat{U}}{\int_A -\hat{k} grad \hat{\Phi} ds}, \tag{2.34}$$

The integration is carried out along an equipotential line, *ds* being the differential normal vector element of the line. Once the potential distribution $\hat{\Phi}(x, y)$ is known, the impedance can be calculated for a given complex conductivity. By varying frequency and thus the complex conductivity, it is possible to simulate the entire impedance spectrum for a given sample geometry. The finite element method was used to solve the partial differential equation numerically in order to obtain the complex electrical potential.

An example of the FE modelling of the impedance spectroscopy of YSZ is shown in Figure 2.16. Based on the real microstructure of the sintered YSZ, a geometric model is established as shown in Figure 2.16(a). By defining the physical properties of each component (e.g., grain and grain boundary) and applying the boundary conditions to each surface and interface (as indicated in the numbers), the impedance spectroscopy of the model can be worked out, as shown in Figure 2.16(b). FE modelling is an effective and convenient method to study the structure- property relationship.

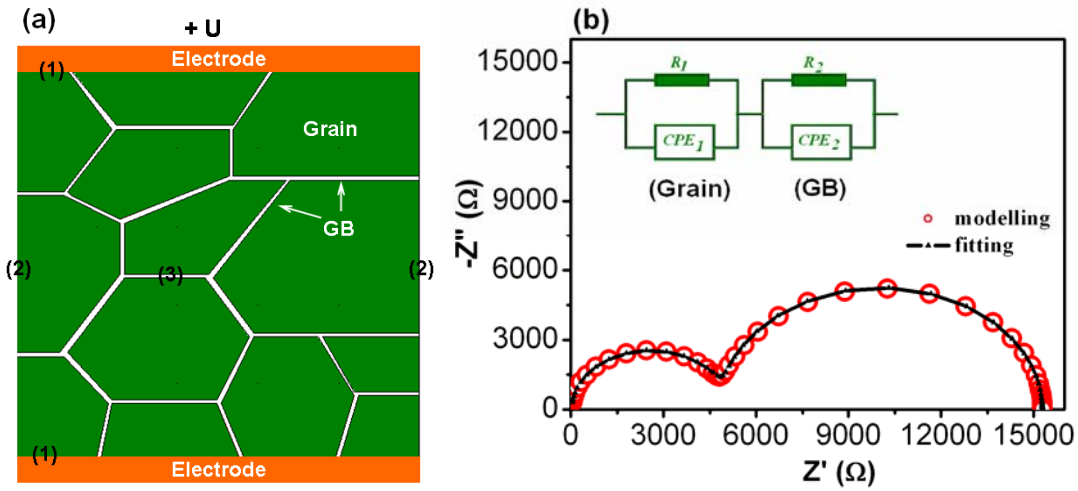

Figure 2.16 (a) A geometric model for FE modelling. The numbers indicate the boundary condition used. (b) The calculated impedance spectroscopy of the model, along with the equivalent circuit and the fitting curve.

2.4 Summary of part I

Part I of this chapter reviewed the ionic conduction of YSZ. Information obtained from the references is summarized below.

(1) YSZ is a typical fluorite-type ionic conductor. Oxygen vacancies, generated by substitution of Zr^{4+} by Y^{3+}, move diffusively under the electric field as charge carriers;

(2) Ionic conductivity of YSZ depends on the yttria concentration. The highest ionic conductivity is obtained in 8 mol% YSZ. Further increase of yttria concentration decreases the ionic conductivity because the formation of defect associates becomes significant at high dopant concentration.

(3) Activation energy equals migration enthalpy at high temperatures, whereas it is a sum of the migration enthalpy and the association enthalpy at low temperatures (< 650 ºC).

(4) The grain boundary conductivity is 2 or 3 orders of magnitude lower than the bulk (grain) conductivity of YSZ (so called blocking effect). The blocking effect originates from the impurity segregation at grain boundaries or the space charge effect, with the latter one as the dominant mechanism.

(5) Impedance spectroscopy is an effective method to study the electrical and dielectric properties of YSZ grain and grain boundary.

PART 2. Thermal conduction mechanism of YSZ

2.5 Fundamentals of thermal conduction in dielectric materials

The thermal conductivity of a material, k ($W \cdot m^{-1} \cdot K^{-1}$), is a measure of heat flow in a temperature gradient, as described by the Fourier's law [74]:

$$q = -k \cdot \nabla T , \tag{2.35}$$

where q is the heat flux density through the cross-section per unit time ($W \cdot m^{-2}$) and ∇T is the temperature gradient ($K \cdot m^{-1}$).

By analogy with the kinetic theory of gases, Debye derived an expression of the thermal conductivity, written as [75]:

$$k = \frac{1}{3} C \cdot v \cdot \Lambda , \tag{2.36}$$

where C is the specific heat, v is the phonon velocity and Λ is the phonon mean free path. In the form of lattice waves, over a spectrum of frequencies ω, Eq.(2.36) can be rewritten as [76]:

$$k = \frac{1}{3} \int_0^{\omega_D} C(\omega, T) \cdot v \cdot \Lambda(\omega) d\omega , \tag{2.37}$$

where ω_D is the Debye frequency; $C(\omega)d\omega$ is the contribution to the specific heat from the vibration modes having a frequency between ω and $\omega+d\omega$.

In a polycrystalline ceramic material, the phonon mean free path usually includes the contributions from phonon-phonon scattering, phonon-point defect scattering and phonon-grain boundary scattering. The contributions from the above processes are introduced in the following parts.

2.5.1 Umklapp phonon-phonon process [77]

At temperatures higher than the Debye temperature Θ_D, the specific heat $C(\omega)$ is proportional to ω^2 and it is independent of temperature, expressed as:

$$C(\omega,T) = B \cdot \omega^2 , \tag{2.38}$$

where B is a constant. The mean free path associated with Umklapp phonon-phonon interactions, Λ_U, is proportional to ω^{-2} and T^{-1} at high temperatures, expressed as:

$$\Lambda_U(\omega,T) = \frac{D_U}{\omega^2 T}, \tag{2.39}$$

where D_U is a parameter independent of temperature and frequency.

Substitute Eq.(2.38) and (2.39) into Eq.(2.37), the classical T^{-1} variations of the intrinsic thermal conductivity is obtained:

$$k = \frac{1}{3}\int_0^{\omega_D} B\omega^2 \cdot v \cdot \frac{D_U}{\omega^2 T} d\omega = \frac{A}{T}, \tag{2.40}$$

where $A = \frac{1}{3} B v D_U \omega_D$.

In Eq.(2.39), it is indicated that the phonon mean free path decreases continuously with increasing temperature. However, due to the fact that the phonon mean free path can not be shorter than the distance between two neighbouring atoms, there exists a minimum mean free path Λ_{min}, as suggested by Roufosse and Klemens [78], that

$$\Lambda(\omega,T) = \frac{D_U}{\omega^2 T}, \text{ if } \frac{D_U}{\omega^2 T} > \Lambda_{min}, \tag{2.41}$$

$$\Lambda(\omega,T) = \Lambda_{min}, \text{ if } \frac{D_U}{\omega^2 T} < \Lambda_{min}. \tag{2.42}$$

Consequently, integration of Eq.(2.37) gives:

$$k = \frac{1}{3}\left(\int_0^{\omega'} B\omega^2 v \frac{D_U}{\omega^2 T} d\omega + \int_{\omega'}^{\omega_D} B\omega^2 v \Lambda_{min} d\omega\right) = \frac{A}{T}\left(\frac{2}{3}\sqrt{\frac{T_1}{T}} + \frac{T}{3T_1}\right), \tag{2.43}$$

where $\omega' = \sqrt{\frac{D_U}{\Lambda_{\min} T}} = \sqrt{\frac{T_1}{T}}\omega_D$ and $T_1 = \frac{D_U}{\Lambda_{\min}(\omega_D)^2}$. Eq.(2.43) indicates the thermal conductivity of the a solid material might decrease less rapidly than the T^{-1} law.

Based on the above theory, the minimum high temperature thermal conductivity (k_{min}) of one material can be predicted from its physical properties, expressed as [79,80]:

$$k_{\min} \to 0.87 k_B \sqrt{\frac{E}{\rho}} \Omega_a^{-2/3} \to 0.87 k_B N_A^{2/3} \frac{m^{2/3} \rho^{1/6} E^{1/2}}{M^{2/3}}, \qquad (2.44)$$

where $\Omega_a = \frac{M}{m N_A \rho}$ is the average volume per atom; k_B and N_A are Boltzmann's and Avogadro's constant, respectively; m is the number of atoms per molecule; M is the molecular mass; ρ is the density and E is the Young's modulus. The minimum thermal conductivity, calculated from Eq.(2.44), of a variety of materials is plotted in Figure 2.17, indicating that materials with high average atomic volume (Ω_a) and low specific elastic modulus (E/ρ) have low thermal conductivities.

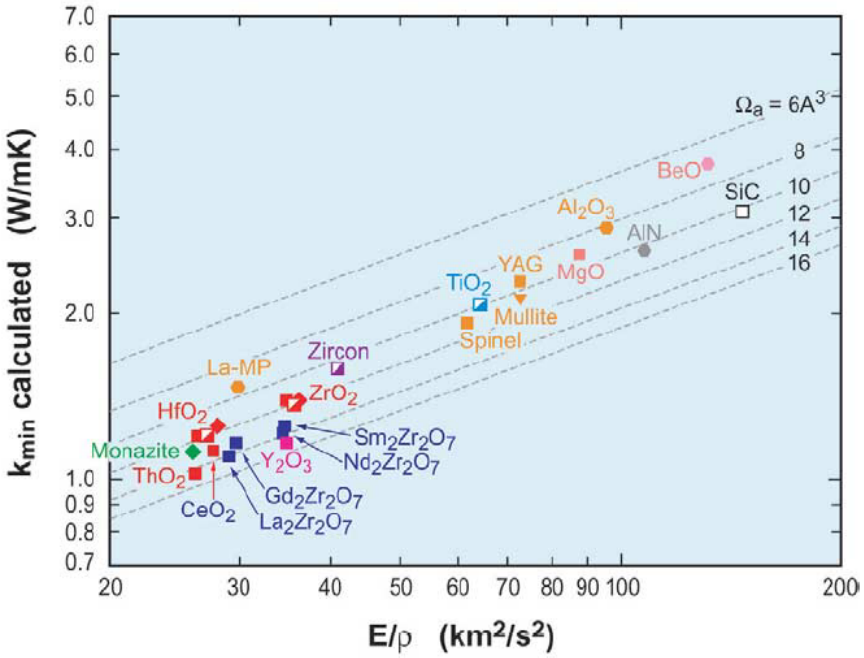

Figure 2.17 Minimum thermal conductivity of a variety of materials, calculated from Eq.(2.44). [79,81]

2.5.2 Phonon-point defect scattering [77]

The point defects in the material interact with phonons and contribute to a phonon mean free path Λ_D, which is dependent on the point defect concentration (c_D) and frequency, but independent of temperature. It is expressed as:

$$\Lambda_D(\omega) = \frac{D_D}{c_D \cdot \omega^4}, \tag{2.45}$$

where D_D is a parameter independent of temperature and frequency.

Assuming the phonon-phonon and the phonon-point defect scattering are independent procedures, the total phonon mean free path, Λ, can be written as:

$$\frac{1}{\Lambda(\omega,T)} = \frac{1}{\Lambda_U(\omega,T)} + \frac{1}{\Lambda_D(\omega)}. \tag{2.46}$$

Combining Eq.(2.39), (2.45) and (2.46), the mean free path is:

$$\frac{1}{\Lambda(\omega,T)} = \frac{\omega^2 T}{D_U} + \frac{c_D \omega^4}{D_D}. \tag{2.47}$$

Employing the concept of minimum mean free path, then:

$$\frac{1}{\Lambda(\omega,T)} = \frac{\omega^2 T}{D_U} + \frac{c_D \omega^4}{D_D} \text{ if } \frac{\omega^2 T}{D_U} + \frac{c_D \omega^4}{D_D} < \frac{1}{\Lambda_{\min}}, \tag{2.48}$$

$$\frac{1}{\Lambda(\omega,T)} = \frac{1}{\Lambda_{\min}} \text{ if } \frac{\omega^2 T}{D_U} + \frac{c_D \omega^4}{D_D} > \frac{1}{\Lambda_{\min}}. \tag{2.49}$$

Then integration of Eq.(2.37) gives:

$$\begin{aligned} k &= \frac{1}{3}\left(\int_0^{\omega_1} B\omega^2 v \frac{1}{\frac{\omega^2 T}{D_U} + \frac{c_D \omega^4}{D_D}} d\omega + \int_{\omega_1}^{\omega_D} B\omega^2 v \Lambda_{\min} d\omega \right) \\ &= \frac{A}{T}\left(\frac{\omega_0}{\omega_D}\right) arctg\left(\frac{\omega_1}{\omega_0}\right) + \frac{A}{3T}\left[\frac{1}{1+\left(\frac{\omega_1}{\omega_0}\right)^2}\right]\left[\left(\frac{\omega_D}{\omega_1}\right)^2 - \frac{\omega_1}{\omega_D}\right] \end{aligned}, \tag{2.50}$$

where $\omega_0 = \sqrt{\frac{\beta T}{c_D}}$, $\beta = \frac{D_D}{D_U}$ and $\omega_1 = \omega_0 \sqrt{-\frac{1}{2} + \sqrt{\frac{1}{4} + \left(\frac{\omega'}{\omega_0}\right)^2}}$. The frequency ω_1 is defined by $\Lambda(\omega_1) = \Lambda_{\min}$.

2.5.3 Phonon-grain boundary scattering [82]

Grain boundaries are important components of polycrystalline ceramic materials. They scatter phonons and contribute to a phonon mean free path, Λ_{GB}, which is a frequency-independent constant corresponding to a characteristic length L:

$$\Lambda_{GB} = L . \tag{2.51}$$

Thus in a polycrystalline ceramic material without point defects, both the Umklapp phonon-phonon scattering and the phonon-grain boundary scattering contribute to the thermal conduction, with a phonon mean free path of:

$$\frac{1}{\Lambda(\omega)} = \frac{1}{\Lambda_U(\omega,T)} + \frac{1}{\Lambda_{GB}} = \frac{1}{\Lambda_U(\omega,T)} + \frac{1}{L} . \tag{2.52}$$

The reduction in thermal conductivity caused by phonon-grain boundary scattering is given by:

$$\Delta k = k\left(\frac{\omega_B}{\omega_D}\right) arctg\left(\frac{\omega_D}{\omega_B}\right), \tag{2.53}$$

where ω_B is the frequency at which $\Lambda_U(\omega_B) = L$. And from Eq.(2.39), ω_B is obtained as $\omega_B = \sqrt{\frac{D_U}{TL}}$.

Grain boundaries are effective of scattering low frequency phonons. Assuming the phonons are randomly scattered at each grain boundary, the characteristic length L can be identified as the average grain size. Consequently the grain boundary can effectively scatter the phonons only when the grain size is small enough, i.e., in nano-metre scale.

2.6 Thermal conductivity of YSZ

As stated in Chapter 1, YSZ is the state-of-art TBC material because it provides the best performance in high temperature applications. It has a low and temperature-independent thermal conductivity, which is usually attributed to the presence of a high point defect concentration caused by the substitution of Zr^{4+} by Y^{3+} ions in the fluorite structure, producing a small spacing between point defects [81]. Thermal conductivity of YSZ, both its bulk material and coating, has been extensively studied. In the mean time, lots

of efforts has been devoted to modify YSZ, e.g., by adding other dopants, to decrease its thermal conductivity.

2.6.1 Phonon-phonon and phonon-defect scattering in YSZ

In YSZ, the thermal conductivity is determined by the phonon-phonon scattering process (intrinsic) and the phonon-defect scattering process. The intrinsic thermal conductivity of pure ZrO_2, considering the minimum phonon mean free path, is described in Eq.(2.43). Mévrel *et al.* [77] fitted their experimental results by Eq.(2.43) and reported the constant A is 2400 W/m and T_1 = 420 K.

The mean free path caused by phonon-defect scattering, as described in Eq.(2.44), can be rewritten as [83]:

$$\frac{1}{\Lambda_D(\omega)} = \frac{a^3}{4\pi v^4} c_D \left(\frac{\Delta M}{M}\right)^2 \omega^4, \tag{2.54}$$

where M is the atomic mass of the host atom, ΔM is the mass difference between the host and the substitutional atom; a^3 is the mean atomic volume and v is the averaged sound velocity. In the presence of point defects, the thermal conductivity is written as [84,85]:

$$k = k_{U(\min)} \left(\frac{\omega_0}{\omega_m}\right) arctg\left(\frac{\omega_m}{\omega_0}\right), \tag{2.55}$$

where ω_m is the Debye frequency of the acoustic branch, given by $\omega_m = \omega_D m^{-1/3}$ with m is the number of atoms per molecule. And [85]:

$$\left(\frac{\omega_0}{\omega_m}\right)^2 = \left(\frac{4\gamma^2}{\mu a^3}\right)\left[c_D\left(\frac{\Delta M}{\overline{M}}\right)^2\right]^{-1}, \tag{2.56}$$

where γ is the Grüneisen constant and μ is the shear modulus.

In YSZ, two types of point defects are created: (1) sustitutional solute atoms (Y on Zr sites); (2) oxygen vacancies due to the aliovalent nature of the dopant (anion sites). Thus the term $c_D(\Delta M / M)^2$ in Eq.(2.54) is composed of two parts corresponding to the two types of point defects. Also according to the defect chemistry, adding x mol Y_2O_3 into ZrO_2 can generate $2x$ mol $Y_M^{'}$ and x mol $V_O^{\bullet\bullet}$, therefore:

$$c_D\left(\frac{\Delta M}{\overline{M}}\right)^2 = 2x\left(\frac{\Delta M}{\overline{M}}\right)^2_{Y-solute} + x\left(\frac{\Delta M_{O-Vacancies}}{\overline{M}}\right)^2_{O-Vacancies}, \quad (2.57)$$

where $\overline{M}$ is the average atomic weight in a unit cell. For oxygen vacancies [85]:

$$\frac{\Delta M_{O-Vacancies}}{\overline{M}} = -\frac{M_O}{\overline{M}} - 2, \quad (2.58)$$

where the term -2 arises because the number of broken bonds at the vacancy is twice the number of bonds per atom [83,85]. Due to the small difference between the atomic mass of Y and Zr, the contribution from the cation sites is minor compared with that from the anion sites in YSZ.

2.6.2 Effect of yttria concentration

From part 2.6.1, it is known that the oxygen vacancies in YSZ are the most effective scattering sites for phonons. The yttria concentration determines the oxygen vacancy concentration in YSZ and thus influences the thermal conductivity of YSZ. From Eq.(2.54) it is expected that the thermal conductivity decreases monotonously with increasing yttria concentration. However, the experimental results show no further decrease of thermal conductivity when yttria concentration is higher than 9 mol% [86], which is attribute to the formation of defect associates at high yttria concentrations.

On the other hand, with an increase in the yttria concentration, there is a change of phase composition in YSZ, from monoclinic, via a mixture of cubic and tetragonal, to fully stabilised cubic phase. Different phases have different lattice parameters and various physical properties, i.e., Young's modulus, density, etc., which might also have influences on the thermal conductivity. The phase change might be another reason for the reduction of thermal conductivity with increasing yttria concentration.

In all, the introduction of yttria into ZrO_2 changes the oxygen vacancy concentration, as well as the phase composition of YSZ. An overall picture showing the effect of yttria content on thermal conductivity of YSZ is shown in Figure 2.18.

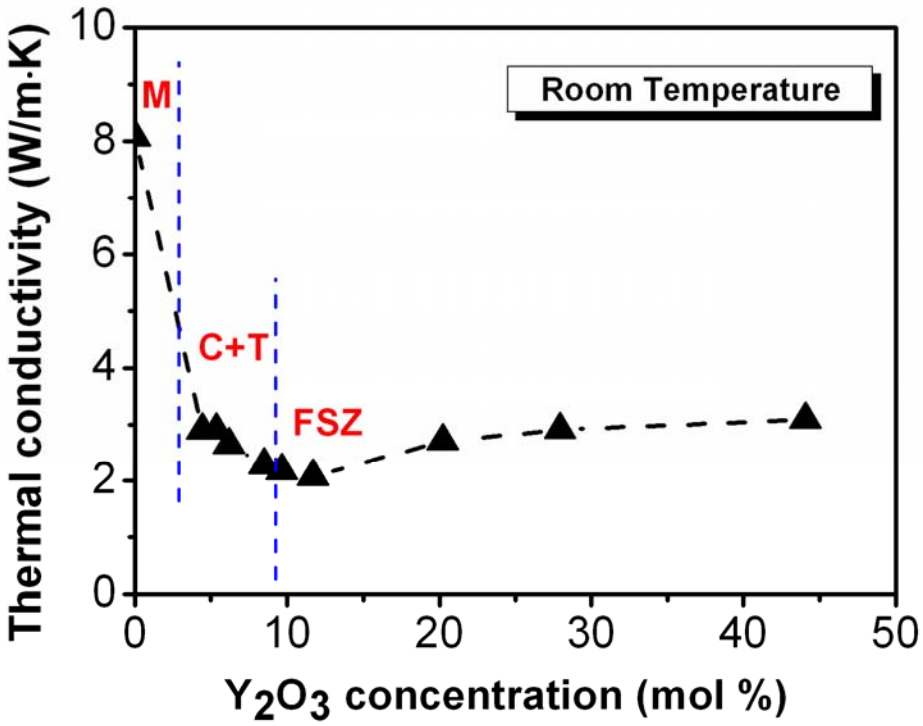

Figure 2.18 Effect of yttria content on thermal conductivity of YSZ. Phases are indicated, where *M* represents monoclinic, *C* cubic and *T* tetragonal. After [80,86].

2.6.3 Effect of grain size

As stated in 2.5.3, grain boundaries in the polycrystalline material scatter the phonons and decrease the phonon mean free path. In YSZ, however, due to its highly defective crystal structure and the small phonon mean free path, the effect of phonon-grain boundary scattering is not significant. Only when the grain size is very small, i.e., tens of nanometers, the grain boundary effect can be observed. For example, Raghavan *et al.* [87] found that in 5.8 wt% YSZ, a grain size of around 80 nm is still not small enough to observe any reduction of thermal conductivity.

Yang *et al.* [88] studied the grain boundary effect in nanocrystalline YSZ with grain size ranging from 10 to 100 nm. As shown in Figure 2.19(a), a rapid decrease of thermal conductivity can be observed when grain size is smaller than 40 nm. They proposed a general formalism for determining the grain boundary thermal resistance in polycrystalline materials.

Figure 2.19(b) shows the temperature profile across a polycrystalline material with a grain width of d in response to an applied heat flux q. The temperature drop across a single grain is:

$$T^* = T_0 + T_{GB}, \tag{2.59}$$

where T_0 is the temperature drop across a single grain interior region, and T_{GB} is the average temperature discontinuity at each grain boundary. According to Fourier's law, the effective thermal conductivity of a polycrystalline material can be defined as:

$$k = \frac{-qd}{T_0 + T_{GB}} = \frac{-qd}{\frac{-qd}{k_0} - qR_{GB}} = \frac{k_0}{1 + \frac{k_0 R_{GB}}{d}}, \tag{2.60}$$

where k_0 is the bulk or single-crystal thermal conductivity and R_{GB} is the grain boundary thermal resistance, which is the reciprocal of thermal conductance by $G_{GB} = \frac{1}{R_{GB}}$.

However, when the experimental results in Figure 2.19(a) are fitted using Eq.(2.60), the k_0 values obtained from fitting deviate from literature values by 20%. To solve this problem, the authors modified Eq.(2.60) by introducing an additional temperature factor β. The effective thermal conductivity is therefore written as:

$$k = \frac{-qd}{T_0 + \beta + T_{GB}} = \frac{k_0}{1 + \mu + \frac{k_0}{G_{GB} d}}, \tag{2.61}$$

where μ is a dimensionless parameter equal to β/T_0.

Using the reference values of k_0 and fitting k vs. d (Figure 2.19(a)) to Eq.(2.61), the thermal conductance of YSZ grain boundary is obtained, as shown in Figure 2.20. G_{GB} increases with increasing temperature and then plateaus. The room temperature thermal resistance is around 4.5×10^{-9} m^2·K/W, which is quite low compared with materials like $Si_{0.8}Ge_{0.2}$ [89]. From the practical side, using nanocrystalline YSZ to decrease the thermal conductivity can not be effective because of the rapid grain growth above 900 ºC [90], which is much lower than the operating temperatures for TBCs applications.

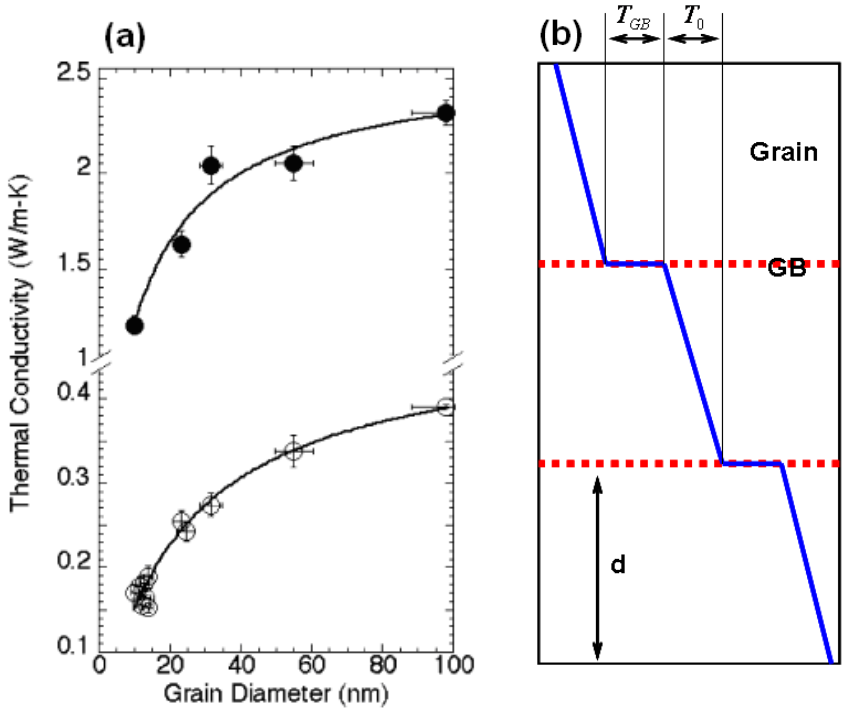

Figure 2.19 (a) Thermal conductivity of nanocrystalline YSZ as a function of grain size at 25 K (open circles) and 480 K (solid circles); (b) Schematic representation of the one-dimensional temperature profile across a polycrystalline sample in response to an applied heat flux (blue line). After [88].

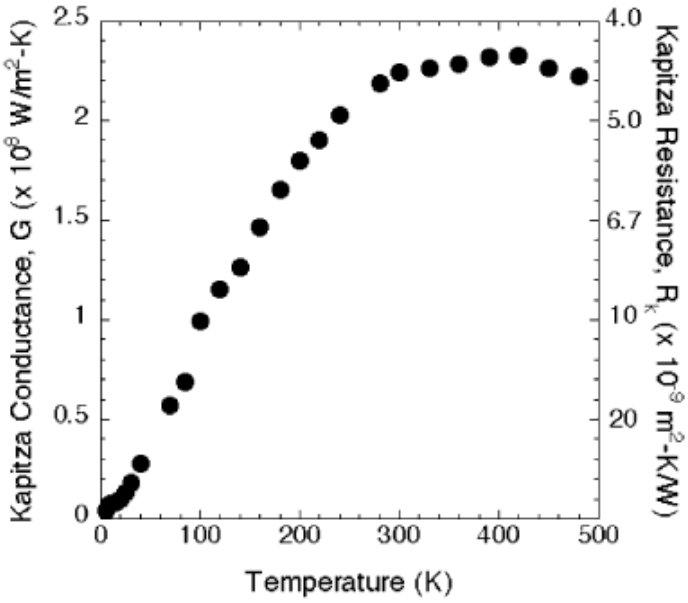

Figure 2.20 Grain boundary thermal conductance G_{GB} and resistance R_{GB} for YSZ derived from the measured grain-size dependent thermal conductivity data fit to Eq.(2.61). [88]

2.6.4 Effect of porosity

The presence of porosity has the greatest effect in decreasing the thermal conductivity of a material. The reduction of thermal conductivity depends on not only the volume fraction of pores but also the spatial distribution and the shape of the pores. An empirical expression of the effective thermal conductivity, k_{eff}, is written as [91]:

$$k_{eff} = k\left(1 - c\Phi - d\Phi^2 .....\right), \tag{2.62}$$

where Φ is the volume fraction of pores, c and d are constants describing the pore shape and pore distribution.

For sintered bulk YSZ, the pores can be treated as randomly distributed spheres. Over a range of volume fraction, the constant c then has a value of ~2.5 [91] the effective thermal conductivity can be approximated by:

$$k_{porous} = k_{dense}\left(1 - 2.5\Phi\right). \tag{2.63}$$

On the other hand, from Maxwell model [92], another expression of the effective thermal conductivity can be obtained, written as:

$$k_{porous} = k_{dense}\left(\frac{1-\Phi}{1+0.5\Phi}\right). \tag{2.64}$$

The other frequently used relationship between thermal conductivity of porous sample and fully-dense sample is [93]:

$$k_{porous} = k_{dense}\left(1 - \frac{4}{3}\Phi\right). \tag{2.65}$$

The above three equations are compared, as shown in Figure 2.21. It can be seen that Eq.(2.64) and (2.65) give very close values for zero-porosity correction whereas Eq.(2.63) is quite different with the other two. When the volume fraction of pores is low (less than 10%), Eq.(2.64) and (2.65) are almost identical.

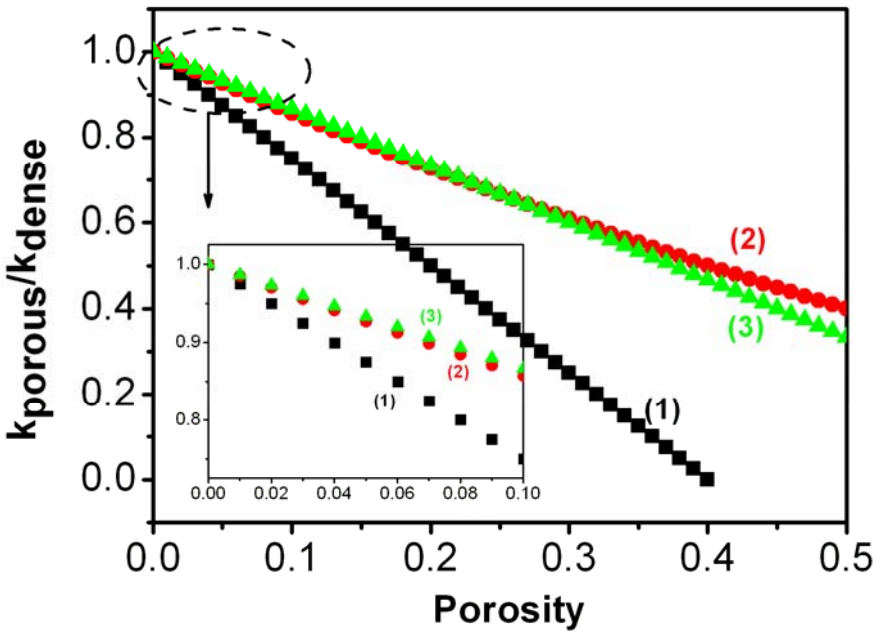

Figure 2.21 Effect of porosity on thermal conductivity of bulk sintered samples. Line (1) to (3) describe the relationship in Eq.(2.63) to (2.65) respectively.

2.6.5 Effect of co-doping

Dopants are important to zirconia on both stabilising its tetragonal or cubic phase and decreasing its thermal conductivity. Additions of other metal oxides into YSZ can result in further thermal conductivity reduction. The mechanisms of the reduction of thermal conductivity are different according to the valence of the metal oxides. For example, additions of trivalent oxides into YSZ generate more oxygen vacancies, which strongly scatter phonons, and thus decrease the thermal conductivity. Additions of tetravalent oxides into YSZ do not usually generate any vacancy. The reduction of thermal conductivity is due to the substitutional defects, which are less effective in decreasing thermal conductivity than vacancies [94]. Additions of pentevalent oxides into YSZ decrease the oxygen vacancy concentration but they still result in a thermal conductivity close to or lower than that of YSZ. Both the oxygen vacancies and the substitutional defects are responsible for the reduction of thermal conductivity, depending on the relative amount between the pentevalent oxides and yttria. Details of the effect of doping trivalent, tetravalent and pentevalent oxides are described in the following paragraphs.

2.6.5.1 Trivalent oxides: Sc_2O_3 and Yb_2O_3

Doping a small amount of trivalent oxides into YSZ can further decrease the thermal conductivity by increasing the oxygen vacancy concentration in the ternary solid solutions. It is predictable that the effect of doping trivalent oxides into YSZ is similar to that of increasing the yttria concentration, as illustrated in Figure 2.18.

Huang *et al.* [94] doped 3.9 mol% YSZ with 5 mol% Sc_2O_3 or Yb_2O_3 and found a reduction of room temperature thermal conductivity from 3.99 W/m·K for YSZ to 2.35 W/m·K for Sc-YSZ and 2.30 W/m·K for Yb-YSZ. The reduction of thermal conductivity is more significant in Yb-YSZ than in Sc-YSZ at high temperatures. For example, the thermal conductivity at 800ºC decreases from 4.51 W/m·K for YSZ to 3.5 W/m·K for Sc-YSZ and to 1.9 W/m·K for Yb-YSZ. The authors attribute the lower thermal conductivity in Yb-YSZ to the larger atomic mass of Yb (173.04 g/mol) than that of Sc (44.96 g/mol). However, it is noticeable that the amount of monoclinic phase is different in YSZ (46 mol%), Sc-YSZ (6 mol%) and Yb-YSZ (0 mol%), which could also be a reason for the decreased thermal conductivity.

2.6.5.2 Tetravalent oxides: TiO_2, CeO_2 and HfO_2

TiO_2 has a solution limitation in ZrO_2 of 40 mol% [95] and in YSZ of 20 mol% [96-98]. Miyazaki [99] studied the effect of doping TiO_2 into 3 mol% YSZ and found a continuous reduction of thermal conductivity with increasing TiO_2 content. The room temperature thermal conductivity decreases from ~ 4.0 W/m·K for 3 mol% YSZ to ~ 2.1 W/m·K for 20 mol% TiO_2 doped YSZ, as shown in Figure 2.22. The authors briefly attributed the reduction of thermal conductivity to the mass defect at the cation sites, caused by the substitution of Y or Zr by Ti. However, with an increase in the TiO_2 content, the phase of the solid solution changes from a mixture of monoclinic, tetragonal and cubic in 3YSZ and 4 mol% TiO_2-3YSZ, a mixture of tetragonal and cubic for 8 - 16 mol% TiO_2-3YSZ, to a tetragonal single phase for 20 mol% TiO_2-3YSZ. How the phase change influences the thermal conductivity is unknown.

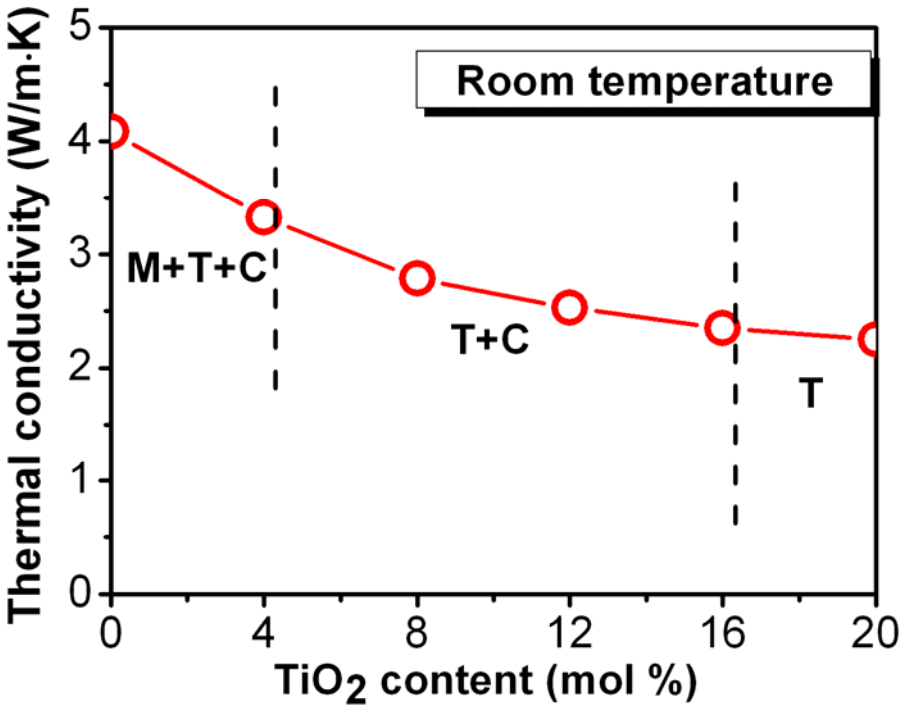

Figure 2.22 Thermal conductivity of TiO_2-3 mol% yttria-stabilized zirconia ceramics at room temperature as a function of TiO_2 content. Phases are indicated: M represents monoclinic, T tetragonal and C cubic. After [99].

Reduction of thermal conductivity by doping CeO_2 into YSZ has also been reported by several studies. Huang *et al*. [94] added 5 mol% ceria into 7 wt% YSZ and found the thermal conductivity was lowered from 3.99 W/m·K (for YSZ) to 3.23 W/m·K at room temperature, and from 3.96 W/m·K to 3.78 W/m·K at 600 ºC. However, the introduction of ceria significantly decreases the fraction of monoclinic phase in 7 wt% YSZ. Again the phase composition difference might be responsible for the reduction of thermal conductivity.

HfO_2 has similar physical and chemical properties with ZrO_2 and it has a complete solubility with ZrO_2. Winter and Clarke [100] studied the thermal conductivity of HfO_2-YSZ solid solutions over the whole composition range, from YSZ to yttria-stabilized hafnia (YSH). The high concentration of yttria (24.6 m/o $YO_{1.5}$) leads to fully cubic phase for all compositions. They found the solid solution alloying (intermixing of HfO_2 and ZrO_2) leads to lower thermal conductivity than either YSZ or YSH. Within the

whole composition range the thermal conductivity is almost independent on temperature, as shown in Figure 2.23(a). For a clear comparison of the composition dependence, the thermal conductivity is converted to the thermal resistance, as shown in Figure 2.23(b). The "alloyed" compositions have thermal resistances higher than those suggested from the simple rule-of-mixture between the end members of YSZ and YSH (the dash line in Figure 2.23(b)).

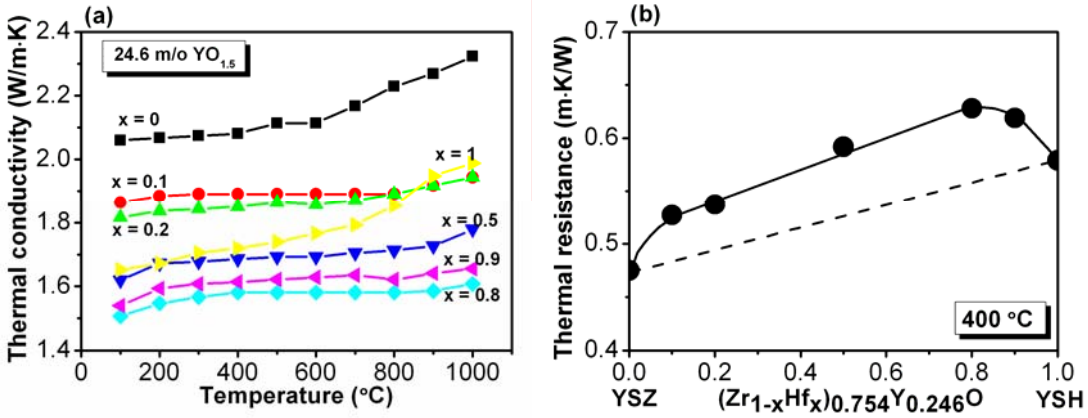

Figure 2.23 (a) Temperature dependence of the thermal conductivity for the solid solution, $(Zr_{1-x}Hf_x)_{0.754}Y_{0.246}O$, as a function of hafnia concentration. (b) Thermal resistance at 400 ºC across the solid solution series with 24.6 m/o $YO_{1.5}$. After [100].

To understand why the intermixing of HfO_2 and ZrO_2 leads to lower thermal conductivity than either YSZ or YSH, the authors employed several models which have been developed to account for alloying effects on thermal conductivity. However, none of them is entirely successful for explaining the experimental observations. First, considering the Umklapp and the phonon-defect scattering, the thermal conductivity is described in Eq.(2.50). The thermal conductivity decreases with increasing temperatures until reaching a minimum value given by $k_{\min} = \frac{A}{3T_1}$. T_1 is an effective temperature that for any given material is a constant [77]. The coefficient A is dependent on the atomic mass M, the number of atoms per unit cell volume m and the Debye temperature Θ_D, and other fundamental constants, in the form of:

$$A = \frac{Q}{(2\pi)^3} M \left(\frac{\Omega_0}{m}\right)^{1/3} \frac{k_B^3 \Theta_D^3}{\hbar^3 \gamma^2}, \tag{2.66}$$

where Q is a numerical constant. Considering the dependence of the Debye temperature on atomic mass, k_{min} is dependent on the atomic mass as $M^{-1/2}$. This predicts a monotonic decrease with increasing HfO_2 concentration due to the larger atomic mass of Hf, which contradicts to the experimental observations.

The second consideration is the phonon scattering from the alloy element as a result of both the mass difference and the ionic size difference. Due to the fixed yttria concentration in the solid solutions, the ionic size effect is ignored. Then the phonon scattering coefficient, Γ, of a random mixture of two different atoms Hf and Zr, is expressed in terms of the concentration and atomic mass as:

$$\Gamma = \frac{x(1-x)\left(M_{Hf} - M_{Zr}\right)^2}{\left[xM_{Hf} + (1-x)M_{Zr}\right]^2}. \tag{2.67}$$

According to Eq.(2.67), the scattering coefficient increases with increasing HfO_2 concentration, reaching its highest value when x is around 0.34, and then decreases afterward. Because the elastic modulus and the volume of the unit cell for the solid solutions are independent of composition, the thermal resistance is proportional to the scattering coefficient [100]. This can explain the nonlinear variation of thermal conductivity as a function of HfO_2 concentration, however, it failed to explain why the highest thermal resistance is observed when $x = 0.8$.

Although there remains unclear issue, this work suggests that solid solution alloying can be a viable strategy for further reducing the thermal conductivity of solids.

2.6.5.3 Pentavalent oxides: Ta_2O_5 and Nb_2O_5

When pentavalent oxides and yttria are doped into zirconia, the defect chemistry is described by the following equation [101]:

$$xZ_2O_5 + yY_2O_3 = 2xZ_{Zr}^{\bullet} + 2yY_{Zr}^{'} + (5x+3y)O_O + (y-x)V_O^{\bullet\bullet}. \tag{2.68}$$

Therefore the final ternary solid solutions can have various concentrations of oxygen vacancies and substitutional defects depending on the relative amount of pentavalent oxides and yttria.

Raghavan *et al.* [102] studied the thermal conductivities of Ta_2O_5 and Nb_2O_5 co-doped YSZ and found some interesting phenomena which contradict, to some extent, to the theoretical predictions. First, when Nb_2O_5 and Y_2O_3 are equimolar ($x = y$), oxygen vacancies are not generated in the ternary solid solutions. Plus the similar atomic mass between Nb (92.91) and Zr (91.22), the Nb_2O_5-Y_2O_3-ZrO_2 solid solution, $YNbO_4$, should have a thermal conductivity that is similar to that of pure monoclinic zirconia. On the other hand, due to the large difference in atomic mass between Ta (180.95) and Zr, the equimolar Ta_2O_5-Y_2O_3 co-doped ZrO_2, $YTaO_4$, should have much lower thermal conductivity than a pure monoclinic zirconia or $YNbO_4$. However, as shown in Figure 2.24(a), the thermal conductivity of $YNbO_4$ is much lower than that of pure monoclinic ZrO_2, whereas thermal conductivity of $YTaO_4$ is lower, but not as significantly as expected, than that of $YNbO_4$. Second, in yttria-excess samples, oxygen vacancies are generated in the ternary solid solutions. In Nb_2O_5 co-doped YSZ, due to the similar atomic mass between Nb and Zr, it should have similar value with that of YSZ having the same concentration of oxygen vacancies. In Ta_2O_5 co-doped YSZ, the thermal conductivity should be lower than that of YSZ with same concentration of oxygen vacancies due to additional scattering because of the large mass difference between Ta and Zr. However, as shown in Figure 2.24(b), the Nb-YSZ sample has lower thermal conductivity than those Ta-YSZ samples.

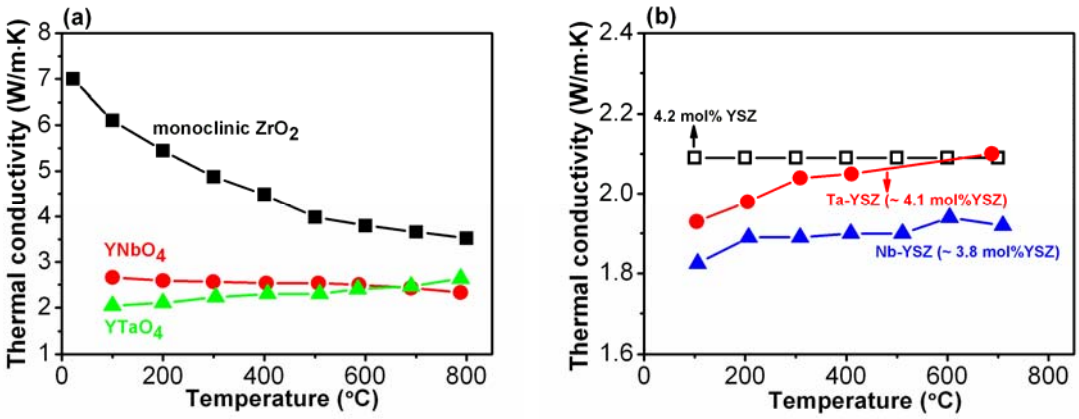

Figure 2.24 (a) Comparison of the thermal conductivities of pure monoclinic zirconia with that of the Ta or Nb co-doped YSZ containing no oxygen vacancies. (b) Thermal conductivities of the Ta or Nb co-doped YSZ containing oxygen vacancies. The concentrations of oxygen vacancies in the co-doped samples are indicated in the blankets. After [102].

The discrepancies between theoretical predictions and experimental observations might due to the underestimation of the ionic size effect, as well as the different phase compositions in those samples. However, it does point out that the phonon scattering due to mass difference alone is inadequate to predict the thermal conductivity of the co-doped YSZ solid solutions.

2.7 Techniques for thermal conductivity measurement

2.7.1 Axial flow methods [103]

In steady-state conduction, the thermal conductivity is defined as the heat flux over the temperature gradient. Thermal conductivity therefore can be obtained from measuring the heat flux and the temperature difference across the sample. Axial flow methods are based on this concept.

One of the most widely used axial flow methods is the comparative cut bar method (ASTM E1225). The principle of the measurement lies with passing the heat flux through a reference sample with known thermal conductivity (k_R) and the test sample (k_S), and comparing their temperature gradients which are inversely proportional to their thermal conductivities. To minimize the heat loss, the sample is commonly sandwiched between two reference samples. A schematic of the comparative cut bar test method is shown in Figure 2.25. The thermal conductivity of the sample can be calculated as:

$$\frac{Q}{A} = k_S \frac{\Delta T_S}{L} = k_R \frac{\Delta T_1 + \Delta T_2}{2} \frac{1}{L}, \tag{2.69}$$

where Q is the heat input and A is the cross-section area.

The steady-state measurements have been long established. They are easy, direct and accurate at low temperatures. However, the heat losses are difficult to control at high temperatures, which decreases the accuracy. The measurement also takes long time and requires a large specimen.

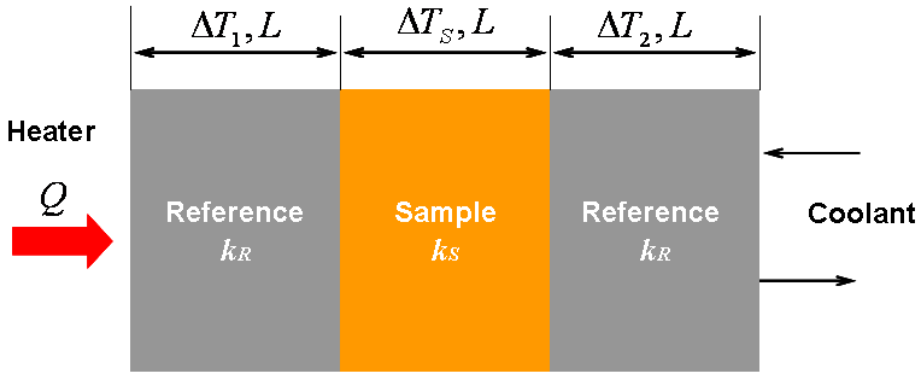

Figure 2.25 Schematic of the comparative cut bar test method for thermal conductivity measurement.

2.7.2 Laser flash technique [104, 105]

Laser flash is a transient-state method of measuring the thermal diffusivity/conductivity of materials. It was proposed by Parker *et al.* [104] in 1961 and now it has become a most widely used method for high temperature thermal conductivity measurement.

A schematic view of the laser flash system is shown in Figure 2.26. During the measurement, a high-intensity short-duration laser pulse is applied to the front surface of the sample. The temperature rise at the backside is measured by an infra-red detector. The thermal diffusivity (α) can be determined from the temperature versus time curve at the rear surface by:

$$\alpha = \frac{1.38d^2}{\pi^2 t_{0.5}} = \frac{0.1388d^2}{t_{0.5}}, \tag{2.70}$$

where d is the sample thickness and $t_{0.5}$ is the time required for the back surface to reach half of the maximum temperature rise. The thermal diffusivity value can be converted to thermal conductivity by multiplying the specific heat capacity (C_p) and the density (ρ):

$$k = \alpha C_p \rho . \tag{2.71}$$

The thermal diffusivity measurement by laser flash technique is fast and convenient, especially at high temperatures. Only a small amount of material is needed for the measurement. However, depending on the flash duration, a minimum thickness of the sample is required. The sample should be thick enough to guarantee that the time the

temperature begins to raise at the back surface is longer than the flash duration. For a low thermal diffusivity material, the satisfactory thickness is about 1 mm.

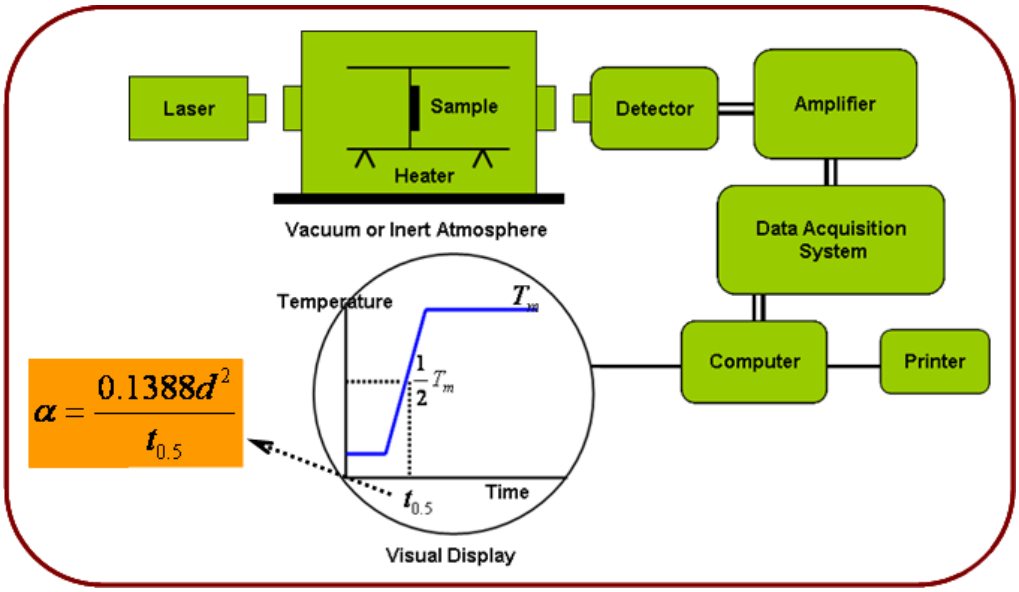

Figure 2.26 A schematic view of the laser flash system.

2.7.3 Micro-Raman scattering [106]

Micro-Raman scattering is a noncontact and non-destructive method to measure thermal conductivity, proposed by Périchon *et al.*. The concept of this technique is based on two complementary effects in micro-Raman spectroscopy. The first effect is the local heating in the surface layer caused by the laser beam focused on the sample. It causes a temperature rise, which is directly related to the sample's thermal conductivity. The second effect is the shift of the Raman peak with temperature, which can be used to obtain the local temperature rise.

When the sample thickness is far (at least one order) larger than the heat source diameter, the distribution of isotherms is hemispherical. Neglecting the heat losses in the air, a linear relationship between the heating power P, the local temperature T_j and the thermal conductivity k can be obtained:

$$k = \frac{2P}{\pi a \Delta T} = \frac{2P}{\pi a (T_j - T_b)}, \tag{2.72}$$

where T_b is the bulk temperature and a is the heating source diameter. During the measurement, a low laser power P_L, by which no surface heating is induced, is applied to the sample to calibrate the relationship between Raman peak shift and the temperature. After that, Raman measurement is carried out at given laser power. From the Raman peak position, the local temperature T_j is obtained from the peak shift-temperature relationship. The local temperature rise and thus the thermal conductivity of the sample can be obtained from Eq.(2.72).

This technique can be applied to bulk or layered materials whose thickness is larger than the laser beam diameter. The main random error is from the uncertainty on the Raman peak position, which is estimated to be ± 0.5 cm^{-1}, leading to a relative error on the measured thermal conductivity of 16%. Improvement of Raman spectra acquisition can enhance the accuracy of this method.

Other techniques, for example, 3ω method [107], thermography [86], time-domain thermoreflectance (TDTR) [108], are also widely used to determine the thermal conductivity of materials, especially for thin films. The details of those techniques can be found in relevant references.

2.8 Summary of part II

In part II of this chapter, the fundamentals of the thermal conduction mechanism of YSZ are reviewed. The information obtained is summarized as the following:

(1) YSZ has a temperature independent low thermal conductivity which is attributed to the existence of oxygen vacancies;

(2) Thermal conductivity of YSZ depends on the yttria concentration. The lowest thermal conductivity is obtained in 8 mol% YSZ, with a value of around 2.2 W/m·K.

(3) The grain boundary effect can be neglected when the average grain size is larger than 100 nm.

(4) Doping other metal oxides into YSZ is an effective method to decrease the thermal conductivity is YSZ. Depending on the valence of the metal, the mechanism of the reduction of thermal conductivity is different.

(5) Laser flash is a convenient method to obtain the thermal diffusivity/conductivity values of YSZ bulk samples.

References

[1] H. Yamamura, S. Takeda and K. Kakinuma, *Relationship between oxide-ion conductivity and dielectric relaxation in Sm-doped CeO_2*, Solid State Ionics **178** (2007) 889-893

[2] J. B. Good enough, *Oxide-ion conductors by design*, Nature **404** (2000) 821-823.

[3] A. J. Moulson and J. M. Herbert, Electroceramics: materials, properties, applications, John Wiley & Sons Ltd, Chichester, 2003, p.45.

[4] D. J. Kim, *Lattice parameters, ionic conductivities, and solubility limits in fluorite-structure MO_2 oxide [M= Hf^{4+}, Zr^{4+}, Ce^{4+}, Th^{4+}, U^{4+}] solid solutions*, Journal of the American Ceramic Society **72** (1989) 1415-1421.

[5] J. A. Kilner and R. J. Brook, *A study of oxygen ion conductivity in doped non-stoichiometric oxides*, Solid State Ionics **6** (1982) 237-252.

[6] D. A. Andersson, S. I. Simak, N. V. Skorodumova, I. A. Abrikosov and B. Johansson, Optimization of ionic conductivity in doped ceria, Proceedings of the National Academy of Sciences 103 (2006) 3518-3521.

[7] A. Orliukas, P. Bohac, K. Sasaki and L. J. Gauckler, *The relaxation dispersion of the ionic conductivity in cubic zirconias*, Solid State Ionics **72** (1994) 35-38.

[8] W. van Gool, Fast ion transport in solids, North-Holland, Amsterdam, 1972, p.201.

[9] M. Pouchard and P. Hagenmuller, Solid electrolytes, Academic Press, New York, 1978, p.191.

[10] M. Mogensen, D. Lybye, N. Bonanos, P. V. Hendriksen and F. W. Poulsen, *Factors controlling the oxide ion conductivity of fluorite and perovskite structured oxides*, Solid State Ionics **174** (2004) 279-286

[11] S. Omar, E. D. wachsman, J. L. Jones and J. C. Nino, *Crystal structure-ionic conductivity relationships in doped ceria systems*, Journal of the American Ceramic Society **92** (2009) 2674-2681.

[12] O. Yamamoto, Y. Arachi, H. Sakai, Y. Takeda, N. Imanishi, Y. Mizutani, M. Kawai and Y. Nakamura, *Zirconia based oxide ion conductors for solid oxide fuel cells*, Ionics **4** (1998) 403-408.

[13] R. J. Stafford, S. J. Rothman and J. L. Routbort, *Effect of dopant size on the ionic conductivity of cubic stabilised ZrO_2*, Solid State Ionics **37** (1989) 67-72

[14] V. V. Kharton, F. M. B. Marques and A. Atkinson, *Transport properties of solid oxide electrolyte ceramics: a brief review*, Solid State Ionics **174** (2004) 135-149.

[15] D. Y. Wang , D. S. Park, J. Griffith and A. S. Nowick, *Oxygen-ion conductivity and defect interactions in yttria-doped ceria*, Solid State Ionics **2** (1981) 95-105.

[16] Y. Arachi, H. Sakai, O. Yamamoto, Y. Takeda and N. Imanishai, *Electrical conductivity of the ZrO_2-Ln_2O_3 (Ln = lanthanides) system*, Solid State Ionics **121** (1999) 133-139.

[17] M. F. Trubelja and V. S. Stubican, *Ionic conductivity of the fluorite-type Hafnia-R_2O_3 solid solutions*, Journal of the American Ceramic Society **74** (1991) 2489-2494.

[18] X. Guo and R. Waser, *Electrical properties of the grain boundaries of oxygen ion conductors: Acceptor-doped zirconia and ceria*, Progress in Materials Science **51** (2006) 151-210.

[19] Y. M. Chiang, E. B. Lavik and D. A. Blom, *Defect thermodynamics and electrical properties of nanocrystalline oxides: pure and doped CeO_2*, Nanostructured Materials **9** (1997) 633-642.

[20] X. Guo and Z. Zhang, *Grain size dependent grain boundary defect structure: case of doped zirconia*, Acta Materialia **51** (2003) 2539-2547.

[21] M. J. Verkerk, B. J. Middelhuis and A. J. Burggraaf, Effect of grain boundaries on the conductivity of high-purity ZrO_2-Y_2O_3 ceramics, Solid State Ionics 6 (1982) 159-170.

[22] X. Guo and J. Maier, *Grain boundary blocking effect in zirconia: A Schottky barrier analysis*, Journal of Electrochemical Society **148** (2001) E121-126.

[23] S. P. S. Badwal and J. Drennan, *Yttria-zirconia: effect of microstructure on conductivity*, Journal of Materials Science **22** (1987) 3231-3239.

[24] S. P. S. Badwal and J. Drennan, *Grain boundary resistivity in Y-TZP materials as a function of thermal history*, Journal of Materials Science **24** (1989) 88-96

[25] A. E. Hughes and B. A. Sexton, *XPS study of an intergranular phase in yttria-zirconia*, Journal of Materials Science **24** (1989) 1057-1061.

[26] A. E. Hughes and S. P. S. Badwal, *Impurity segregation study at the surface of yttria-zirconia electrolytes by XPS*, Solid State Ionics **40-41** (1990) 312-315

[27] S. P. S. Badwal and J. Drennan, *Evaluation of conducting properties of yttria-zirconia wafers*, Solid State Ionics **40-41** (1990) 869-873.

[28] S. P. S. Badwal, F. T. Ciacchi and R. H. J. Hannink, *Relationship between phase stability and conductivity of yttria tetragonal zirconia*, Solid State Ionics **40-41** (1990) 882-885.

[29] A. E. Hughes and S. P. S. Badwal, *Impurity and yttrium segregation in yttria-tetragonal zirconia*, Solid State Ionics **46** (1991) 265-274.

[30] S. P. S. Badwal, *Zirconia-based solid electrolytes: microstructure, stability and ionic conductivity*, Solid State Ionics **52** (1992) 23-32.

[31] S. P. S. Badwal, *Effect of micro- and nano-structures on the properties of ionic conductors*, Solid State Ionics **70-71** (1994) 83-95.

[32] F. T. Ciacchi, K. M. Crane and S. P. S. Badwal, *Evaluation of commercial zirconia powders for solid oxide fuel cells*, Solid State Ionics **73** (1994) 49-61.

[33] S. P. S. Badwal, F. T. Ciacchi, M. V. Swain and V. Zelizko, *Creep deformation and the grain-boundary resistivity of tetragonal zirconia polycrystalline materials*, Journal of the American Ceramic Society **73** (1990) 2505-2507.

[34] S. P. S. Badwal and A. E. Hughes, *The effects of sintering atmosphere on impurity phase formation and grain boundary resistivity in Y_2O_3-fully stabilized ZrO_2*, Journal of the European Ceramic Society **10** (1992) 115-122.

[35] M. Gödickemeier, B. Michel, A. Orliukas, P. Bohac, K. Sasaki, L. Gauckler, H. Heinrich, P. Schwander, G. Kostorz, H. Hofmann and O. Frei, *Effect of intergranular glass films on the electrical conductivity of 3Y-TZP*, Journal of Materials Research **9** (1994) 1228-1240.

[36] M. Kleitz, L. Dessemond and M. C. Steil, *Model for ion-blocking at internal interfaces in zirconias*, Solid State Ionics **75** (1995) 107-115.

[37] X. Guo and R. Z. Yuan, *On the grain boundaries of ZrO_2-based solid electrolyte*, Solid State Ionics **80** (1995) 159-166.

[38] H. Yamamura, N. Utsunomiya, T. Mori and T. Atake, *Electrical conductivity in the system ZrO_2-Y_2O_3-Sc_2O_3*, Solid State Ionics **107** (1998) 185-189.

[39] S. P. S. Badwal, F. T. Ciacchi, S. Rajendran and J. Drennan, *An investigation of conductivity, microstructure and stability of electrolyte compositions in the system 9 mol% (Sc_2O_3-Y_2O_3)-ZrO_2 (Al_2O_3)*, Solid State Ionics **109** (1998) 167-186.

[40] C. C. Appel and N. Bonanos, *Structural and electrical characterization of silica-containing yttria-stabilised zirconia*, Journal of the European Ceramic Society **19** (1999) 847-851.

[41] J. H. Lee, T. Mori, J. G. Li, T. Ikegami, M. Komatsu and H. Haneda, *Improvement of grain-boundary conductivity of 8 mol% yttria-stabilized zirconia by precursor scavenging of siliceous phase*, Journal of the Electrochemical Society **147** (2000) 2822-2829.

[42] J. H. Lee, T. Mori, J. G. Li, T. Ikegami, J. Drennan and D. Y. Kim, *Scavenging of siliceous grain-boundary phase of 8-mol%-ytterbia-stabilized zirconia without additive*, Journal of the American Ceramic Society **82** (2001) 2734-2736.

[43] J. H. Lee, T. Mori, J. G. Li, T. Ikegami, J. Drennan and D. Y. Kim, *Precursor scavenging of the resistive grain-boundary phase in 8 mol% yttria-stabilized zirconia: effect of trace concentrations of SiO_2*, Journal of Materials Research **16** (2001) 2377-2383.

[44] J. H. Lee, T. Mori, J. G. Li, T. Ikegami, J. Drennan and D. Y. Kim, *Precursor scavenging of resistive grain-boundary phase in 8 mol% ytterbia-stabilized zirconia*, Journal of the Electrochemical Society **149** (2002) J35-J40.

[45] J. H. Lee, J. H. Lee and D. Y. Kim, *Inhomogeneity of grain-boundary resistivity in calcia-stabilized zirconia*, Journal of the American Ceramic Society **85** (2002) 1622-1624.

[46] Y. S. Jung, J. H. Lee, J. H. Lee, D. Y. Kim, *Liquid-phase redistribution during sintering of 8 mol% yttria-stabilized zirconia*, Journal of the European Ceramic Society **23** (2003) 499-503.

[47] M. C. Martin and M. L. Mecartney, *Grain boundary ionic conductivity of yttrium stabilized zirconia as a function of silica content and grain size*, Solid State Ionics **161** (2003) 67-79.

[48] X. Guo, *Physical origin of the intrinsic grain-boundary resistivity of stabilized-zirconia: role of the space-charge layers*, Solid State Ionics **81** (1995) 235-242

[49] X. Guo, *Space-charge conduction in yttria and alumina codoped-zirconia*, Solid State Ionics **96** (1997) 247-254.

[50] X. Guo, W. Sigle, J. Fleig and J. Maier, *Role of space charge in the grain boundary blocking effect in doped zirconia*, Solid State Ionics **154-155** (2002) 555-561.

[51] X. Guo, *Low temperature stability of cubic zirconia*, Physica Status Solidi (a) **177** (2000) 191-201.

[52] X. Guo, *Defect structure modification in zirconia by alumina*, Physica Status Solidi (a) **183** (2001) 261-271.

[53] X. Guo, *Size dependent grain-boundary conductivity in doped zirconia*, Computational Materials Science **20** (2001) 168-176.

[54] J. C. M'Peko, D. L. Spavieri and M. F. de Souza, *In situ characterization of the grain and grain-boundary electrical responses of zirconia ceramics under uniaxial compressive stresses*, Applied Physics Letters **81** (2002) 2827-2829.

[55] J. C. M'Peko and M. F. de Souza, *Ionic transport in polycrystalline zirconia and Frenkel's space-charge layer postulation*, Applied Physics Letters **83** (2003) 737-739.

[56] X. Guo, *Roles of alumina in zirconia for functional applications*, Journal of the American Ceramic Society **86** (2003) 1867-1873.

[57] X. Guo and Y. Ding, *Grain boundary space charge effect in zirconia*, Journal of the Electrochemical Society **151** (2004) J1-J7.

[58] X. Guo, S. Mi and R. Waser, *Nonlinear electrical properties of grain boundaries in oxygen ion conductors: acceptor-doped ceria*, Electrochemical and Solid-State Letters **8** (2005) J1-J3.

[59] J. Fleig and J. Maier, *Finite-element calculations on the impedance of electroceramics with highly resistive grain boundaries: I, Laterally inhomogenerous grain boundaries*, Journal of the American Ceramic Society **82** (1999) 3485-3493.

[60] M. M. McGibbon, N. D. Browning, M. F. Chisholm, A. J. McGibbon, S. J. Pennycook, V. Ravikumar and V. P. Dravid, *Direct determination of grain boundary atomic structure in $SrTiO_3$*, Science **266** (1994) 102-104.

[61] N. D. Browning, J. P. Buban, H. O. Moltaji, S. J. Pennycook, G. Duscher, K. D. Johnson, R. P. Rodrigues and V. P. Dravid, *The influence of atomic structure on the formation of electrical barriers at grain boundaries in $SrTiO_3$*, Applied Physics Letters **74** (1999) 2638-2640.

[62] R. F. Klie and N. D. Browning, *Atomic scale characterization of oxygen vacancy segregation at $SrTiO_3$ grain boundaries*, Applied Physics Letters **77** (2000) 3737-3739.

[63] H. Chang, Y. Choi and J. D. Lee, *Atomic and electronic structures of doped grain boundaries in $SrTiO_3$*, Applied Physics Letters **81** (2002) 3564-3566.

[64] M. Kim, G. Duscher, N. D. Browning, K. Sohlberg, S. T. Pantelides and S. J. Pennycook, *Nonstoichiometry and the electrical activity of grain boundaries in $SrTiO_3$*, Physical Review Letters **86** (2001) 4056-4059.

[65] S. L. Hwang and I. W. Chen, *Grain size control of tetragonal zirconia polycrystals using the space charge concept*, Journal of the American Ceramic Society **73** (1990) 3269-3277.

[66] J. Fleig, S. Rodewald and J. Maier, *Microcontact impedance measurements of individual highly resistive grain boundaries: General aspects and application to acceptor-doped $SrTiO_3$*, Journal of Applied Physics **87** (2000) 2372-2381.

[67] J. R. MacDonald, *Impedance Spectroscopy- Emphasizing Solid Materials and Systems*, Wiley, New York, 1987.

[68] J. G. Fletcher, A. R. West and J. T. S. Irvine, *The AC impedance response of the physical interface between yttria-stabilized zirconia and $YBa_2Cu_3O_{7-x}$*, Journal of the Electrochemical Society **142** (1995) 2650-2654.

[69] S. T. Amaral and I. L. Muller, *Effect of silicate on passive films anodically formed on iron in alkaline solution as studied by electrochemical impedance spectroscopy*, Corrosion **55** (1999) 17-23.

[70] J. Fleig, *The grain boundary impedance of random microstructures: Numerical simulations and implications for the analysis of experimental data*, Solid State Ionics **150** (2002) 181-193.

[71] M. C. Steil, F. Thevenot and M. Kleitz, *Densification of yttria-stabilized zirconia*, Journal of the Electrochemical Society **144** (1997) 390-398.

[72] J. Fleig and J. Maier, *Finite element calculations of impedance effects at point contacts*, Electrochimica Acta **41** (1996) 1003-1009.

[73] J. Fleig and J. Maier, *The influence of laterally inhomogeneous contacts on the impedance of solid materials: a three-dimensional finite-element study*, Journal of Electroceramics **1** (1997) 73-89.

[74] S. R. Phillpot and A. J. H. McGaughey, *Introduction to thermal transport*, Materials Today **8** (2005) 18-20.

[75] C. Kittel, *Introduction to Solid State Physics*, Wiley Interscience, New York, 1995.

[76] P. G. Klemens, *Thermal Conductivity*, Academic Press, New York, 1969.

[77] P. Mévrel, J. C. Laizet, A. Azzopardi, B. Leclercq, M. Poulain, O. Lavigne and D. Demange, *Thermal diffusivity and conductivity of $Zr_{1-x}Y_xO_{2-x/2}$ (x = 0, 0.084 and 0.179) single crystals*, Journal of the European Ceramic Society **24** (2004) 3081-3089.

[78] M. Roufosse and P. G. Klemens, *Thermal conductivity of complex dielectric crystals*, Physical Review B **7** (1973) 5379-5386.

[79] C. G. Levi, *Emerging materials and processes for thermal barrier systems*, Current Opinion in Solid State and Materials Science **8** (2004) 77-91.

[80] D. R. Clarke and C. G. Levi, *Materials design for the next generation thermal barrier coatings*, Annual Review of Materials Research **33** (2003) 383-417.

[81] D. R. Clarke and S. R. Phillpot, *Thermal barrier coating materials*, Materials Today **8** (2005) 22-29.

[82] P. G. Klemens, *Phonon scattering and thermal resistance due to grain boundaries*, International Journal of Thermophysics **15** (1994) 1345-1351.

[83] J. Wu, N. P. Padture, P. G. Klemens, M. Gell, E. García, P. Miranzo and M. I. Osendi, *Thermal conductivity of ceramics in the ZrO_2-$GdO_{1.5}$ system*, Journal of Materials Research **17** (2002) 3193-3200.

[84] P. G. Klemens, *Thermal resistance due to point defects at high temperatures*, Physical Review **119** (1960) 507-509.

[85] P. G. Klemens, *Phonon scattering by oxygen vacancies in ceramics*, Physica B 2**63-264** (1999) 102-104.

[86] J. F. Bisson, D. Fournier, M. Poulain, O. Lavigne and R. Mévrel, *Thermal conductivity of yttria-zirconia single crystals, determined with spatially resolved infrared thermography*, Journal of the American Ceramic Society **83** (2000) 1993-1998.

[87] S. Raghavan, H. Wang, R. B. Dinwiddie, W. D. Porter and M. J. Mayo, The effect of grain size, porosity and yttria content on the thermal conductivity of nanocrystalline zirconia, Scripta Materialia 39 (1998) 1119-1125.

[88] H. S. Yang, G. R. Bai, L. J. Thompson and J. A. Eastman, *Interfacial thermal resistance in nanocrystalline yttria-stabilized zirconia*, Acta Materialia **50** (2002) 2309-2317.

[89] C. W. Nan and R. Birringer, *Determining the Kapitza resistance and the thermal conductivity of polycrystals: a simple model*, Physical Review B **57** (1998) 8264-8268.

[90] G. Soyez, J. A. Eastman, L. J. Thompson, G. R. Bai, P. M. Baldo, A. W. McCormick, R. J. DiMelfi, A. A. Elmustafa, M. F. Tambwe and D. S. Stone, *Grain-size-dependent thermal conductivity of nanocrystalline yttria-stabilized zirconia films grown by metal-organic chemical vapour deposition*, Applied Physics Letters **77** (2000) 1155-1157.

[91] D. R. Clarke, *Materials selection guidelines for low thermal conductivity thermal barrier coatings*, Surface and Coating Technology **163-164** (2003) 67-74.

[92] J. C. Maxwell, *A treatise on electricity and magnetism*, Dover Publications Inc., New York, 1954, p.57.

[93] C. Wan, W. Zhang, Y. Wang, Z. Qu, A. Du, R. Wu and W. Pan, *Glass-like thermal conductivity in ytterbium-doped lanthanum zirconate pyrochlore*, Acta Materialia **58** (2010) 6166-6172.

[94] X. Huang, D. Wang, M. Lamontagne and C. Moreau, *Experimental study of the thermal conductivity of metal oxides co-doped yttria stabilized zirconia*, Materials Science and Engineering B **149** (2008) 63-72.

[95] F. H. Brown and P. Duwez, *The zirconia-titania system*, Journal of the American Ceramic Society **37** (1954) 129-132

[96] E. Zschech, P. N. Kountouros and G. Petzow, *Synchrotron radiation Ti-KXANES study of TiO_2-Y_2O_3-stabilized tetragonal zirconia polycrystals*, Journal of the American Ceramic Society **76** (1993) 197-201.

[97] F. Capel, C. Moure, P. Duran, A. R. Gonzalez-Elipe and A. Caballero, *Sturcture and electrical behaviour in air of TiO_2-doped stabilized tetragonal zirconia ceramic*s, Applied Physics A **68** (1999) 41-48.

[98] F. Capel, C. Moure, P. Duran, A. R. Gonzalez-Elipe and A. Caballero, *Structure and electrical behaviour in air of TiO_2-doped stabilized tetragonal zirconia ceramics*, Journal of the European Ceramic Society **19** (1999) 765-768.

[99] H. Miyazaki, *Influence of TiO_2 solid solution on the thermal property and ionic conductivity of partially stabilized zirconia*, International Journal of Applied Ceramic Technology **5** (2008) 490-498.

[100] M. R. Winter and D. R. Clarke, *Thermal conductivity of yttria-stabilized zirconia-hafnia solid solutions*, Acta Materialia **54** (2006) 5051-5059.

[101] S. Raghavan, H. Wang, R. B. Dinwiddie, W. D. Porter, R. Vassen, D. Stöver and M. J. Mayo, *Ta_2O_5/Nb_2O_5 and Y_2O_3 co-doped zirconias for thermal barrier coatings*, Journal of the American Ceramic Society **87** (2004) 431-437.

[102] S. Raghavan, H. Wang, W. D. Porter, R. B. Dinwiddie and M. J. Mayo, *Thermal properties of zirconia co-doped with trivalent and pentavalent oxides*, Acta Materialia **49** (2001) 169-179.

[103] http://www.anter.com/TN67.htm

[104] W. J. Parker, R. J. Jenkins, C. P. Butler and G. L. Abbott, *Flash method of determining thermal diffusivity, heat capacity, and thermal conductivity*, Journal of Applied Physics **32** (1961) 1679-1684.

[105] R. Taylor, *Construction of apparatus for heat pulse thermal-diffusivity measurements from 300 – 3000 K*, Journal of Physics E: Scientific Instruments **13** (1980) 1193-1199.

[106] P. Périchon, V. Lysenko, B. Remaki, D. Barbier and B. Champagnon, *Measurement of porous silicon thermal conductivity by micro-Raman scattering*, Journal of Applied Physics **86** (1999) 4700-4702.

[107] D. G. Cahill, *Thermal conductivity measurement from 30 to 750 K: the 3ω method*, Review of Scientific Instruments **61** (1990) 802-808.

[108] D. G. Cahill, *Analysis of heat flow in layered structures for time-domain thermoreflectance*, Review of Scientific Instruments **75** (2004) 5119-5122.

Chapter 3

Electrical properties of YSZ/Al_2O_3 composites

3.1 Introduction

Yttria stabilized zirconia (YSZ) and Al_2O_3 are important ceramic materials and have wide range of applications in industry. Their YSZ/Al_2O_3 composite, which should combine the properties of individual component, might increase the range of its application. For example, the YSZ/Al_2O_3 composite has been proposed as electrolyte for planar Solid Oxide Fuel Cell (SOFC) because of its enhanced mechanical and thermal properties compared with conventional YSZ [1]. On the other hand, owing to the immiscibility of YSZ and Al_2O_3 (the solubility of Al_2O_3 in 8 mol% YSZ is around 1 wt.% when sintered at 1500 °C [2]), YSZ/Al_2O_3 composite is also of scientific interest in understanding the fundamental behaviours of a diphase system [3]. It is also a good system for studying the physical properties of the ceramic/ceramic interface.

Electrical properties of the YSZ/Al_2O_3 composite are not new topics and have been investigated by a number of researchers [1-8]. However, most of the studies have been focused on the effect of adding a small amount of Al_2O_3 (less than 5 wt%) to YSZ [4-8]. A review on the effect of the Al_2O_3 addition on the electrical properties of YSZ grain and grain boundary can be found in Ref. [9] and [10]. It is summarized that the Al_2O_3 addition below the solubility limit decreases the grain boundary conductivity by increasing the Schottky barrier height, while the Al_2O_3 addition above the solubility limit increases the grain boundary conductivity by increasing the grain-to-grain contact area by scavenging SiO_2 from the boundaries between grains [9, 10]. For a much wider

range of composition, most of work has reported the electrical properties of YSZ/Al_2O_3 composite with the Al_2O_3 fraction less than 30 wt% (around 40 vol%). For example, Feighery and Irvine [2] doped up 24 wt% Al_2O_3 into 8 mol% YSZ and found that 10 wt% Al_2O_3 can be added to 8 mol% YSZ without any significant decreases in ionic conducting properties. Further additions of Al_2O_3 cause a rapid decrease in conductivity due to the large volume fraction of insulating Al_2O_3 phase. Mori *et al.* [1] studied the composite with Al_2O_3 content up to 30 wt%, and found the conductivity only decreased less than one order of magnitude.

Although it is predictable that the conductivity of the YSZ/Al_2O_3 decreases with further increase in the Al_2O_3 volume fraction, it is still of interest and importance to study the electrical properties of the composite covering the whole composition range because it can provide valuable information on the diphase system. However, the only work that includes the whole composition range of YSZ/Al_2O_3 composite, limited to the authors' knowledge, is reported by Peko *et al.* [3]. They found a strong influence from the microstructural features on the final electrical response of the composite.

On the other hand, among numerous studies related to the electrical properties of the YSZ/Al_2O_3 composite, the effect of the YSZ/Al_2O_3 interface has been rarely discussed. Kumar *et al.* [11, 12] examined the normalized conductivity (conductivity of a composite/volume fraction of active phase) and proposed that the transport of oxygen ions was enhanced at the YSZ/Al_2O_3 interface because of the creation of space charge regions in the vicinity of the YSZ-Al_2O_3 phase boundary. However, due to the blocking effect of Al_2O_3, the enhancement of conductivity is not obvious. Guo [5] studied the grain boundary resistance in yttria and alumina co-doped zirconia and discussed the effect of the ZrO_2/Al_2O_3 interface. It was proposed the resistance of the Al_2O_3/ZrO_2 interface is reduced because of the Al_2O_3/ZrO_2 interface potential is lower than the grain boundary interface potential of ZrO_2. However, the resistance-reducing effect was not obvious due to the pores and the amorphous phases covering the Al_2O_3 particles [5]. Therefore, a further investigation of the electrical properties of the YSZ/Al_2O_3 interface is desirable.

In this chapter, we studied the electrical properties of the YSZ/Al_2O_3 composite covering a whole composition range. The effect of the YSZ/Al_2O_3 interface is discussed from relaxation frequency analysis coupled with finite element modelling. The purpose of this study is to present an overall picture of the electrical properties of the composite system, and to promote the understanding of the YSZ/Al_2O_3 interface.

3.2 Experiments

8 mol% YSZ powder (average particle size of 0.25 μm, PI-KEM, UK) and α-Al_2O_3 powder (average particle size of 0.1-0.3 μm, PI-KEM, UK) were used as starting materials. The YSZ/Al_2O_3 composite samples with 20, 40, 60, 80, 85, 90% (volume percentage) Al_2O_3 were produced. Appropriate amounts of YSZ and Al_2O_3 powders were mixed by ball milling for 24 hours in 2-propanol, using zirconia balls as grinding media. The resulting mixtures were subsequently dried in air overnight, and then milled by mortar and pestle and passed through a 45-micron sieve. The final mixed powders were cold-pressed into cylindrical tablets under a uniaxial pressure of 100 MPa, and then sintered at 1500ºC for 4 hours in air with a heating and cooling rate of 3°C/min. Pure YSZ and Al_2O_3 tablets were also obtained using the same cold press and sintering procedures.

Theoretical full density of the YSZ/Al_2O_3 composite was obtained according to the mixing rule ie, $\rho = \nu_{YSZ}\rho_{YSZ} + \nu_{Al_2O_3}\rho_{Al_2O_3}$ (Eq.(3.1)), where ν_{YSZ} and ν_{Al2O3} are the volume fractions of YSZ and Al_2O_3, and ρ_{YSZ} and ρ_{Al2O3} are the theoretical densities of pure YSZ and Al_2O_3, which are 5.96 and 3.98 g/cm^3, respectively. The density of a sintered specimen was estimated based on its weight and geometrical dimension, and the relative densities were found to be over 95 %. Therefore, the porosity effect has been neglected in this study.

Phase compositions of the YSZ/Al_2O_3 composite were identified by X-ray diffraction (XRD, Philips X'Pert) method using Cu K_α radiation. The measurements were performed on the sample surfaces with a step scanning mode (step size of 0.05°) at a

rage of 0.1° min^{-1}. Microstructure of the YSZ/Al_2O_3 composite was examined using a scanning electron microscope (SEM, Philips XL30).

Electrical properties of the YSZ/Al_2O_3 composites were determined with AC impedance spectroscopy measurements using a Solatron SI 1255 HF frequency response analyser coupled with a Solatron 1296 Dielectric Interface (Solartron, UK). Silver paint was coated on two polished surfaces of a tablet and fired at 350ºC for 1 hour to serve as electrodes. During impedance measurements, an AC voltage of 0.1 V was applied to the sample over a frequency range from 0.1 to 10^7 Hz at various temperatures. Equivalent circuit fittings of the measured impedance spectra were carried out using Zview Impedance Analysis software (Scribner Associates, Inc., Southern Pines, NC). For a clear comparison, all the impedance spectra were normalized by a geometric factor $\alpha = \frac{4t}{\pi D^2}$, where t and D denote to sample thickness and diameter, respectively, to eliminate the influence of sample geometry.

Finite element modelling was carried out using the electromagnetic module in the COMSOL 3.3 software [13] coupled with MATLAB. The application of the finite element method in impedance spectra simulation was proposed by Fleig *et al.* and the fundamentals can be found in Ref. [14]. Descriptions of the boundary conditions and calculation procedures can be found in Ref. [14, 15]. Geometric models and physical parameters used for the calculation are described in part 3.3.

3.3 Results and discussion

3.3.1 Phase composition and microstructure

Figure 3.1 illustrates the X-ray diffraction pattern of the YSZ/Al_2O_3 composite, which reveals the composite consists of cubic YSZ and α-Al_2O_3. No obvious peak shift has been observed, which confirms the solid solubility between Al_2O_3 and YSZ is very limited.

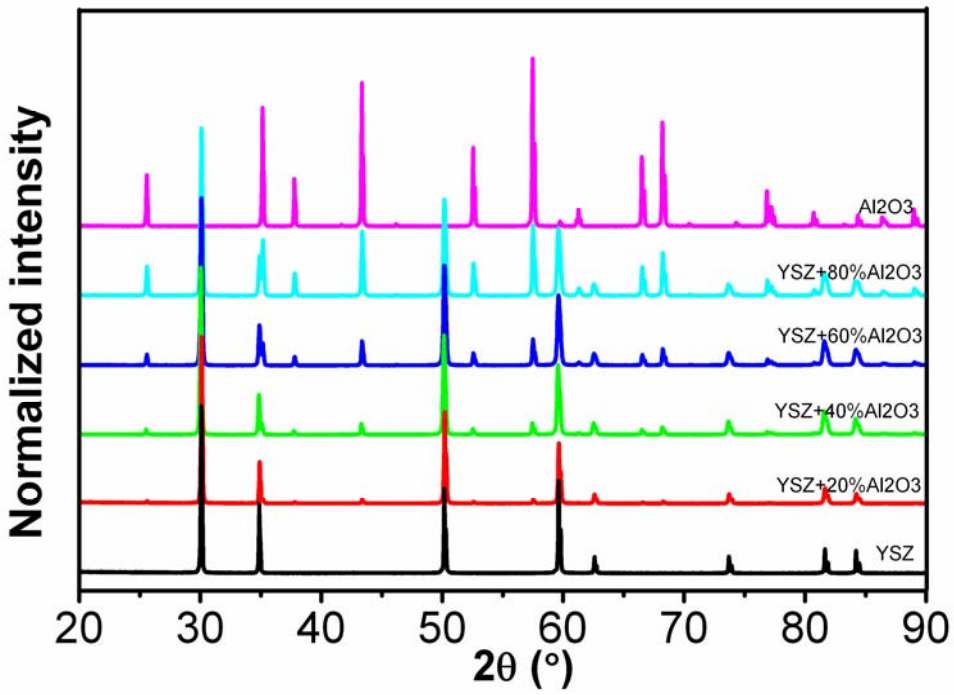

Figure 3.1 X-ray diffraction pattern of the YSZ/Al_2O_3 composite.

The microstructure of the YSZ/Al_2O_3 composite is shown in Figure 3.2. The white phase and the dark phase in the images correspond to YSZ and Al_2O_3 respectively. It can be seen that the minor phase disperses randomly in the major phase without large scale agglomerations. The average grain size of YSZ decreases dramatically with increasing Al_2O_3 volume fraction, from around 10 μm for pure YSZ (not shown) to 0.5 μm in the composite with 80% of Al_2O_3. The change of the component volume fraction and the grain size consequently changes the quantity of the YSZ/Al_2O_3 interface. Although it is rather difficult to quantify those interface fractions, it can be roughly estimated from the images that, the YSZ/Al_2O_3 interface first increases with increasing Al_2O_3 concentration and then decreases with further increasing of Al_2O_3. For example, from the SEM images in Figure 3.2, the composite with 60% Al_2O_3 has more YSZ/Al_2O_3 interface than the other three.

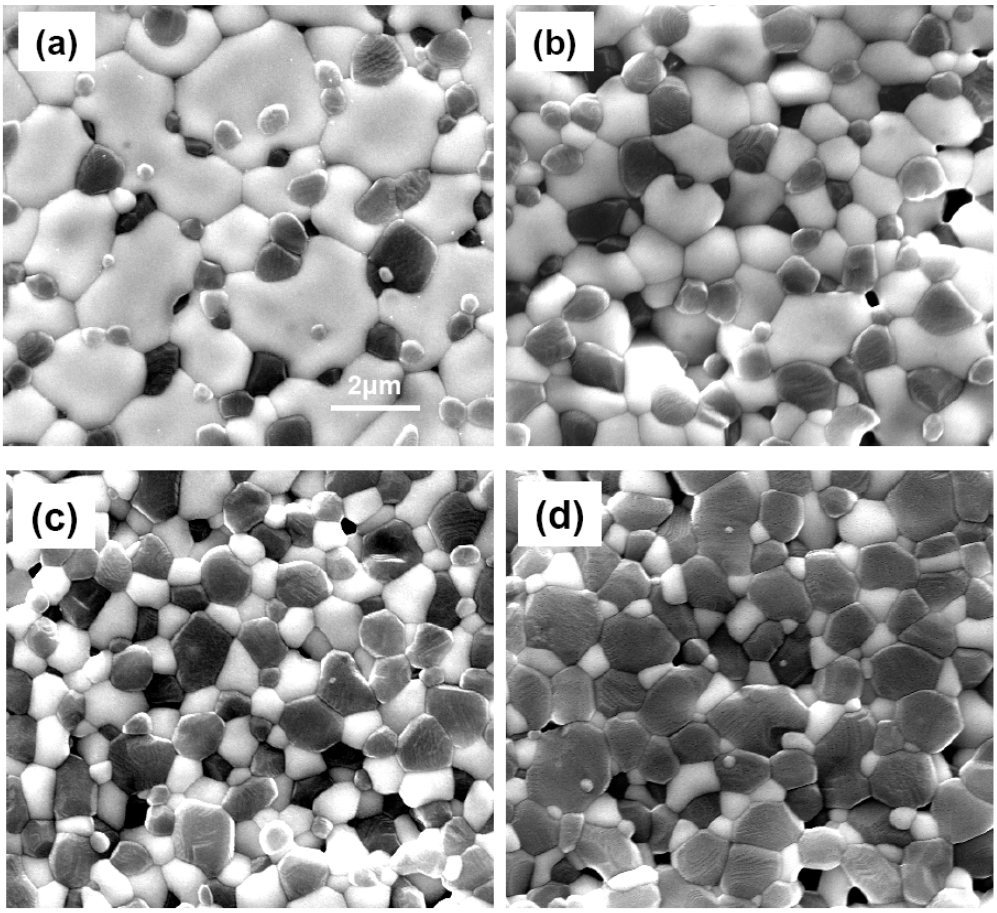

Figure 3.2 Scanning electron micrographs of the YSZ/Al_2O_3 composite with different volume percentage of Al_2O_3. (a) 20% (b) 40% (c) 60% and (d) 80%. The bright area corresponds to YSZ grains and the dark area corresponds to Al_2O_3. The four images have the same scale bar.

3.3.2 Electrical properties

Impedance spectra of the YSZ/ Al_2O_3 composite are shown in Figure 3.3. Figure 3.3(a)-(f) show the impedance spectra of the composite when volume percentage of Al_2O_3 varies from 0 to 85%, measured at 350°C. The Nyquist plot of pure YSZ in Figure 3.3(a), which is typical for YSZ, shows two well resolved semicircles, from left to right (high frequency to low frequency), representing the response from grain and grain boundary, respectively. The Nyquist plots of the YSZ/Al_2O_3 composites have similar features with that of pure YSZ: two semicircles are displayed in their Nyquist plots, as can be seen in Figure 3.3(b)-(f), indicating the existence of Al_2O_3 does not add new features (e.g., one or more semicircles) to their impedance spectra. However, the shape

of the impedance curve changes with the increase of Al_2O_3 volume fraction: the semicircle at low frequency increases much faster than the high frequency semicircle, therefore at high Al_2O_3 fraction (e.g., 80 and 85%), the two semicircles become overlapping with each other so that the two semicircles are not well resolved. The impedance spectra in Figure 3.3 (a)-(f) can be fitted by an equivalent circuit of two parallel-aligned resistance-constant phase element (R-CPE) in series connection (see the solid lines). However, in the cases of the composite with 90% Al_2O_3 and pure Al_2O_3, the impedances are too large to be measured at low temperatures. The Nyquist plot measured at 800°C has only one semicircle in each case, as shown in Figure 3.3(g) and (h), and the impedance spectra can be fitted by an equivalent circuit of one parallel-aligned R-CPE.

The total resistance (sum of the high frequency and low frequency resistance) of the YSZ/Al_2O_3 composite at various temperatures was obtained from the equivalent circuit fitting and subsequently converted to conductivity. Figure 4.4 shows the composition and temperature dependence of the conductivity of the composite. It can be seen that conductivity decreases with increase of volume percentage of Al_2O_3. On the other hand, the temperature dependence of the YSZ/Al_2O_3 composite obeys Arrhenius law that good linear relationship can be observed without turning points within the measured temperature range. Activation energy of each sample can be obtained from the slope of Arrhenius plot. When volume fraction of Al_2O_3 varies from 0 to 85%, the activation energy is independent on the volume fraction of Al_2O_3, with a value of around 1.07 eV which is similar to that of pure YSZ. However, with further increase of Al_2O_3, the activation energy increases to 1.54 eV and 1.68 eV for YSZ + 90 % Al_2O_3 and pure Al_2O_3, respectively. The activation energy values indicate that the conduction is mainly dominated by the YSZ phase even with high volume fraction of Al_2O_3 (e.g., 80 %).

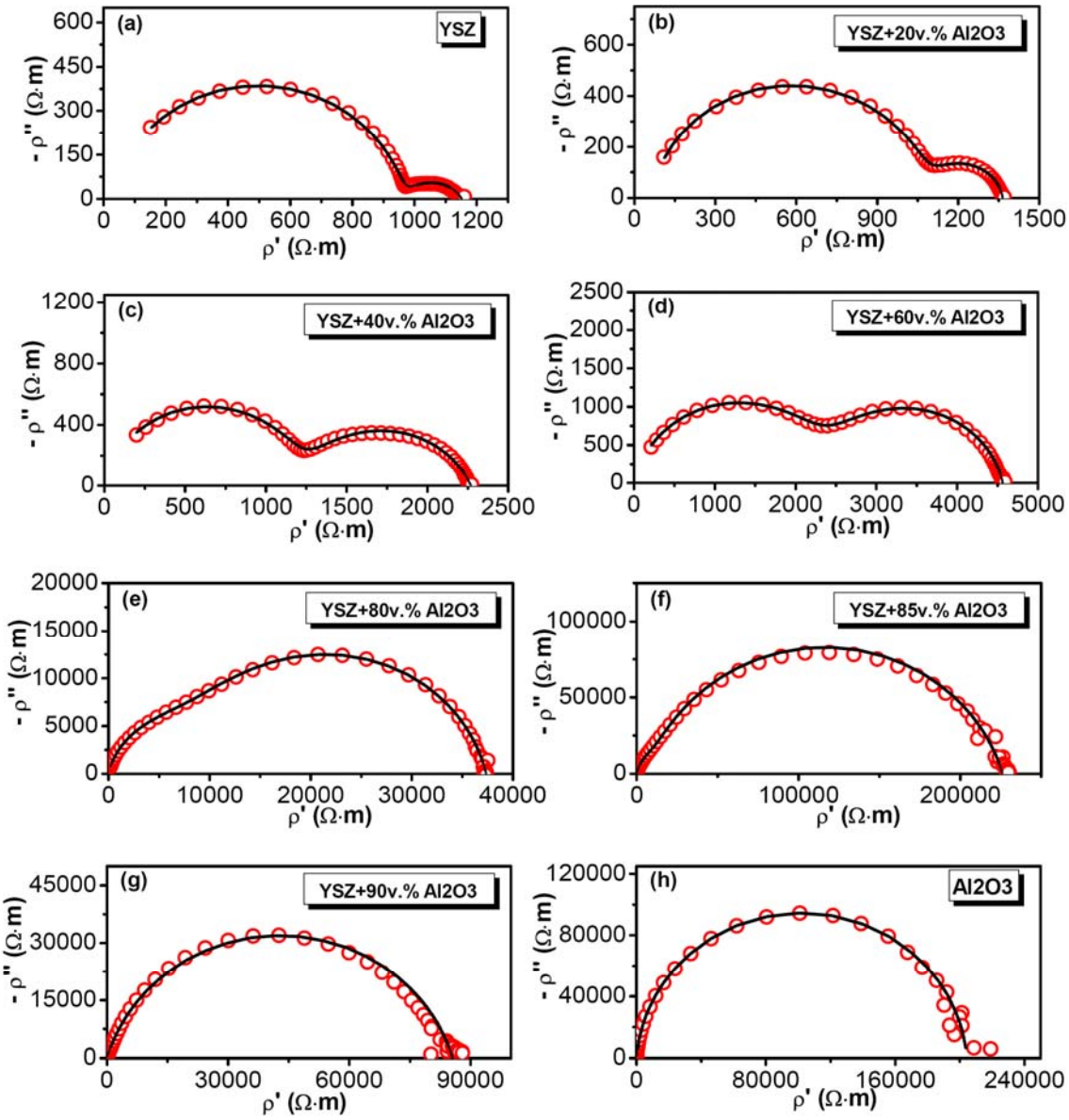

Figure 3.3 Impedance spectra of the YSZ/Al_2O_3 composite. (a)-(f) volume percentage of Al_2O_3 varies from 0 to 85%, measured at 350°C; (g) and (h) YSZ + 90 % Al_2O_3 and pure Al_2O_3, measured at 800°C. The red hollow circles represent measured data, while the black solid lines represent the equivalent circuit fitting results. All the impedance data were normalized by the sample geometry.

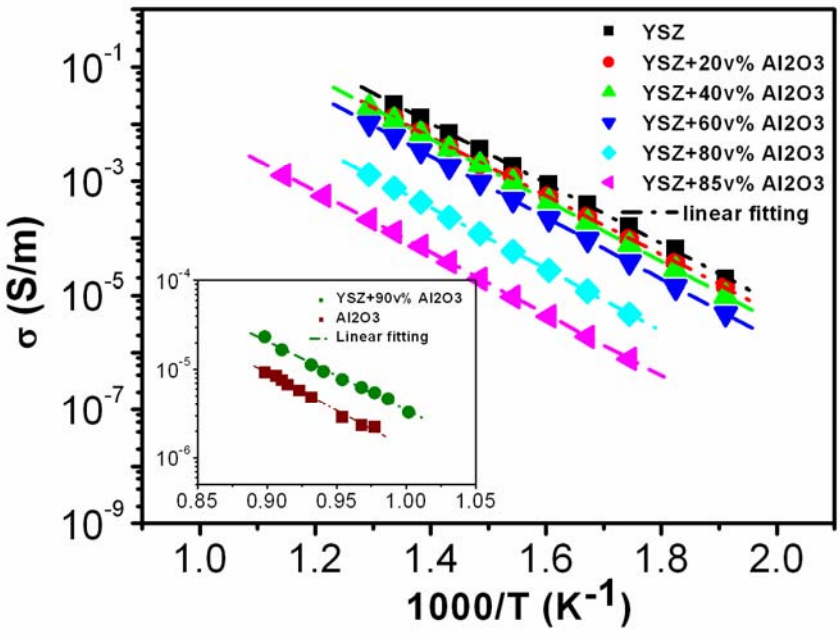

Figure 3.4 Arrhenius plots of YSZ/Al_2O_3 composites. The inset shows the cases of high volume percentage of Al_2O_3 (90%) and pure Al_2O_3 measured at high temperatures. σ corresponds to the total conductivity of the sample, which is calculated by $\sigma = \frac{t}{A}\frac{1}{(R_{HF}+R_{LF})}$, where t and A refer to the thickness and cross-section area of the sample; R_{HF} and R_{LF} represent the resistance of the high and low frequency response respectively.

Figure 3.5 shows the dependency of conductivity of YSZ/Al_2O_3 composites on the volume fraction of YSZ at 350°C. The conductivity of the composites increases with increase in the YSZ volume fraction and exhibits a typical insulator-conductor transition with an increase of more than five orders of magnitude when volume fraction of YSZ increases from 10% to 15%. According to the percolation theory, above the percolation threshold, the conductivity follows the power laws [16-18]: $\sigma_{comp} = \sigma_{YSZ}(f_{YSZ} - f_c)^t$ for $f_{YSZ} > f_c$, (Eq.(3.2)), where σ_{comp} is the conductivity of the composite, σ_{YSZ} is the conductivity of the conductive YSZ component; f_{YSZ} is the volume fraction of YSZ and f_c is the critical volume fraction (the percolation threshold); t is the conductivity exponent. Using a least-squares fit, we obtain the percolation threshold of f_c = 13.9 ± 0.4 %. This value is close to, but slightly lower than the theoretical value of 16% expected

in two phase random composite system [3, 19], and it is in agreement with the reported value of 14 ± 0.2 % in similar composite system in Ref. [3].

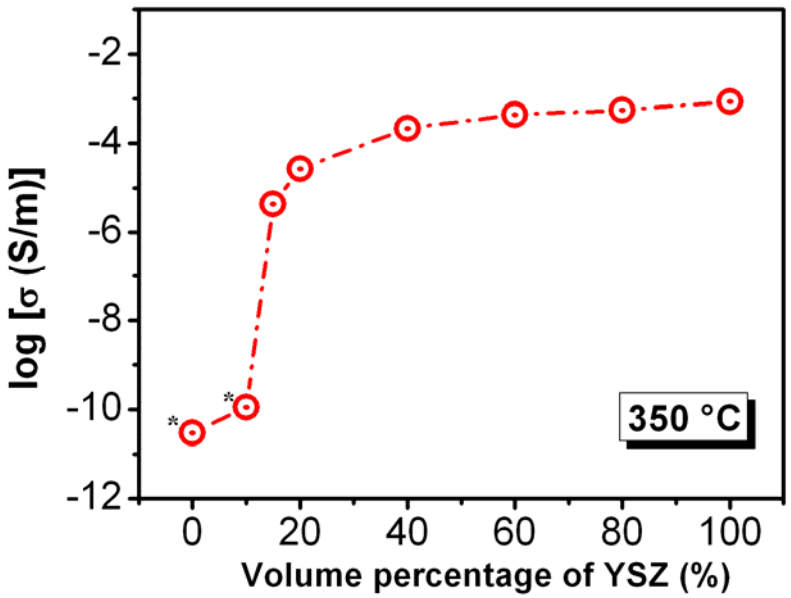

Figure 3.5 Plot of conductivity (350ºC) of the YSZ/Al_2O_3 composite as a function of the volume percentage of YSZ. Symbols with asterisk indicate the values are obtained by extrapolation the Arrhenius plot from high temperature to 350ºC.

3.3.3 Effect of YSZ/Al_2O_3 interface

The Nyquist plot in Figure 3.3 does not show additional features related to the YSZ/Al_2O_3 interface, which makes it difficult to obtain the electrical property of the YSZ/Al_2O_3 interface. However, further analysis of the relaxation frequencies from the Bode plot (imaginary impedance vs frequency) gives some information about the electrical property of the YSZ/Al_2O_3 interface, as discussed in the following parts.

Figure 3.6 shows the Bode plot of the composite with the volume fraction of Al_2O_3 varying from 0 to 85 %, measured at 350ºC. For a clear comparison, the imaginary impedance was scaled by its maximum value. The relaxation frequencies can be obtained by the peak positions, and are listed in Table 3.1. It should be pointed out that when the volume fraction of Al_2O_3 exceeds 80%, the high frequency (HF) response overlaps with the low frequency (LF) response, and therefore only the LF relaxation

frequency can be obtained from the Bode plot. Fortunately, this does not affect the discussion, since we mainly focused on the LF relaxation frequency change.

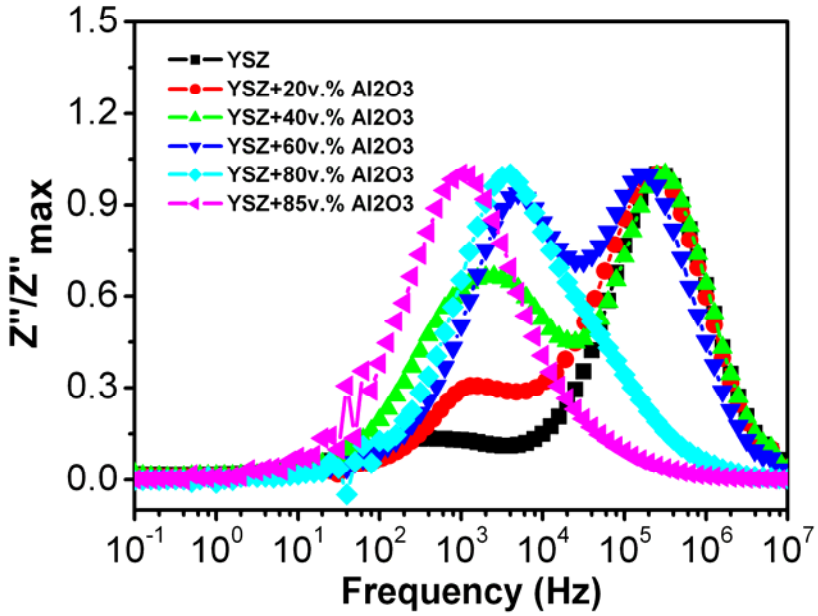

Figure 3.6 Bode plot (imaginary impedance versus frequency) of the YSZ/Al_2O_3 composite when volume fraction of Al_2O_3 varies from 0 to 85%, measured at 350ºC. The imaginary impedance was scaled by its maximum value.

Table 3.1 Relaxation frequencies of the YSZ/Al_2O_3 composite when volume fraction of Al_2O_3 varies from 0 to 85%, measured at 350ºC. LF and HF stand for low frequency and high frequency respectively.

	Relaxation frequency (Hz)	
	LF	HF
YSZ	3.98×10^2	2.51×10^5
YSZ+20% Al_2O_3	6.31×10^2	2.51×10^5
YSZ+40% Al_2O_3	2.51×10^3	2.51×10^5
YSZ+60% Al_2O_3	5.01×10^3	1.58×10^5
YSZ+80% Al_2O_3	3.98×10^3	--
YSZ+85% Al_2O_3	1.00×10^3	--

The relaxation frequency (f) of a material is determined by its conductivity and dielectric constant by the following relationship:

$$2\pi f = \frac{1}{RC} = \frac{1}{(\frac{1}{\sigma}\frac{t}{A})\cdot(\varepsilon_0\varepsilon_r\frac{A}{t})} = \frac{\sigma}{\varepsilon_0\varepsilon_r}, \quad (3.3)$$

where R and C represent the resistance and capacitance; t and A denote sample thickness and cross section area; σ, ε_0 and ε_r have their commonly used meanings. In Table 1, the LF relaxation frequency shows obvious change with Al_2O_3 volume fraction, indicating an obvious change of either conductivity or dielectric constant. Since the dielectric constant of YSZ-based ceramic materials does not differ significantly, it is considered the shift of relaxation frequency is mainly caused by the conductivity change.

Compared with pure YSZ, the composite samples have higher LF relaxation frequencies, as listed in Table 3.1. With increase of Al_2O_3 volume fraction, the LF relaxation frequency shifts to higher frequency, reaching its highest value when Al_2O_3 volume fraction is 60%, and decreases afterward. This trend is generally in agreement with the change of YSZ/Al_2O_3 interface fraction in the composite. Therefore, the YSZ/Al_2O_3 interface might be a possible reason for the LF relaxation frequency change.

In order to testify the validity of the above statement, the conductivities (at 350ºC) of the two responses were calculated separately and they were plotted as a function of the volume fraction of Al_2O_3, as shown in Figure 3.7. The HF conductivity was calculated by $\sigma_{HF} = \frac{t}{A}\frac{1}{R_{HF}}$, and it shows an obvious decrease with an increase of Al_2O_3 volume fraction. The decrease of HF conductivity is considered to be caused by the reduction of the conductive YSZ volume fraction, which is confirmed by the little change of normalized conductivity (conductivity divides YSZ volume fraction) with increasing Al_2O_3 volume fraction (see the open triangles). On the other hand, the LF conductivity (calculated by $\sigma_{LF}^{sp} = \frac{t}{A}\frac{1}{R_{LF}}\frac{C_{HF}}{C_{LF}}$ [10]) shows an obvious up-going trend when Al_2O_3 volume fraction varies from 0 to 60%, while it goes downward with further addition of Al_2O_3. This trend is in agreement with the LF relaxation frequency change, proving the

validity of Eq.(3.3) and confirming the claim that the change of LF relaxation frequency is mainly caused by the conductivity change.

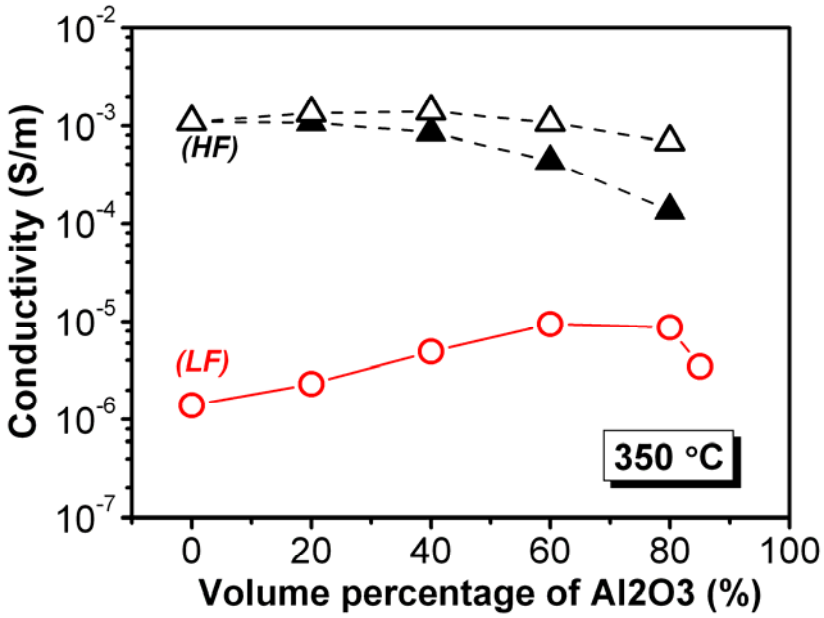

Figure 3.7 High-frequency (HF) and low-frequency (LF) conductivities of the YSZ/Al_2O_3 composites as a function of Al_2O_3 volume fraction. The black solid triangles represent the HF conductivity calculated by $\sigma_{HF} = \frac{t}{A}\frac{1}{R_{HF}}$; the black open triangles represent the HF conductivity normalized by the volume fraction of YSZ (σ_{HF}/ν_{YSZ}); the LF conductivity was calculated according to $\sigma_{LF}^{sp} = \frac{t}{A}\frac{1}{R_{LF}}\frac{C_{HF}}{C_{LF}}$.

From Table 3.1 it can be seen that, with increase of Al_2O_3 volume fraction, the LF relaxation frequency shifts to higher frequency, reaching its highest value when Al_2O_3 volume fraction is 60%, and decreases afterward (The LF conductivity in Figure 3.7 shows the same trend). This trend is generally in agreement with the change of YSZ/Al_2O_3 interface fraction in the composite. Therefore, the YSZ/Al_2O_3 interface might be a possible reason for the LF relaxation frequency change.

However, before we can attribute the LF relaxation frequency shift to the YSZ/Al_2O_3 interface, other factors that may influence the LF relaxation frequency should be excluded. First, the existence of the Al_2O_3 phase might influence the relaxation

frequency and its effect is discussed as follows. Because of the electrical insulative property of Al_2O_3, its effect on the impedance spectroscopy is analogous to the porosity effect, which has already been well established. The early work of Brailsford and Hohnke [20] demonstrated that the presence of pores does not introduce a new arc or other feature in the impedance spectra, but it alters the diameters of the grain or grain boundary impedance arc, dependent on the pore location (intragranular or intergranular), by decreasing the "effective" grain or grain boundary conductivity. The "effective" conductivity decreases monotonically with increasing porosity [21]. Therefore, the existence of Al_2O_3 should decrease either the HF or the LF relaxation frequency. With increasing Al_2O_3 volume fraction, the relaxation frequency should keep shifting to lower frequency range. This is in disagreement with our experimental observations, thus the shift of the LF relaxation frequency is not caused by the existence of Al_2O_3.

Second, as described in part 3.3.1, the grain size of YSZ decreases obviously with increase in the Al_2O_3 volume fraction, thus the influence of grain size should be clarified first. In Ref [10] and [22], Guo *et al.* studied and summarized the grain size dependences of bulk and grain boundary conductivity in YSZ. In the case of 8.2 mol% YSZ, the conductivity of YSZ grain is almost independent on the grain size, while the grain boundary conductivity increases with decrease in grain size [23]. However, the variation of grain boundary conductivity of YSZ over a wide range of grain size, from several nanometers to tens of micrometers, is less than half order of magnitude. In addition, in the references, the samples with different grain sizes were obtained by controlling the sintering temperature. High sintering temperature causes more yttrium element or impurity segregations at the grain boundary, leading to more oxygen vacancy depletion in the grain boundary space charge region, and consequently decreases the grain boundary conductivity. But in our case, all the samples were sintered at the same temperature and heat treated for the same period. YSZ grain size decreases because the presence of Al_2O_3 inhibits the grain growth. Therefore, it is reasonable to believe that the grain boundary conductivity change caused by grain size difference is minor in our composite system.

The third possible reason for the shift of LF relaxation frequency is that the existence of Al_2O_3 changes the YSZ grain boundary conductivity. Feighery and Irvine [2] studied

the Al_2O_3 content dependence of the grain boundary conductivity of 8 mol.% YSZ. They found the grain boundary conductivity increases by 1.5 orders of magnitude when the Al_2O_3 content increases from 0 to 1 wt%, but it then decreases gradually with further increasing Al_2O_3 addition. For the composite with 13 wt.% Al_2O_3, the grain boundary conductivity is around one order of magnitude higher than of the pure YSZ. Similar phenomenon is also reported in Ref. [8] and [24]. Therefore, the grain boundary conductivity for the composite is higher than that for the pure YSZ, but it decreases with increasing Al_2O_3 content. If the LF relaxation frequency change is caused by the grain boundary conductivity change, it is expected the LF relaxation frequency shifts to lower frequency range when the volume fraction of Al_2O_3 increases from 20% to 60%, which is against the results in Table 3.1.

Excluding the above three factors, we assume the presence of the YSZ/Al_2O_3 interface as the possible reason for the LF relaxation frequency shift. And according to Eq.(3.3), a shift toward higher frequency range indicates an increasing conductivity, thus it can be deduced that the YSZ/Al_2O_3 interface is more conductive than the YSZ grain boundary. However, there is still a question to be answered before we draw any conclusion: does the YSZ/Al_2O_3 interface really contribute to the LF relaxation frequency? In order to answer this question and investigate the interface effect, a 2-dimensional finite element modelling was employed to simulate the impedance spectra of the composite. The geometric models were established based on the microstructure of YSZ, as illustrated in Figure 3.8. In the modelling, the following simplifications were employed. First, in the real case, the thickness of grain boundary is around several nanometers, which is far smaller than the grain size. However, for finite element calculation, too thin grain boundary will lead to difficulties in meshing and extensively increase the computation work. Therefore the YSZ grain boundary and the YSZ/Al_2O_3 interface are treated as thin layers with certain thickness comparable to grain size. On the other hand, we ignore the effect of Al_2O_3 grain boundary due to the insulative property of Al_2O_3. Isolated Al_2O_3 grains randomly substitute the position of YSZ grains, as shown in Figure 3.8(c).

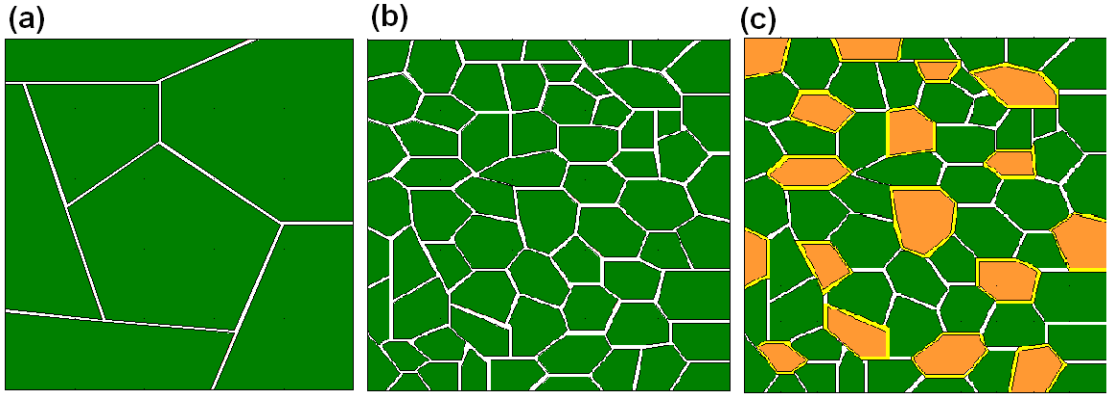

Figure 3.8 Geometric models for finite element modelling. Green, white, orange and yellow colours represent YSZ grain, YSZ grain boundary, Al_2O_3 and YSZ/Al_2O_3 interface, respectively. The side length of the model is 1, and the grain boundary thickness is 0.01 (arbitrary unit).

In the calculation, the conductivity of YSZ grain was fixed at 1.0×10^{-3} S/m (close to the value at 350 ºC); for the YSZ grain boundary, values of 1.0×10^{-5} and 5.0×10^{-6} S/m were chosen based on the fact that the YSZ grain boundary conductivity is usually two or three orders of magnitude lower than the YSZ grain conductivity [10]; the conductivity of Al_2O_3 was seven orders of magnitude lower than that of the YSZ bulk, which was estimated from Figure 3.5 as well as Ref. [25]. Dielectric constants of YSZ and Al_2O_3 were obtained from Ref. [26] and [27]. Dielectric constant of YSZ grain boundary is the same as its bulk value since the dielectric constant of ZrO_2 is insensitive to its composition [28]. The conductivity of the YSZ/Al_2O_3 interface varies from 10^{-2} to 10^{-6} S/m, and its dielectric constant is assumed to be the same as either YSZ or Al_2O_3. The above physical parameters were listed in Table 3.2.

The calculated relaxation frequencies of the above models were also listed in Table 3.2. Model (a) and (b) illustrate the effect of grain size in pure YSZ. The results confirm that the LF relaxation frequency is only determined by the physical parameters (conductivity) of grain boundary. In model (b), when the grain boundary conductivity increases, the LF relaxation frequency shifts to higher frequency range, as predicted by Eq.(3.3).

Model (c) simulates the microstructure of the YSZ/Al_2O_3 composite, where YSZ is the major phase. Compared with pure YSZ (model (b)), both the LF and HF relaxation frequency are influenced by the physical parameters of the YSZ/Al_2O_3 interface. The

LF relaxation frequency combines the contributions from YSZ grain boundary and the YSZ/Al_2O_3 interface, and its shift direction is determined by the relative conductivity magnitude of YSZ grain boundary and YSZ/Al_2O_3 interface. When $\sigma_{YSZ/Al2O3}>\sigma_{gb}$, it shifts to higher frequency range; when $\sigma_{YSZ/Al2O3}<\sigma_{gb}$, it shifts to lower frequency range. For the HF relaxation frequency, it moves to higher frequency range only in the case when $\sigma_{YSZ/Al2O3}>\sigma_{g}$. In the remaining cases, the HF relaxation frequency remains constant, and shifts to lower frequency range compared with pure YSZ. The modelling results confirm that the YSZ/Al_2O_3 interface has an obvious effect on the LF relaxation frequency of the composite system.

There comes an argument that in the YSZ/Al_2O_3 composites, the oxygen vacancies are blocked by the insulative Al_2O_3 phase and therefore they move within the YSZ phase under the electric field. Therefore the YSZ/Al_2O_3 interfaces seem to be "parallel" to the motion of the oxygen vacancies. Usually it is accepted that the parallel boundaries affect the first semicircle and not the second one [29]. However, in this study, both the experimental evidences and the modelling results indicate the YSZ/Al_2O_3 interface contributes to the LF response (second semicircle) on the impedance spectroscopy. This is possibly due to the fact that, the YSZ/Al_2O_3 interface is not continuously connected inside the composite, especially when the volume fraction of Al_2O_3 is low. Therefore, although the charge carriers (oxygen vacancies) move along the YSZ/Al_2O_3 interface, they have to move towards the adjacent YSZ grain for further transportation under the electric field. When the charge carriers move from the YSZ/Al_2O_3 interface to the YSZ grain, they actually move across the interface (or the space charge region), as illustrated in Figure 3.9. Therefore, the YSZ/Al_2O_3 interface is still "perpendicular" to the electric field and consequently contributes to the second semicircle on the Nyquist plot.

Table 3.2 Finite element calculation results of the relaxation frequencies, showing the effect of YSZ grain size and YSZ/Al_2O_3 interface. The units for conductivity and relaxation frequency are S/m and Hz, respectively.

Model	YSZ				Al_2O_3		YSZ/Al_2O_3 interface		Relaxation frequency	
	σ_g	ε_g	σ_{gb}	ε_{gb}	σ	ε	σ	ε	LF	HF
(a)	1.0×10^{-3}	28	5.0×10^{-6}	28	--	--	--	--	3.62×10^{3}	6.51×10^{5}
(b)	1.0×10^{-3}	28	5.0×10^{-6}	28	--	--	--	--	3.62×10^{3}	6.51×10^{5}
(b)	1.0×10^{-3}	28	1.0×10^{-5}	28	--	--	--	--	6.26×10^{3}	6.51×10^{5}
(c)	1.0×10^{-3}	28	1.0×10^{-5}	28	1.0×10^{-10}	10	1.0×10^{-2}	28	1.42×10^{4}	8.55×10^{5}
(c)	1.0×10^{-3}	28	1.0×10^{-5}	28	1.0×10^{-10}	10	1.0×10^{-3}	28	1.08×10^{4}	4.95×10^{5}
(c)	1.0×10^{-3}	28	1.0×10^{-5}	28	1.0×10^{-10}	10	1.0×10^{-3}	10	1.08×10^{4}	4.95×10^{5}
(c)	1.0×10^{-3}	28	1.0×10^{-5}	28	1.0×10^{-10}	10	1.0×10^{-4}	28	8.23×10^{3}	4.95×10^{5}
(c)	1.0×10^{-3}	28	1.0×10^{-5}	28	1.0×10^{-10}	10	1.0×10^{-4}	10	8.23×10^{3}	4.95×10^{5}
(c)	1.0×10^{-3}	28	1.0×10^{-5}	28	1.0×10^{-10}	10	1.0×10^{-5}	28	6.26×10^{3}	4.95×10^{5}
(c)	1.0×10^{-3}	28	1.0×10^{-5}	28	1.0×10^{-10}	10	1.0×10^{-6}	28	4.76×10^{3}	4.95×10^{5}

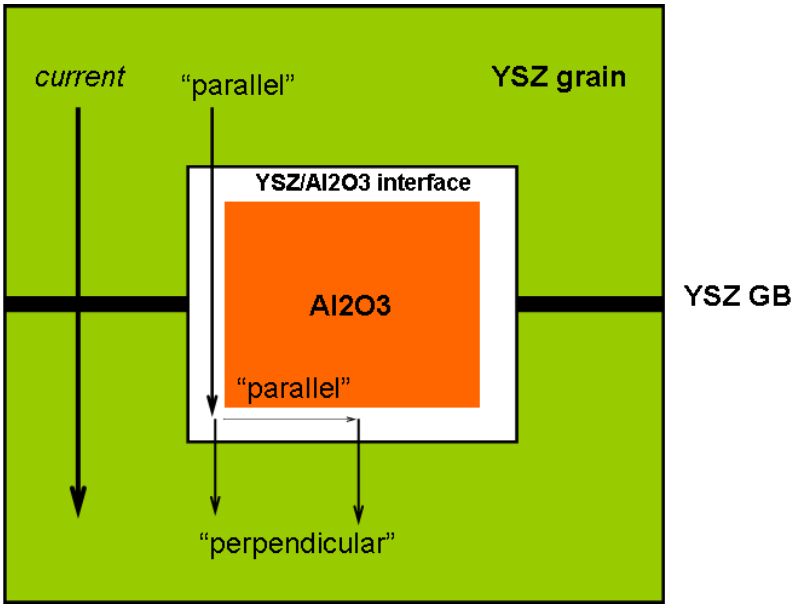

Figure 3.9 Schematic of the current flow in the YSZ/Al_2O_3 interface. The arrows indicate the current direction.

Combining the above modelling results with the experimental results, the following information can be obtained. (1) Both the YSZ grain boundary and the YSZ/Al_2O_3 interface contribute to the LF relaxation frequency. (2) The YSZ/Al_2O_3 interface can not be more conductive than the YSZ grain. Otherwise the HF relaxation frequency will shift to higher frequency range, which is in disagreement with the experimental observations. (3) The YSZ/Al_2O_3 interface should be more conductive than the YSZ grain boundary. The YSZ grain boundary and the YSZ/Al_2O_3 interface contribute to an effective conductivity of the LF response. Because the electrical conduction tends to transport through the "easy path", the effective conductivity is determined by the fraction of the relatively conductive YSZ/Al_2O_3 interface. When the Al_2O_3 volume fraction increases from 20 to 60%, the number of YSZ/Al_2O_3 interface increases and therefore the effective conductivity increases, which causes the LF relaxation frequency moving to higher frequency range. With further increasing Al_2O_3 fraction to 85%, the number of YSZ/Al_2O_3 interface decreases and therefore causes a decreasing of the LF relaxation frequency. From the above analysis, it can be concluded that, the YSZ/Al_2O_3 interface conductivity is higher than the YSZ grain boundary, but lower than or similar to the YSZ grain.

Possible reasons for the relatively conductive YSZ/Al_2O_3 interface are proposed as following. (1) Less siliceous phase exists in the YSZ/Al_2O_3 interface because of the "scavenging" effect of Al_2O_3; (2) Less yttrium element segregates at the YSZ/Al_2O_3 interface, which releases the depletion of oxygen vacancies at the heterogeneous boundary; (3) As proposed by Kumar *et al.*, Al_2O_3 removes the electron concentration gradient which impedes the transport of the oxygen ions [11, 12]; (4) The lattice strain due to the lattice mismatch between the two materials might be reason for the enhanced conductivity at the interface, as reported in some YSZ/oxide multilayered thin films in Ref. [30, 31]. Further work will be carried out to clarify these points.

3.4 Conclusions

Electrical properties of YSZ/Al_2O_3 composite and the YSZ/Al_2O_3 interface were studied by impedance spectroscopy coupled with finite element modelling. The conductivity of the composite shows the typical characteristics expected from the percolation theory, with a critical YSZ volume fraction of 13.9 ± 0.4 % for the onset of conduction. Above this YSZ volume fraction, the activation energy has a similar value with pure YSZ and it is independent of the Al_2O_3 fraction because the electrical (ionic) conduction is mainly dominated by the YSZ phase. The YSZ/Al_2O_3 interface is discussed from the relaxation frequency analysis and finite element modelling. It is found the low frequency response combines the contribution from both the YSZ grain boundary and the YSZ/Al_2O_3 interface and the conductivity of the YSZ/Al_2O_3 interface is higher than YSZ grain boundary but similar to, or lower than the YSZ grain. Although the presence of Al_2O_3 leads to a blocking effect which suppresses the composite conductivity because of its intrinsic electrical insulation, the conductive YSZ/Al_2O_3 interface provides a possible way to enhance the ionic conductivity of YSZ/Al_2O_3 composite, which is beneficial to its application in SOFC.

References

[1] M. Mori, T. Abe, H. Itoh, O. Yamamoto, Y. Takeda and T. Kawahara, *Cubic-stabilized zirconia and alumina composites as electrolyte in planar type solid oxide fuel cells*, Solid State Ionics **74** (1994) 157-164.

[2] A. J. Feighery and J. T. S. Irvine, *Effect of alumina additions upon electrical properties of 8 mol.% yttria-stabilised zirconia*, Solid State Ionics **121** (1999) 209-216.

[3] J. M' Peko, D. Spavieri Jr., C.da Silva, C. Fortulan, D. de Souza and M. de Souza, *Electrical properties of zirconia-alumina composites*, Solid State Ionics **156** (2003) 59-69.

[4] A. Rizea, D. Chirlesan, C. Petot and G. Petot-Ervas, *The influence of alumina on the microstructure and grain boundary conductivity of yttria-doped zirconia*, Solid State Ionics **146** (2002) 341-353.

[5] X. Guo, *Space-charge conduction in yttria and alumina codoped-zirconia*, Solid State Ionics **96** (1997) 247-254.

[6] Y. Ji, J. Liu, Z. Lv, X. Zhao, T. He and W. Su, *Study on the properties of Al_2O_3-doped $(ZrO_2)_{0.92}(Y_2O_3)_{0.08}$ electrolyte*, Solid State Ionics **126** (1999) 277-283.

[7] X. Guo, W. Sigle, J. Fleig and J. Maier, *Role of space charge in the grain boundary blocking effect in doped zirconia*, Solid State Ionics **154-155** (2002) 555-561.

[8] A. Yuzaki and A. Kishimoto, *Effects of alumina dispersion on ionic conduction of toughened zirconia base composite*, Solid State Ionics **116** (1999) 47-51.

[9] X. Guo, *Roles of alumina in zirconia for functional applications*, Journal of the American Ceramic Society **86** (2003) 1867-1873.

[10] X. Guo and R. Waser, *Electrical properties of the grain boundaries of oxygen ion conductors: acceptor-doped zirconia and ceria*, Progress in Materials Science **51** (2006) 151-210.

[11] B. Kumar, C. Chen, C. Varanasi and J. Fellner, *Electrical properties of heterogeneously doped yttria stabilized zirconia*, Journal of Power Sources **140** (2005) 12-20.

[12] B. Kumar and J. Thokchom, *Space charge-mediated ionic transport in yttria-stabilized zirconia-alumina composite membranes*, Journal of the American Ceramic Society **91** (2008) 1175-1181.

[13] COMSOL Ltd., COMSOL Multiphysics, London

[14] J. Fleig and J. Maier, *Finite element calculations of impedance effects at point contacts*, Electrochimica Acta **41** (1996) 1003-1009.

[15] L. Deng, Y. Xiong and P. Xiao, *Modelling and experimental study of impedance spectra of electron beam physical vapour deposition thermal barrier coatings*, Surface and Coating Technology **201** (2007) 7755-7763.

[16] D. J. Begman, *Exactly solvable microscopic geometries and rigorous bounds for the complex dielectric constant of a two-component composite material*, Physics Review Letters **44** (1980) 1285-1287.

[17] C. –W. Nan, *Physics of inhomogeneous inorganic materials*, Progress in Materials Science **37** (1993) 1-116.

[18] Y. Meir, *Percolation-type description of the metal-insulator transition in two dimensions*, Physical Review Letters **83** (1999) 3506-3509.

[19] D. S. McLachlan, M. Blaszkiewicz and R. E. Newnham, *Electrical resistivity of composites*, Journal of the American Ceramic Society **73** (1990) 2187-2203.

[20] A. D. Brailsford and D. K. Hohnke, *The electrical characterization of ceramic oxides*, Solid State Ionics **11** (1983) 133-142.

[21] E. Barsoukov and J. R. Macdonald, *Impedance Spectroscopy Theory, Experiment, and Applications*, Second Edition, John Wiley & Sons, Inc., USA (2005), p.216-218

[22] X. Guo and Z. Zhang, Grain size dependent grain boundary defect structure: case of doped zirconia, Acta Materialia **51** (2003) 2539-2547.

[23] M. J. Verkerk, B. J. Middelhuis and A. J. Burggraaf, *Effect of grain boundaries on the conductivity of high-purity ZrO_2-Y_2O_3 ceramics*, Solid State Ionics **6** (1982) 159-170.

[24] S. Rajendran, J. Drennan and S. P. S. Badwal, Effect of alumina additions on the grain boundary and volume resistivity of tetragonal zirconia polycrystals, Journal of Materials Science Letters **6** (1987) 1431-1434.

[25] O. T. Özkan and A. J. Moulson, *The electrical conductivity of single-crystal and polycrystalline aluminium oxide*, Journal of Physics D: Applied Physics **3** (1970) 983-987.

[26] N. H. Perry, S. Kim and T. O. Manson, *Local electrical and dielectric properties of nanocrystalline yttria-stabilized zirconia*, Journal Materials Science **43** (2008) 4684-4692.

[27] D. R. Lide, CRC Handbook of Chemistry and Physics, CRC Press, LLC (2004), p.12.

[28] X. Guo and J. Maier, *Grain boundary blocking effect in zirconia: A Schottky barrier analysis*, Journal of Electrochemical Society **148** (2001) E121-E126.

[29] S. Kim and J. Maier, Partial electronic and ionic conduction in nanocrystalline ceria: role of space charge, Journal of the European Ceramic Society **24** (2004) 1919-1923.

[30] C. Korte, A. Peters, J. Janek, D. Hesse and N. Zakharov, *Ionic conductivity and activation energy for oxygen ion transport in superlattices- the semicoherent multilayer system YSZ (ZrO_2 + 9.5 mol% Y_2O_3)/Y_2O_3*, Physical Chemistry Chemical Physics **10** (2008) 4623-4635.

[31] A. Peters, C. Korte, D. Hesse, N. Zakharov and J. Janek, *Ionic conductivity and activation energy for oxygen ion transport in superlattices- the multilayer system CSZ (ZrO_2 + CaO)/Al_2O_3*, Solid State Ionics **178** (2007) 67-76.

Chapter 4

Thermal conductivities of YSZ/Al_2O_3 composites

4.1 Introduction

A YSZ/Al_2O_3 composite is of both fundamental and practical interest. Because of the immiscibility of YSZ and Al_2O_3 [1], the YSZ/Al_2O_3 composite is of scientific importance in understanding the physical properties of a diphase system and ceramic/ceramic interfaces [2]. On the practical side, a YSZ/Al_2O_3 composite which combines the properties of the individual components has a wide range of applications. For example, a YSZ/Al_2O_3 composite has been proposed as an electrolyte for a planar Solid Oxide Fuel Cell (SOFC) because of its enhanced mechanical and thermal properties compared with conventional YSZ [3]. A YSZ/Al_2O_3 composite has the potential of being used as a thermal barrier coating (TBC) material because of its enhanced hardness, improved oxidation resistance for the substrate, and longer thermal cycling life than a conventional YSZ coating [4]. Therefore, an investigation of the thermal conductivity, which is an important physical property of a YSZ/Al_2O_3 composite, is necessary.

Another reason for studying the thermal conductivity of a YSZ/Al_2O_3 composite is to obtain the thermal properties of its interfaces. The existence of interfaces usually impedes the heat conduction by scattering the incident phonons and contributes to an

interfacial thermal resistance (also known as the Kapitza resistance), which plays an important role in the thermal transport in nano-scale structures and devices [5]. The interfacial thermal resistance is also proposed as an important factor in selection of TBC candidate materials [6]. The Kapitza resistance of a YSZ/Al_2O_3 interface is also of special interest because during the high temperature service of a TBC, a thermally grown oxide (TGO) layer, which is mainly composed of α-Al_2O_3, forms at the substrate/coating interface [7]. Whether this YSZ/TGO (Al_2O_3) interface has influence on the thermal conductivity and how large this influence is, is an unsolved issue in the thermal conduction of TBCs. Consequently, an estimation of the Kapitza resistance of YSZ/Al_2O_3 interfaces is important.

The interfacial thermal resistance can be estimated by studying the thermal conductivity of the two-phase composite. Usually the effective thermal conductivity of a two-phase composite material without any interfacial thermal resistance can be predicted by the Maxwell theoretical model [8]. With the existence of a Kapitza resistance, the thermal conductivity of the composite will be lower than the value predicted by the Maxwell model. The interfacial thermal resistance can be estimated by the equation proposed by Hasselman and Johnson [9]:

$$k_c = k_m \left[\frac{2\left(\frac{k_d}{k_m} - \frac{k_d}{ah} - 1\right)\nu_d + \left(\frac{k_d}{k_m} + \frac{2k_d}{ah} + 2\right)}{\left(1 - \frac{k_d}{k_m} + \frac{k_d}{ah}\right)\nu_d + \left(\frac{k_d}{k_m} + \frac{2k_d}{ah} + 2\right)} \right], \tag{4.1}$$

where k is the thermal conductivity; the subscripts c, m and d represent the composite, matrix and dispersed phase; a is the particle radius, h is the interfacial thermal conductance (i.e., the reciprocal of the interfacial resistance) and ν_d is the volume fraction of the dispersed phase. When $h = \infty$, this indicates an absence of the interfacial thermal resistance, Eq.(4.1) is an expression of the Maxwell model.

In this chapter, the thermal conductivity of a YSZ/Al_2O_3 composite was studied. The purpose of this study is not only to give an overall picture of the thermal conductivity of the composite, but also to promote an understanding of the Kapitza resistance of the YSZ/Al_2O_3 interfaces. The results may provide useful information for further

application of the composite, as well as for further understanding of the thermal conduction in TBCs.

4.2 Experiments

Procedures for sample preparations, details of XRD and SEM measurements are described in Chapter 3.

Since thermal conductivity is sensitive to porosity of the sample, a precise measurement of the sample density is necessary. Besides the calculated values based on the sample's weight and geometries, the densities of the sintered specimens were also measured by Archimedes' method. The theoretical full densities were calculated according to the rule of mixtures, using theoretical densities of 5.96 g/cm^3 for YSZ [1] and 3.98 g/cm^3 [10] for Al_2O_3. The measured densities, theoretical densities and the relative densities of the YSZ/Al_2O_3 composites are listed in Table 4.1.

Table 4.1 Measured densities, theoretical densities and relative densities of the YSZ/Al_2O_3 composites.

	Measured Density (g/cm^3)	Theoretical Density (g/cm^3)	Relative Density (%)
YSZ	5.86 ± 0.03	5.96	98.3 ± 0.5
YSZ+20%Al_2O_3	5.43 ± 0.03	5.56	97.7 ± 0.4
YSZ+40%Al_2O_3	4.94 ± 0.03	5.17	95.6 ± 0.6
YSZ+60%Al_2O_3	4.55 ± 0.02	4.77	95.4 ± 0.5
YSZ+80%Al_2O_3	4.14 ± 0.02	4.38	94.6 ± 0.5
Al_2O_3	3.83 ± 0.02	3.98	96.5 ± 0.5

The thermal diffusivity measurements were conducted with a laser flash system (Manchester, UK) from 50 ºC up to 900 ºC in an argon atmosphere. The specimens were in the form of disks, 1.5 mm thick and 11 mm in diameter. Before the measurements, the samples were mechanically ground to obtain coplanar surfaces. Both surfaces were coated with a thin layer of carbon using colloidal graphite (Agar Scientific Ltd., UK) to ensure complete and uniform absorption of the laser pulse. The

samples were then dried to remove the remaining solvents. During the measurements, the front face of the samples was subjected to a short-duration heat pulse which was supplied by a neodymium-glass laser of 0.67 ms pulse duration. A liquid nitrogen cooled InSb infra-red detector was used to measure the temperature rise on the backside of the samples. Measurements were made at various chosen temperatures during the heating procedure. For each temperature, ten measurements were made to obtain the mean value of the thermal diffusivity.

The temperature dependence of the specific heat capacities of ZrO_2, Y_2O_3 and Al_2O_3 were obtained from references [11-13]. The specific heat of 8 mol% YSZ was consequently calculated from the values of ZrO_2 and Y_2O_3 according to the Neumann-Kopp rule [14]. The calculated specific heat values for YSZ were compared with the reference values [15] and found to be consistent. The specific heat capacity values of the YSZ/Al_2O_3 composites at various temperatures were calculated from the rule of mixtures. The specific heat values are listed in Table 4.2.

Table 4.2 The specific heat capacities of ZrO_2, Y_2O_3, Al_2O_3, 8 mol% YSZ and the YSZ/Al_2O_3 composites at various temperatures.

Temperature (ºC)	Specific heat capacity ($J.g^{-1}.K^{-1}$)							
	ZrO_2 [11]	Y_2O_3 [12]	YSZ	Al_2O_3 [13]	YSZ/Al_2O_3 composites with Al_2O_3 volume fractions of:			
					20 %	40 %	60 %	80 %
50	0.476	0.465	0.475	0.820	0.524	0.580	0.646	0.725
140	0.523	0.497	0.521	0.959	0.583	0.654	0.738	0.838
250	0.555	0.520	0.552	1.060	0.623	0.706	0.804	0.920
300	0.565	0.528	0.562	1.091	0.636	0.723	0.824	0.945
400	0.581	0.541	0.578	1.136	0.656	0.747	0.854	0.982
500	0.593	0.552	0.590	1.167	0.671	0.765	0.876	1.008
600	0.603	0.562	0.600	1.190	0.683	0.779	0.892	1.027
700	0.612	0.571	0.609	1.209	0.693	0.791	0.906	1.043
800	0.621	0.580	0.617	1.226	0.703	0.802	0.919	1.058
900	0.628	0.588	0.625	1.241	0.712	0.812	0.930	1.071

The microstructure of the YSZ/Al_2O_3 interface was observed by transmission electron microscopy (TEM). The sintered sample was ground to a thickness of approximately 100 μm and ultrasonically cut into discs of 3 mm diameter. The specimen thickness was further reduced to around 30 μm using a dimpling machine (Model D500, VCR Group, San Fransisco, CA). After that, the specimen was cleaned in acetone and mounted onto a molybdenum grid and ion beam thinned using a Gatan (Oxford, UK) precision ion polishing system model 691 (PIPS^{TM}) operating at 4 – 6 kV. TEM observations were carried out using a FEI FEG TEM (Tecnai G2, Eindhoven, the Netherlands) operating at 300 kV.

4.3 Results and discussion

The phase compositions and the microstructures of the YSZ/Al_2O_3 have been described in Chapter 3.

The variations in the thermal diffusivity with temperature for the YSZ/Al_2O_3 composites are shown in Figure 4.1. For all the compositions, the thermal diffusivity decreases monotonically with an increase in the temperature. The thermal conductivities (k) of the YSZ/Al_2O_3 composites were obtained from the heat capacity (C_p), density (ρ) and thermal diffusivity (α) values using the relationship:

$$k = \rho \cdot C_p \cdot \alpha \,. \tag{4.1}$$

The temperature dependence of the thermal conductivity is presented in the open symbols in Figure 4.2. The thermal conductivity of YSZ has a temperature-independent value of around 2.1 W/(m·K), which is in agreement with the reference value for 15 wt% YSZ with a relative density of 98% [15]. For Al_2O_3, an obvious decrease in the thermal conductivity can be observed with an increase in the temperature. The thermal conductivity of Al_2O_3 is close to, but slightly lower than the reported values in the reference [16], which is possibly due to the slightly lower density in the present study. For the YSZ/Al_2O_3 composites, as may be expected, the thermal conductivity increases with an increase in the Al_2O_3 volume fraction because of the intrinsic thermal conductive property of Al_2O_3.

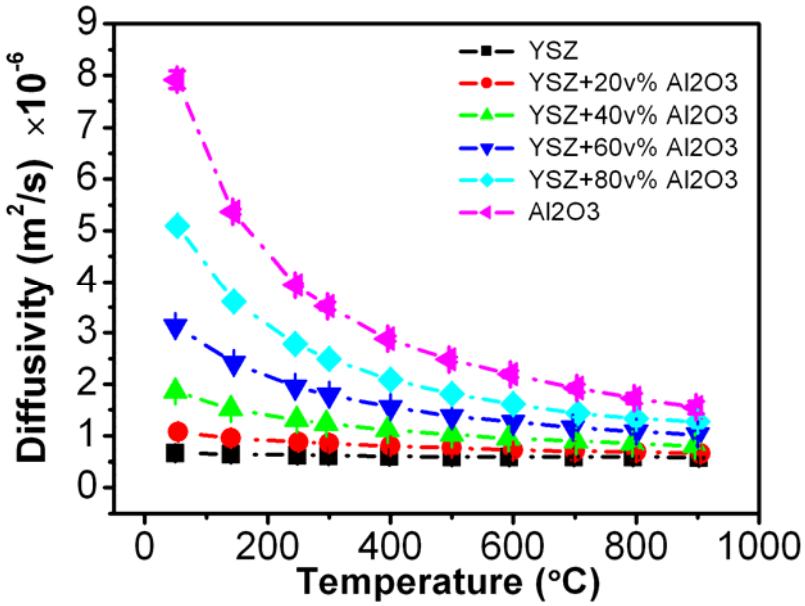

Figure 4.1 Temperature dependence of the thermal diffusivities of the YSZ/Al_2O_3 composites.

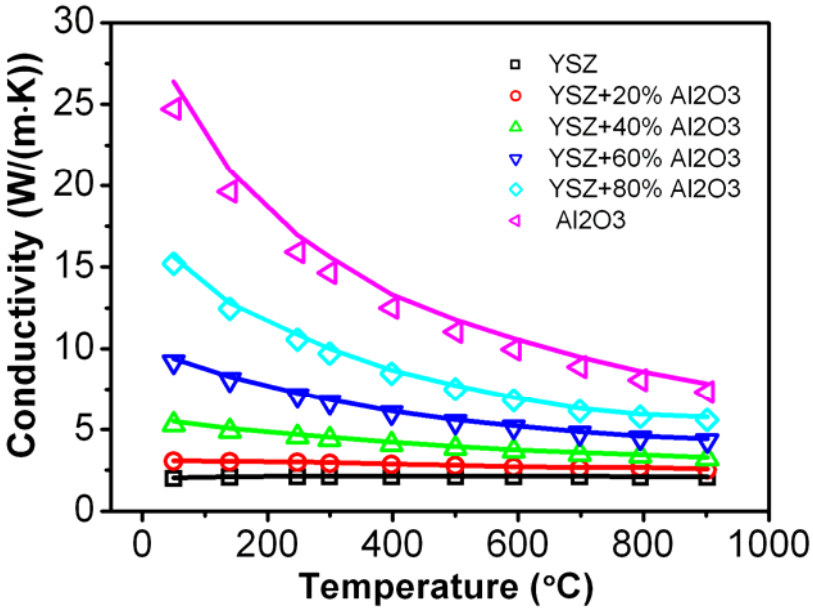

Figure 4.2 Temperature dependence of the thermal conductivities of the YSZ/Al_2O_3 composites. The open symbols represent the measured values of the samples, while the solid lines represent the thermal conductivity of fully-dense samples calculated by Eq.(4.2) and (4.3).

Before going on with further analysis, the effect of porosity on the thermal conductivity of the YSZ/Al_2O_3 composites should be eliminated to obtain the thermal conductivity values of the composites at full density. The YSZ/Al_2O_3 composites with pores can be treated as a "two-inclusion-phase composite" [17], and the thermal conductivity of the fully-dense composite (k_{cf}) can be evaluated with the following relationship [17]:

$$\frac{1}{k_{cp}} = \frac{k_{mf}}{k_{cf}k_{mf}} + \frac{(k_{mf}-k_{mp})(k_{cf}-k_{mf})}{3k_{mf}k_{cf}k_{mp}}, \tag{4.2}$$

where the subscripts *cp*, *cf*, m*p* and *mf* stand for composite with pores, fully dense composite, matrix with pores and fully dense matrix, respectively. The relationship between k_{mf} and k_{mp} is expressed as [17]:

$$k_{mp} = \frac{1-\nu_p}{1+(\eta-1)\nu_p}\cdot k_{mf}, \tag{4.3}$$

where ν_p is the volume fraction of the porosity and η is a parameter which is related to the pore shape. For spherical pores, η equals 1.5. For pure YSZ and Al_2O_3, the thermal conductivity at full density (k_{mf}) was evaluated with Eq.(4.3). When the volume fraction of Al_2O_3 is below 50 %, YSZ is considered to be the matrix and therefore the calculated k_{mf} of YSZ was used in the subsequent calculations for the composite using Eq.(4.2). By contrast, when the volume fraction of Al_2O_3 exceeds 50 %, Al_2O_3 is the matrix and the k_{mf} of Al_2O_3 was used for the subsequent calculations. The calculated thermal conductivities of fully-dense YSZ/Al_2O_3 composites at various temperatures are shown by the solid lines in Figure 4.2. Only a slight increase of the thermal conductivity can be observed after correction.

Figure 4.3 shows the thermal conductivity of the YSZ/Al_2O_3 composites as a function of the volume fraction of Al_2O_3, along with a fitting curve using the Maxwell model. It can be seen that the thermal conductivities predicted by the Maxwell model is in good agreement with the experimental values, which indicates the absence of an obvious interfacial thermal resistance in the YSZ/Al_2O_3 composite system, as discussed in the following paragraphs.

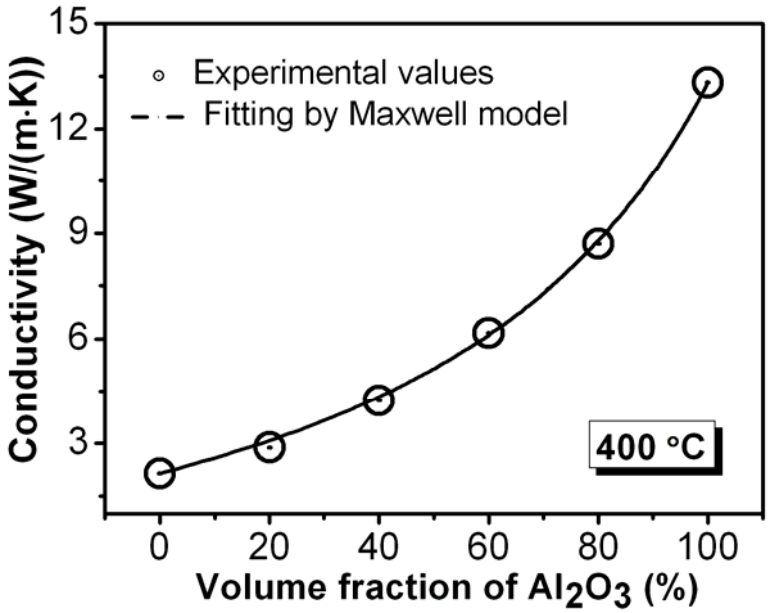

Figure 4.3 Thermal conductivity of the YSZ/Al_2O_3 composites (corrected to zero porosity) as a function of the volume fraction of Al_2O_3 at 400 ºC.

In the YSZ/Al_2O_3 composites, there are three types of interfaces: YSZ/YSZ (YSZ grain boundaries), Al_2O_3/Al_2O_3 (Al_2O_3 grain boundaries) and the YSZ/Al_2O_3 interfaces. The thermal resistance of the YSZ and the Al_2O_3 grain boundaries has been reported in the previous studies, i.e., Yang *et al.* studied the interfacial thermal resistance of nanocrystalline YSZ by measuring the grain-size-dependent thermal conductivity and obtained a value of 4.5×10^{-9} m^2·K/W for YSZ grain boundaries at room temperature [6]; Smith *et al.* investigated the thermal resistance of grain boundaries in Al_2O_3, and evaluated a value of $0.9 \sim 1.3 \times 10^{-8}$ m^2·K/W in dense Al_2O_3 [18]. However, the effect of grain boundaries can be observed only with the existence of a large number of interfaces (a small grain size of tens of nanometres) in YSZ. For example, Raghavan *et al.* found no obvious change of thermal conductivity in 5.8 wt% YSZ when the grain size is larger than 100 nm [15]. For Al_2O_3, the early work by Charvat and Kingery [19] reported almost identical thermal conductivity of dense Al_2O_3 with grain sizes of 9 and 17 μm above 300 ºC, indicating a negligible influence of grain boundaries. In the present study, the average grain size of YSZ changes from ~ 10 μm in the pure YSZ to ~ 0.5 μm in the YSZ/Al_2O_3 composite with 80 v% Al_2O_3, while the average grain size of Al_2O_3 varies from ~ 1 μm in the YSZ/Al_2O_3 composite with 20 v% Al_2O_3 to ~ 5 μm in the pure Al_2O_3. It is known that the phonon mean free path in YSZ has a temperature-

independent value of around 0.2 nm [20], which is much smaller than the YSZ grain size in the composite. The phonon mean free path in Al_2O_3 is about 3 nm at room temperature [19], and it decreases with increasing temperature following a T^{-1} law [20], thus the phonon mean free path can be estimated to be 1.5 nm at 400 ºC, which is more than 500 times smaller than the minimum Al_2O_3 grain size in the composite. Therefore, it can be concluded that neither the YSZ nor the Al_2O_3 grain boundaries have an influence on the thermal conductivity of the composites.

It is usually believed that an interface between two materials with different crystal structures and chemical natures has a larger thermal resistance than a grain boundary in a single-phase material [18]. The interfacial thermal resistance in a composite system can arise from the following aspects. First, the thermal expansion mismatch between the two components can cause imperfect mechanical contact [21,22] or interfacial separation [23]. However, this could not happen in the YSZ/Al_2O_3 composites since the thermal expansion coefficients of YSZ and Al_2O_3 have values close to each other, which are 8×10^{-6} and 10×10^{-6} $ºC^{-1}$, respectively [24]. The YSZ/Al_2O_3 interface is adhesive and coherent without the existence of cracks, as can be seen in the TEM image in Figure 4.4.

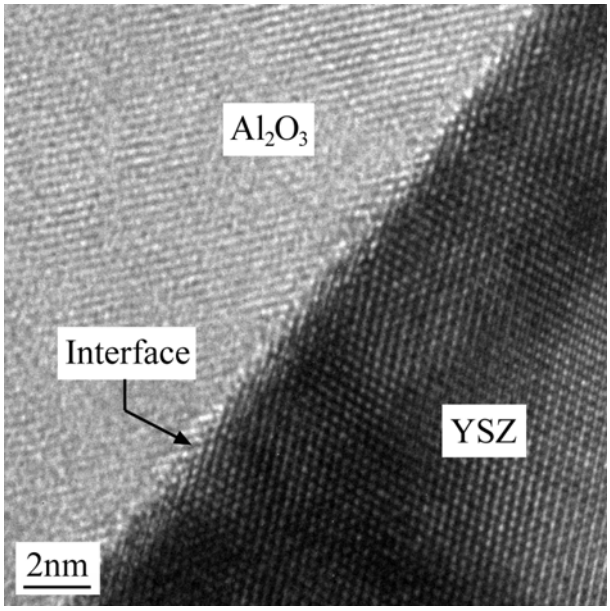

Figure 4.4 High-resolution transmission electron microscopy (HRTEM) image of a YSZ/Al_2O_3 interface. The dark and bright regions represent YSZ and Al_2O_3 grains, respectively.

Second, dislocations and impurity segregations at the interface can act as scattering sites and contribute to the interfacial thermal resistance. However, the YSZ/Al_2O_3 interface is a "clean" interface: only atomic level lattice distortions can be observed without regions of large scale disorder, as also shown in Figure 4.4. Also, impurity segregation is not observed at a YSZ/Al_2O_3 interface because of the "scavenging" effect of Al_2O_3 [25].

Another origin of the Kapitza resistance is the elastic discontinuity at the heterogeneous interface [26]. It is well known that the thermal conductivity of a material is expressed as:

$$k = \frac{1}{3} C v \Lambda , \tag{4.4}$$

where C is the specific heat, v is the phonon velocity and Λ is the phonon mean free path. The phonon velocity is correlated to the elastic property of the material by [27]:

$$v = 0.87\sqrt{\frac{E}{\rho}} , \tag{4.5}$$

where E and ρ are the Young's modulus and the density respectively. When propagating across a heterogeneous interface, the phonons will be scattered to change their velocity, and consequently decrease the transmission probability of the phonons from one side to the other side. According to the diffuse mismatch model (DMM) [28], the phonon transmission probability is determined by the phonon velocity inside the two materials, as expressed by [28]:

$$\alpha = \frac{\sum_j v_{2,j}^{-2}}{\sum_j v_{2,j}^{-2} + \sum_j v_{1,j}^{-2}} , \tag{4.6}$$

where the subscripts "*1*", "*2*" and "*j*" refers to the side with the lower phonon velocity, the side with higher phonon velocity and the phonon mode (longitudinal or transverse) respectively. It can be seen from Eq.(4.6) that, a larger difference between the phonon velocity inside the two materials leads to a lower transmission probability. Since the interfacial thermal resistance is inversely proportional to the phonon transmission probability, it is expected that a large interfacial thermal resistance will exist between the two materials with significantly different Young's moduli. In the YSZ/Al_2O_3 composite system, the difference between the Young's moduli of YSZ and Al_2O_3

($\frac{E_{Al_2O_3}}{\rho_{Al_2O_3}} \cdot \frac{\rho_{YSZ}}{E_{YSZ}} < 3$) is not large enough to have an obvious influence on the phonon transmission probability. Hasselman *et al.* [26] found the interfacial thermal barrier in a cordierite-diamond composite is less than 1.0×10^{-8} $m^2 \cdot K/W$ at 400 ºC, while the Young's modulus of diamond is almost ten times higher than that of cordierite (the density of diamond and cordierite is 3.51 and 2.52 g/cm^3 respectively). Therefore, it is possible that the thermal resistance of the YSZ/Al_2O_3 interface is even smaller than that value.

From the above analysis, it can be concluded that: (1) the negligible thermal resistance effect from the YSZ and Al_2O_3 grain boundaries is caused by the much lower phonon mean free path compared with the grain size in the composite; (2) The low Kapitza resistance is caused by the "clean" and coherent nature of the YSZ/Al_2O_3 interfaces, together with the small difference between the elastic properties of YSZ and Al_2O_3. Therefore, the thermal conductivity of the composite can be predicted well by the Maxwell model because of the absence of any interfacial thermal resistance.

Finally, there is a little remark on the good fitting of the experimental values with the Maxwell model on the YSZ/Al_2O_3 composites, especially when YSZ and Al_2O_3 have comparable volume fractions. Usually, Maxwell model requires dilute dispersions to avoid the interactions between the local temperature fields of neighbouring dispersions [9]. In YSZ/Al_2O_3 composites, the thermal conductivity values of YSZ and Al_2O_3 are not significantly different (for example, k_{Al2O3} is only five times higher than k_{YSZ} at 400 ºC). Therefore, the distortion of temperature gradient around the dispersed phase should be quite mild. In this case, the interaction of the temperature field between two inclusions is very small, as illustrated in the Figure 4.5(a), and consequently extends the application range of Maxwell model. Only when the thermal conductivity values of the two phases are significantly different from each other, the temperature gradient around the dispersed phase is severely distorted (Figure 4.5(b)). In this case the interaction of the temperature field between the two dispersions can not be neglected and the Maxwell model is not usable. On the other hand, because of the small difference between the conductivity of the two phases, the temperature gradient is less dependent on the shape of the dispersed phase, as illustrated in Figure 4.5(c)-(f). Therefore, in the YSZ/Al_2O_3

composites, although the shape of the minor phase is not perfect spherical, the Maxwell model is still applicable.

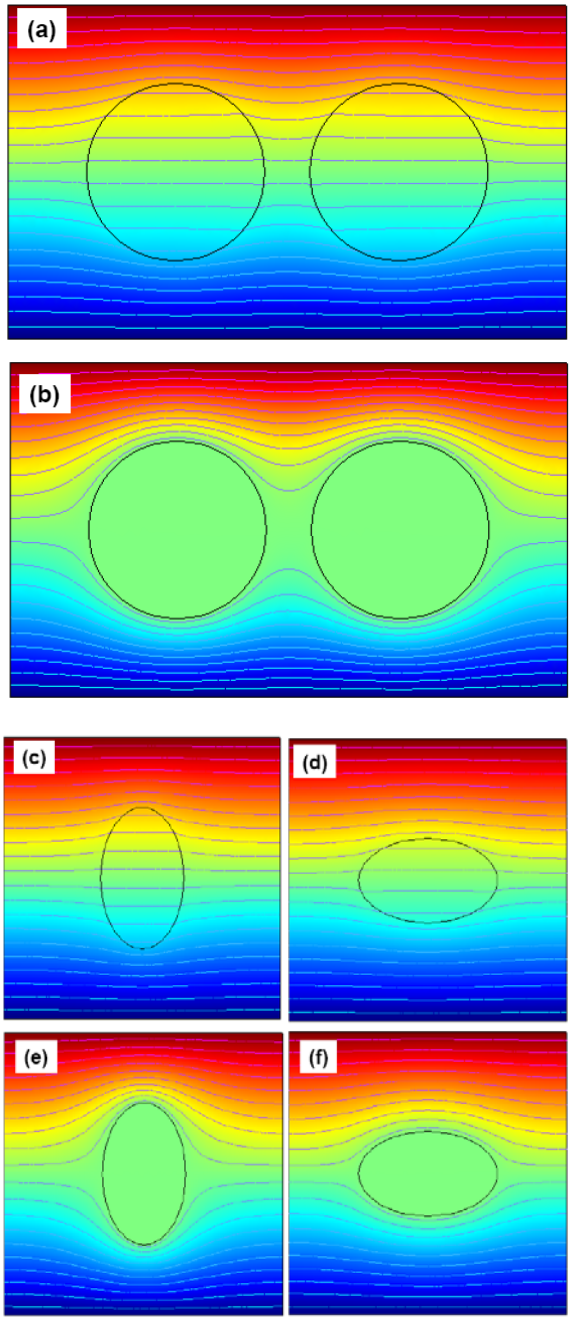

Figure 4.5 Schematics of the temperature profile around dispersions in a diphase material. (a), (c) and (d) are the case when the conductivities of the two phases are comparable, whereas (b), (e) and (f) are the cases when the conductivities of the two phases are significantly different.

4.4 Conclusions

The thermal conductivities/diffusivities of the YSZ/Al_2O_3 composites have been investigated by a laser flash technique from 50 ºC to 900 ºC. The thermal conductivity of the composites increases with an increase in the Al_2O_3 volume fraction, and it can be fitted well by the Maxwell theoretical model. The consistency of the thermal conductivity of the composite with the predicted values indicates the absence of interfacial thermal resistance in the composite. The negligible thermal resistance effect from the YSZ and Al_2O_3 grain boundaries is due to the low phonon mean free path compared with the grain size in the composite. The absence of a Kapitza resistance of the YSZ/Al_2O_3 interface is discussed from the "clean" and coherent nature of the YSZ/Al_2O_3 interface, together with the small difference between the elastic properties of YSZ and Al_2O_3. Although an exact value of the Kapitza resistance of the YSZ/Al_2O_3 interface was not obtained in this study, the results indicate the YSZ/Al_2O_3 interface is not thermally resistive.

References

[1] A. J. Feighery and J. T. S. Irvine, *Effect of alumina additions upon electrical properties of 8 mol.% yttria-stabilized zirconia*, Solid State Ionics **121** (1999) 209-216.

[2] J. C. M' Peko, D. L. Spavieri Jr, C. L. da Silva, C. A. Fortulan, D. P. F. de Souza and M. F. de Souza, *Electrical properties of zirconia-alumina composites*, Solid State Ionics **156** (2003) 59-69.

[3] M. Mori, T. Abe, H. Itoh, O. Yamamoto, Y. Takeda and T. Kawahara, *Cubic-stabilized zirconia and alumina composites as electrolytes in planar type solid oxide fuel cells*, Solid State Ionics **74** (1994) 157-164.

[4] X. Q. Cao, R. Vassen and D. Stoever, *Ceramic materials for thermal barrier coatings*, Journal of the European Ceramic Society **24** (2004) 1-10.

[5] P. Reddy, K. Castelino and A. Majumdar, *Diffuse mismatch model of thermal boundary conductance using exact phonon dispersion*, Applied Physics Letters **87** (2005) 211908.

[6] H. S. Yang, G. R. Bai, L. J. Thompson and J. A. Eastman, *Interfacial thermal resistance in nanocrystalline yttria-stabilized zirconia*, Acta Materialia **50** (2002) 2309-2317.

[7] A. G. Evans, D. R. Mumm, J. W. Hutchinson, G. H. Meier and F. S. Pettit, *Mechanisms controlling the durability of thermal barrier coatings*, Progress in Materials Science **46** (2001) 505-553.

[8] J. C. Maxwell, *A treatise on Electricity and Magnetism*, 3rd Ed., Dover Publications, Inc., New York, 1954, pp.57

[9] D. P. H. Hasselman and L. F. Johnson, *Effective thermal conductivity of composites with interfacial thermal barrier resistance*, Journal of Composite Materials **21** (1987) 508-515.

[10] J. F. Shackelford and W Alexander, *CRC Materials Science and Engineering Handbook*, 3rd Ed., CRC Press LLC, Florida, 2001, pp.81

[11] J. P. Coughlin and E. G. King, *High-temperature heat contents of some zirconium-containing substances*, Journal of the American Chemical Society **72** (1950) 2262-2265.

[12] Y. A. Landa, Y. A. Polonskii, B. S. Glazachev and T. V. Milovidova, *The enthalpy and specific heat of yttrium oxide at 1300-2100 ºK*, Refractories and Industrial Ceramics **15** (1974) 86-88.

[13] R. G. Munro, *Evaluated material properties for a sintered α-alumina*, Journal of the American Ceramic Society **80** (1997) 1919-1928.

[14] H. Kopp, *Investigations of the specific heat of solid bodies*, Philosophical Transcations of the Royal Society of London **155** (1865) 71-202.

[15] S. Raghavan, H. Wang, R. B. Dinwiddie, W. D. Porter and M. J. Mayo, *The effect of grain size, porosity and yttria content on the thermal conductivity of nanocrystalline zirconia*, Scripta Materialia **39** (1998) 1119-1125.

[16] R. Barea, M. Belmonte, M. I. Osendi and P. Miranzo, *Thermal conductivity of Al_2O_3/SiC platelet composites*, Journal of the European Ceramic Society **23** (2003) 1773-1778.

[17] J. Luo, R. Stevens and R. Taylor, *Thermal diffusivity/conductivity of magnesium oxide/silicon carbide composites*, Journal of the American Ceramic Society **80** (1997) 699-704.

[18] D. S. Smith, S. Fayette, S. Grandjean and C. Martin, *Thermal resistance of grain boundaries in alumina ceramics and refractories*, Journal of the American Ceramic Society **86** (2003) 105-111.

[19] F. R. Charvat and W. D. Kingery, *Thermal conductivity: XIII, effect of microstructure on conductivity of single-phase ceramics*, Journal of the American Ceramic Society **40** (1957) 306-315.

[20] R. Mevrel, J. Laizet, A. Azzopardi, B. Leclercq, M. Poulain, O. Lavigne and D. Demange, *Thermal diffusivity and conductivity of $Zr_{1-x}Y_xO_{2-x/2}$ (x = 0, 0.084 and 0.179) single crystals*, Journal of the European Ceramic Society 24 (2004) 3081-3089.

[21] H. Bhatt, K. Y. Donaldson, D. P. H. Hasselman and R. T. Bhatt, *Role of interfacial thermal barrier in the effective thermal diffusivity/conductivity of SiC fiber-reinforced reaction-bonded silicon nitride*, Journal of the American Ceramic Society **73** (1990) 312-316.

[22] H. Bhatt, K. Y. Donaldson, D. P. H. Hasselman and R. T. Bhatt, *Role of interfacial carbon layer in the thermal diffusivity/conductivity of SiC fiber-reinforced reaction-bonded silicon nitride matrix composites*, Journal of the American Ceramic Society **75** (1992) 334-340.

[23] Y. M. Ito, M. Rosenblatt, L. Y. Cheng, F. F. Lange and A. G. Evans, *Cracking in particulate composites due to thermalmechanical stress*, International Journal of Fracture **17** (1981) 1183-1191.

[24] P. Z. Cai, D. J. Green and G. L. Messing, *Constrained densification of alumina/zirconia hybrid laminates, I: experimental observations of processing defects*, Journal of the American Ceramic Society **80** (1997) 1929-1939.

[25] X. Guo and R. Waser, *Electrical properties of the grain boundaries of oxygen ion conductors: acceptor-doped zirconia and ceria*, Progress in Materials Science **52** (2006) 151- 210.

[26] D. P. H. Hasselman, K. Y. Donaldson, J. Liu, L. J. Gauckler and P. D. Ownby, *Thermal conductivity of a particulate-diamond-reinforced cordierite matrix composite*, Journal of the American Ceramic Society **77** (1994) 1757-1760.

[27] D. R. Clarke, *Materials selection guidelines for low thermal conductivity thermal barrier coatings*, Surface and Coating Technology **163-164** (2003) 67-74.

[28] E. T. Swartz and R. O. Pohl, *Thermal boundary resistance*, Reviews of Modern Physics **61** (1989) 605-668.

Chapter 5

Electrical properties of $[(ZrO_2)_{1-x}(CeO_2)_x]_{0.92}(Y_2O_3)_{0.08}$ ($0 \leq x \leq 1$) solid solutions

5.1 Introduction

Oxide ion conductors with cubic fluorite structure are important electrolyte materials for solid oxide fuel cells (SOFCs) [1,2], oxygen sensors [3] and oxygen pumps [4]. High ionic conductivity is achieved in such a structure when the host cations are replaced by lower valence cations, which generates oxygen ion vacancies to compensate the charge missing and to act as charge carriers [5]. The oxygen ions overcome an energy barrier to hop to neighbouring vacant sites and move diffusively to fulfil long-range transport in the material [6].

Among numerous oxide ion conductors, ZrO_2- and CeO_2-based ceramic attract large interest and have been extensively studied [7-15]. They possess many unique physical properties which make them promising materials for practical or potential application in technologically important devices. For example, yttria-stabilized zirconia (YSZ) is the conventionally employed electrolyte material in SOFCs because of its good mechanical, chemical and electrolytic properties [16]. Doped-ceria has higher ionic conductivity, good thermodynamic stability [17] and good catalytic activity [18], therefore it is a prime candidate for the intermediate temperature SOFCs.

The ZrO_2-CeO_2-Y_2O_3 ternary solid solution, which keeps the cubic fluorite structure is also a material of interest both from the practical side and the fundamental side. From the practical side, the idea of a double-layer electrolyte with YSZ on the anode side and doped CeO_2 on the cathode side has been proposed for SOFC [19, 20]. The double-layer electrolyte combines the advantages of YSZ and CeO_2: it suppresses the electronic conduction caused by the reduction of Ce^{4+} at the anode side and retains the high ionic conductivity of doped-CeO_2 [21]. However, the reaction of ZrO_2 and CeO_2 leads to the formation of the ZrO_2-CeO_2-Y_2O_3 ternary solid solution between the two layers. Therefore, an investigation of the ionic conductivity of the ternary solid solution is necessary. On the fundamental side, it is a system to study the homovalent doping effect on the ionic conductivity of the solid solutions if the concentration of Y_2O_3 is constant.

Several studies on the electrical properties of the ZrO_2-CeO_2-Y_2O_3 solid solutions have been reported. However, most of the studies are focused on the mixed conduction of the solid solutions caused by the reduction of Ce^{4+} to Ce^{3+} at various oxygen partial pressures and at high temperatures (> 800 ºC). For example, Cales and Baumard [22] studied the total conductivity of the ternary solid solutions in a large range of oxygen partial pressures from 1000 to 1400 ºC. They discussed the mixed conduction and the defect structure caused by the reduction of Ce^{4+} to Ce^{3+}, and determined the concentrations of the various charge carriers by thermogravimetry and the measurement of the magnetic susceptibility. Arashi *et al*. [23] studied the electrical conduction of the ZrO_2-CeO_2-Y_2O_3 solid solutions at even higher temperatures (> 1200 ºC). They employed the electron blocking method to separate the ionic and electronic conductivities and found that the reduction of Ce^{4+} to Ce^{3+} not only influences the relationship between ionic conductivity and the oxygen partial pressure, but also influences the electronic contribution to the total conductivity. Ananthapadmanabhan *et al*. [24] studied the composition dependence of the electrical conductivity in $[(ZrO_2)_{1-x}(CeO_2)_x]_{0.9}(Y_2O_3)_{0.1}$ solid solutions from ~700 to 1300 ºC in air and they proposed a simple model for the oxygen path length to explain the observed composition dependence of the conductivity.

The reduction of Ce^{4+} at high temperatures makes the ZrO_2-CeO_2-Y_2O_3 solid solution a complicated system to study the effect of tetravalent doping on the ionic conductivity.

On the other hand, most of the current studies on the electrical properties of the ZrO_2-CeO_2-Y_2O_3 solid solutions were studied by DC four-probe measurement. The conductivity obtained from the dc measurement is an overall conductivity from both grain (bulk) and grain boundary. In polycrystalline ceramic materials, the grain boundary has a large influence on the electrical conductivity because of impurity segregations or the space charge effect [25]. For studying the intrinsic property of the ternary solid solution, the contribution of grain boundary to the overall conductivity should be excluded.

Therefore, in this chapter, the electrical properties of the $[(ZrO_2)_{1-x}(CeO_2)_x]_{0.92}(Y_2O_3)_{0.08}$ ($0 \leq x \leq 1$) were studied in an intermediate temperature range (200 - 500 ºC) by impedance spectroscopy. The relative low temperatures were chosen to avoid the reduction of Ce^{4+} and to ensure the electrical conduction in the solid solutions is purely ionic. Impedance spectroscopy was employed to separate the bulk and the grain boundary contributions to the electrical conductivity. The purpose of this work is to study the effect of homovalent doping on the ionic conductivity of the solid solutions.

5.2 Experiments

The samples, formulated as $[(ZrO_2)_{1-x}(CeO_2)_x]_{0.92}(Y_2O_3)_{0.08}$ ($0 \leq x \leq 1$), were synthesized by a solid state reaction method. ZrO_2 (99.6%, PI-KEM, UK), Y_2O_3 (99.99%, PI-KEM, UK) and CeO_2 (99.95%, PI-KEM, UK) powders were used as the starting materials. The powder mixing and drying procedures are the same as those described in Chapter 3. The final mixtures were cold pressed into tablets under a uniaxial pressure of 100 MPa and then sintered at 1500 ºC for 10 hours in air. The other series of solid solutions for comparison, formulated as $[(ZrO_2)_{1-x}(HfO_2)_x]_{0.87}(Y_2O_3)_{0.13}$ ($0 \leq x \leq 0.8$), were synthesized by the same powder mixing method, and sintered at 1600 ºC for 4 hours.

Phase compositions and lattice parameters of the solid solutions were identified by X-ray diffraction (XRD, Philips X'Pert) method using Cu K_α radiation. The details of XRD measurement were the same as those described in Chapter 3. Microstructures of the samples were observed by scanning electron microscope (SEM, Philips XL30).

Theoretical density of each composition of the solid solutions was calculated using the lattice parameter obtained from XRD and the molecular weight of a unit cell. Densities of the sintered specimens were measured by Archimede's method.

Electrical properties of the solid solutions were obtained from ac impedance spectroscopy measurements. The detailed descriptions of the impedance measurement can be found in Chapter 3. The conductivity of the sample was corrected to fully-dense value by the Maxwell model, assuming the pores are spherical shape, randomly distributed inside the sample and electrically insulative, written as:

$$\sigma_{dense} = \sigma\left(\frac{1+0.5\Phi}{1-\Phi}\right). \tag{5.1}$$

5.3 Results

5.3.1 Phase composition, lattice parameter and microstructure

Figure 5.1 shows the X-ray diffraction patterns of the solid solutions, which confirms that all the samples are single phase with cubic structure. The lattice parameters of the solid solutions are shown in Figure 5.2, where a linear relationship between the lattice parameter and the mole ratio of CeO_2 can be observed, indicating it follows the Vegard's rule for solid solutions.

Figure 5.3 shows the SEM images of the solid solutions with selected compositions. The grain sizes of the solid solutions vary from 2 – 5 μm, without a clear trend as a function of *x*. For the binary solid solutions YSZ and yttria-doped ceria (YDC), the sintered samples are quite dense, as shown in Figure 5.3(a) and (d). However, for the ternary solid solutions, a certain amount of pores remains in the sintered samples, as illustrated in Figure 5.3(b) and (c).

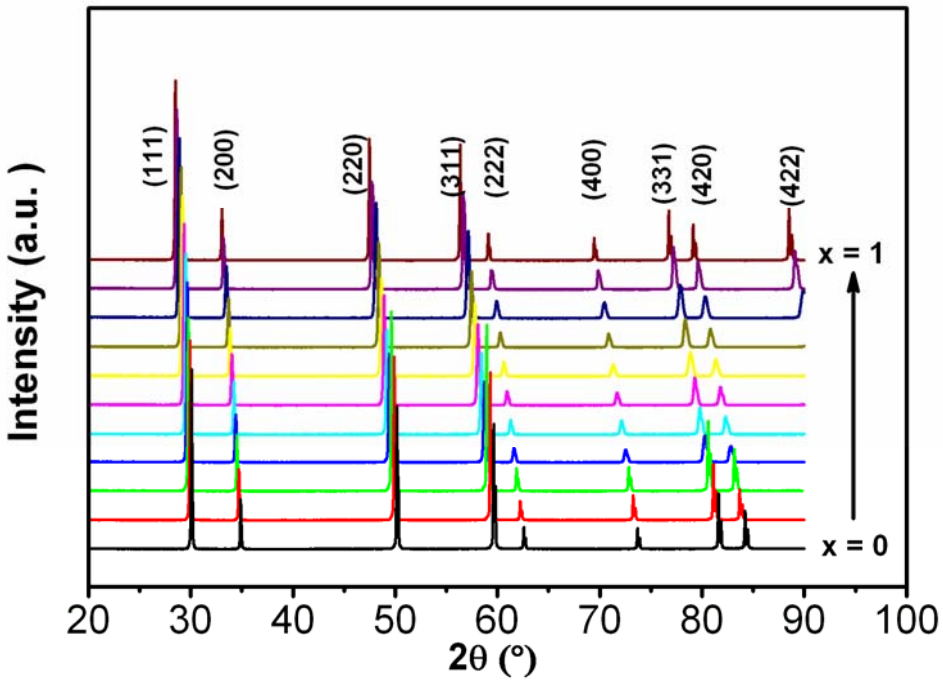

Figure 5.1 X-ray diffraction patterns of the $[(ZrO_2)_{1-x}(CeO_2)_x]_{0.92}(Y_2O_3)_{0.08}$ ($0 \leq x \leq 1$) solid solutions.

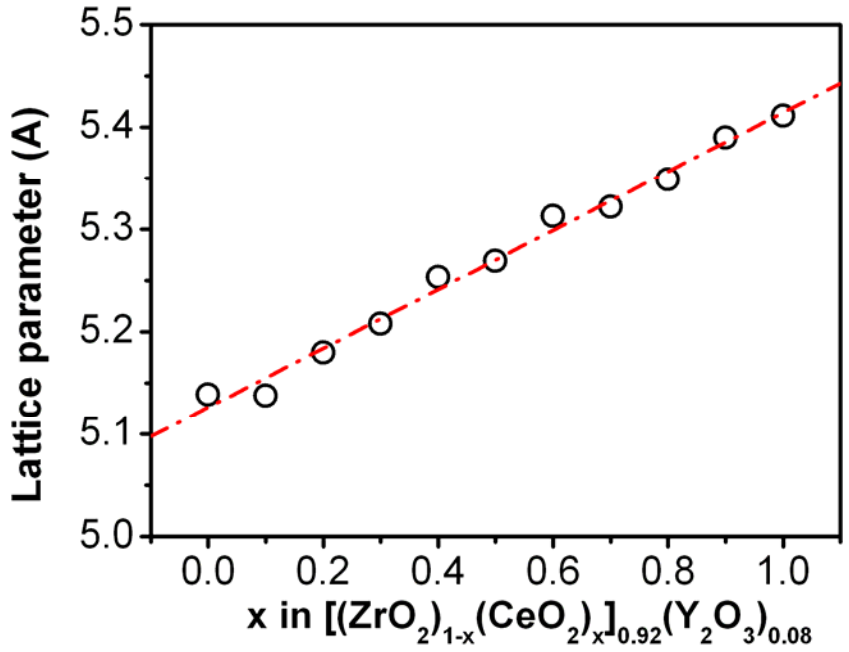

Figure 5.2 Lattice parameters of the $[(ZrO_2)_{1-x}(CeO_2)_x]_{0.92}(Y_2O_3)_{0.08}$ ($0 \leq x \leq 1$) solid solutions.

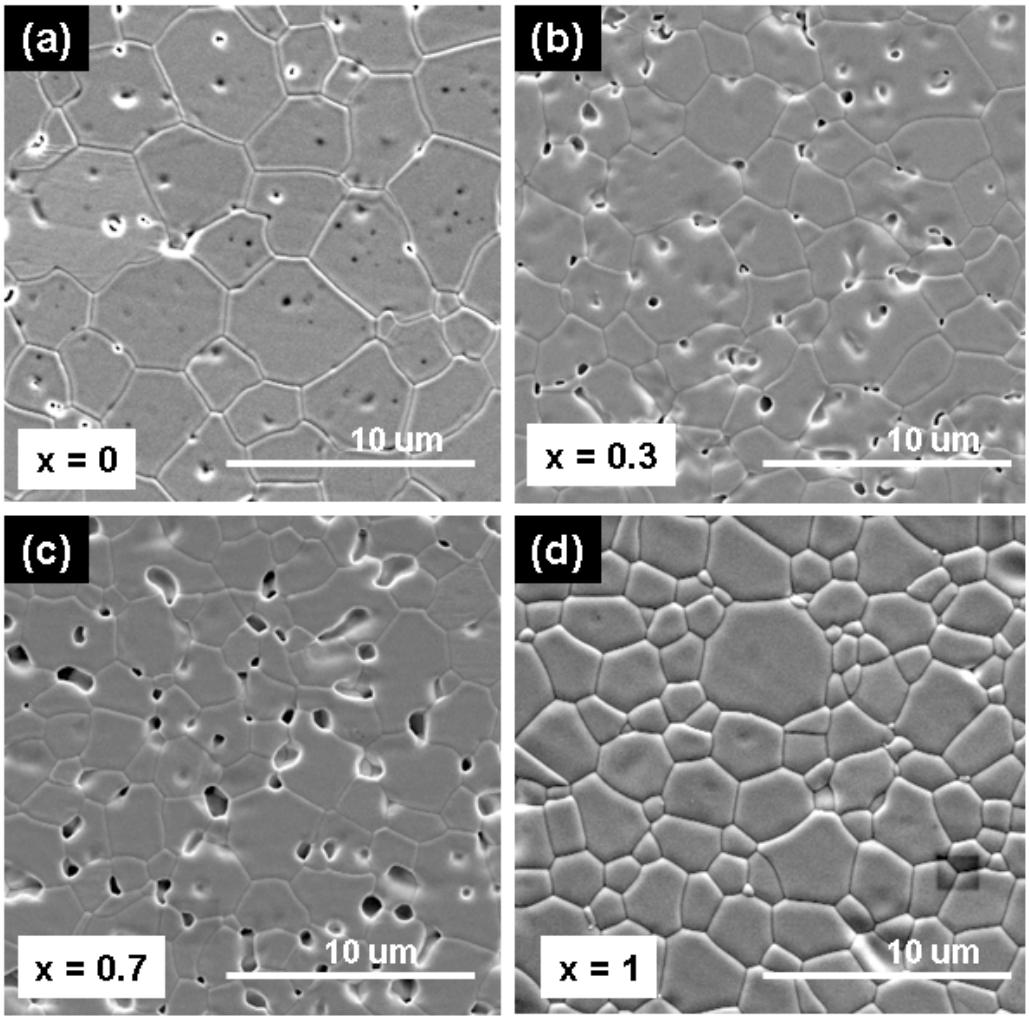

Figure 5.3 Scanning electron micrographs of the solid solutions with selected compositions. (a) $x = 0$; (b) $x = 0.3$; (c) $x = 0.7$ and (d) $x = 1.0$.

5.3.2 Densities

According to the defect reaction:

$$Y_2O_3 \xrightarrow{MO_2} 2Y_M^{'} + V_O^{\bullet\bullet} + 3O_O^x, \qquad (5.2)$$

the composition of the solid solutions can be rewritten as $(Zr_{1-x}Ce_x)_{0.852}Y_{0.148}O_{1.926}$ ($0 \leq x \leq 1$). Thus the theoretical densities of the solid solutions can be calculated by:

$$\rho_{theoretical} = \frac{4[0.852M_{Zr}(1-x) + 0.852M_{Ce}x + 0.148M_Y + 1.926M_O]}{N_0 a_0^3}, \qquad (5.3)$$

where M is the atomic weight, N_0 is the Avogadro's constant and a_0 is the lattice parameter. The calculated theoretical densities and the measured values of selected compositions of the solid solutions are listed in Table 5.1.

Table 5.1 Densities of the solid solutions.

x	Theoretical density (g/cm^3)	Measured density (g/cm^3)	Relative density (%)	Porosity (%)
0	5.96	5.78 ± 0.04	97.0	3.0
0.1	6.17	5.93 ± 0.02	96.1	3.9
0.3	6.31	5.90 ± 0.07	93.5	6.5
0.5	6.47	5.84 ± 0.05	90.3	9.7
0.7	6.65	5.99 ± 0.08	90.1	9.9
0.8	6.73	6.01 ± 0.04	89.3	10.7
1.0	6.85	6.81 ± 0.02	99.4	0.6

5.3.3 Typical impedance spectra of the solid solutions

First of all, one composition of the solid solutions $[(ZrO_2)_{0.6}(CeO_2)_{0.4}]_{0.92}(Y_2O_3)_{0.08}$ (x = 0.4) was selected to present the typical ac impedance behaviours of the solid solutions. Figure 5.4 shows typical impedance spectra (Nyquist plots) of the solid solutions at various temperatures. Similar to the well-known impedance spectroscopy of YSZ, two semicircles are displayed on the Nyquist plot of the solid solution, from left to right (high frequency to low frequency), representing the response from grain (bulk) and grain boundary, respectively. The measured impedance spectra can be fitted by an equivalent circuit of two parallel-aligned resistance-constant phase element (R-CPE) in series connection, as illustrated by the top-left inset in Figure 5.4. The bulk and grain boundary resistances were obtained from the equivalent circuit fitting results and subsequently converted to conductivity by:

$$\sigma_{bulk} = \frac{1}{R_{bulk}} \frac{t}{A} \tag{5.4}$$

and

$$\sigma_{GB}^{sp} = \frac{1}{R_{GB}} \frac{C_{bulk}}{C_{GB}} \frac{t}{A}, \tag{5.5}$$

where t is the sample thickness and A is the cross section area. The grain boundary conductivity is 2 orders of magnitude lower than the bulk conductivity, which is caused either by the impurity segregation at the grain boundary or the space charge effect due to the oxygen vacancy depletion near the grain boundary region [25]. The temperature

dependence of the bulk and the grain boundary conductivity is shown in the top-right inset figure in Figure 5.4. Both the bulk and the grain boundary conductivity shows a typical thermally activated process that it increases with an increase in the temperature and its dependence on the temperature obeys the Arrhenius law in the form of:

$$\sigma_i = \sigma_{i,0} \exp(-\frac{E_{i,a}}{k_B T}), \tag{5.6}$$

where i represents bulk or grain boundary, σ_0 is a pre-exponential factor, k_B is the Boltzmann constant, T is the absolute temperature and E_a is the activation energy. The activation energies can be obtained from the slope of the Arrhenius plots, with values of 1.08 ± 0.01 eV for bulk conduction and 1.09 ± 0.05 eV for grain boundary conduction.

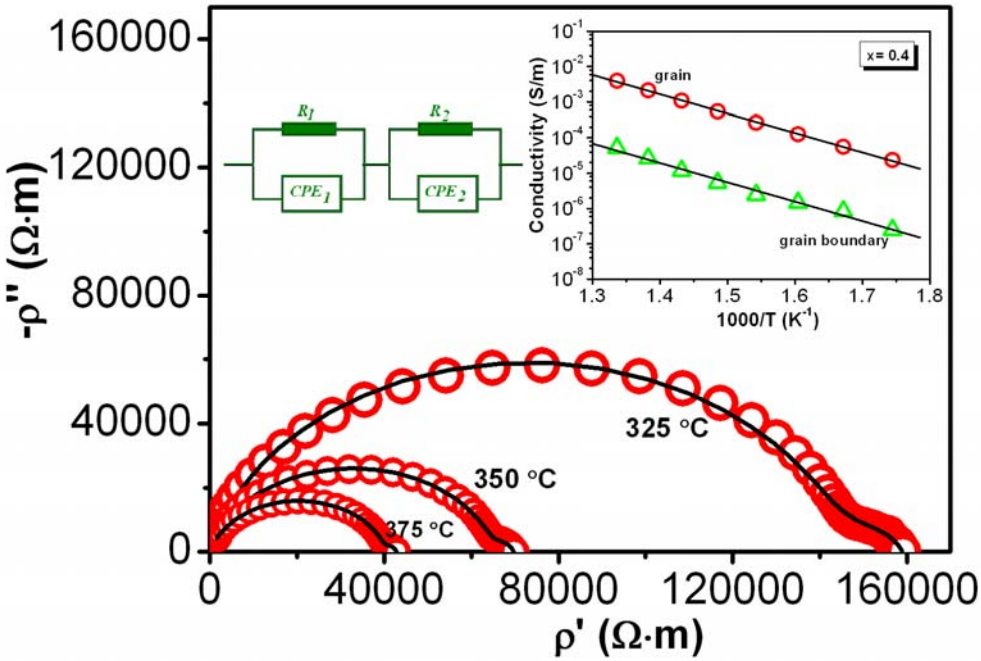

Figure 5.4 Typical Nyquist plots of the solid solutions at various temperatures (x = 0.4 in this case). The red open circles are experimental values, while the black solid lines are the equivalent circuit fitting results. The inset figure on the top-left is the equivalent circuit, and the top-right inset figure shows the Arrhenius plots of the bulk and grain boundary conductivity.

Figure 5.5 shows the Bode plots (imaginary impedance vs frequency) of the selected composition (x = 0.4) at various temperatures. The two peaks on the Bode plot correspond to the two semicircles on the Nyquist plot and the peak height is

proportional to the resistance of each response (diameter of each semicircle). Because the grain boundary resistance is much smaller than the bulk resistance in this sample (see Figure 5.4), the low frequency peak corresponding to the grain boundary response is not obviously distinguished on the Bode plot, but this does not influence the discussion since we mainly focus on the high frequency response (bulk conduction). The frequency at which the peak reaches its maximum is defined as a relaxation frequency ($f_{Z''}$). As shown in the top-left inset in Figure 5.5, the temperature-dependence of $f_{Z''}$ follows the Arrhenius law given by:

$$f_{Z''} = f_0 \exp(-\frac{E_{Za}}{k_B T}), \tag{5.7}$$

where f_0 is the pre-exponential factor, E_{Za} is the activation energy. The activation energy obtained from $f_{Z''}$ is 1.05 ± 0.02 eV. The top-right inset in Figure 5.4 shows the scaling results at different temperatures of the imaginary impedance where ρ''_{max} and $f_{Z''max}$ are used as the scaling parameters for ρ'' and f, respectively. It can be seen all the imaginary impedance collapses into one master curve, indicating the conduction mechanism remains unchanged within this temperature range [26].

The frequency dependence of the imaginary electric modulus (M'') at various temperatures is shown in Figure 5.6. The electric modulus is defined as $M = j\omega C_0 Z$, where ω is the angular frequency and C_0 is the capacitance of an empty cell. In the modulus plot, only one peak corresponding to the bulk is displayed because of its much smaller capacitance value than that of grain boundary. The peak maximum M''_{max} slightly increases with increasing temperature indicating a weak temperature dependence of the dielectric constant of the sample. Similarly, the relaxation frequency at which the imaginary electric modulus reaches its maximum value, defined as $f_{M''}$, shifts to higher frequency range with increasing temperature, and its temperature-dependence also obeys the Arrhenius law, as shown in the top-left inset of Figure 5.6. The activation energy (E_{Ma}) value is 1.07 ± 0.03 eV, which is similar to E_{Za}. In a scaled coordinate, as shown in the top-right inset in Figure 5.6, all the curves collapse into a single master curve, indicating the relaxation describes the same mechanism at various temperatures [27].

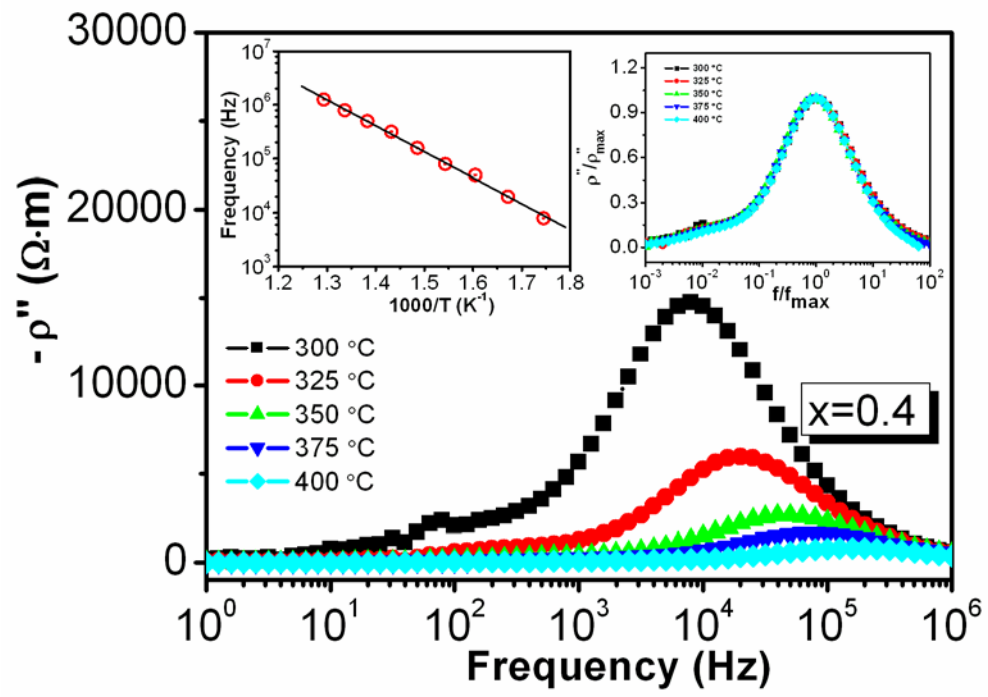

Figure 5.5 Bode plots (imaginary impedance vs frequency) of the solid solution (x = 0.4) at various temperatures. The top-left inset figure shows the Arrhenius plot of the bulk relaxation frequency. The top-right inset figure shows the scaling behaviour of the imaginary impedance.

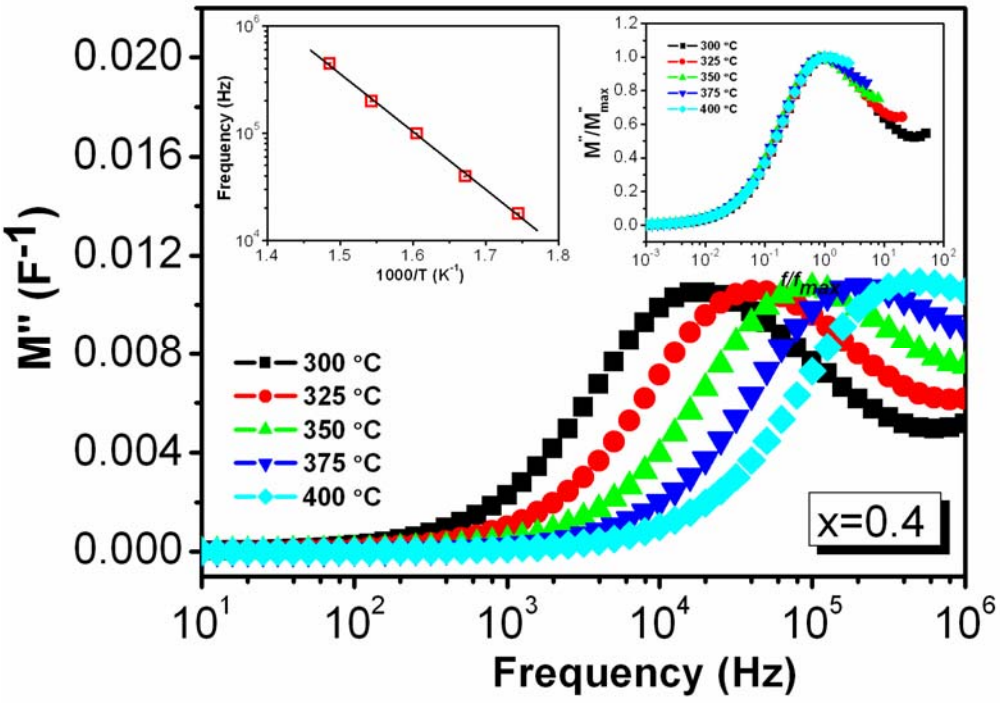

Figure 5.6 Frequency dependence of the imaginary electric modulus (M'') of the solid solution (x = 0.4) at various temperatures. The top-left inset figure shows the Arrhenius plot of the bulk relaxation frequency. The top-right inset figure shows the scaling behaviour of the imaginary electric modulus.

In Figure 5.7, the imaginary impedance (ρ'') and the imaginary modulus (M'') were plotted as a function of frequency. The peaks are not overlapped: the peak position for M'' shifts to a higher frequency region compared to the ρ'' peak. According to reference [28], the overlapping peak position of imaginary impedance and imaginary modulus is evidence of delocalized or long-range relaxation. Therefore, the slight separation of the two peaks (the peak position of *M''* is around half magnitude higher than that of *ρ''*) suggests the components from both long-range and localized relaxation [29].

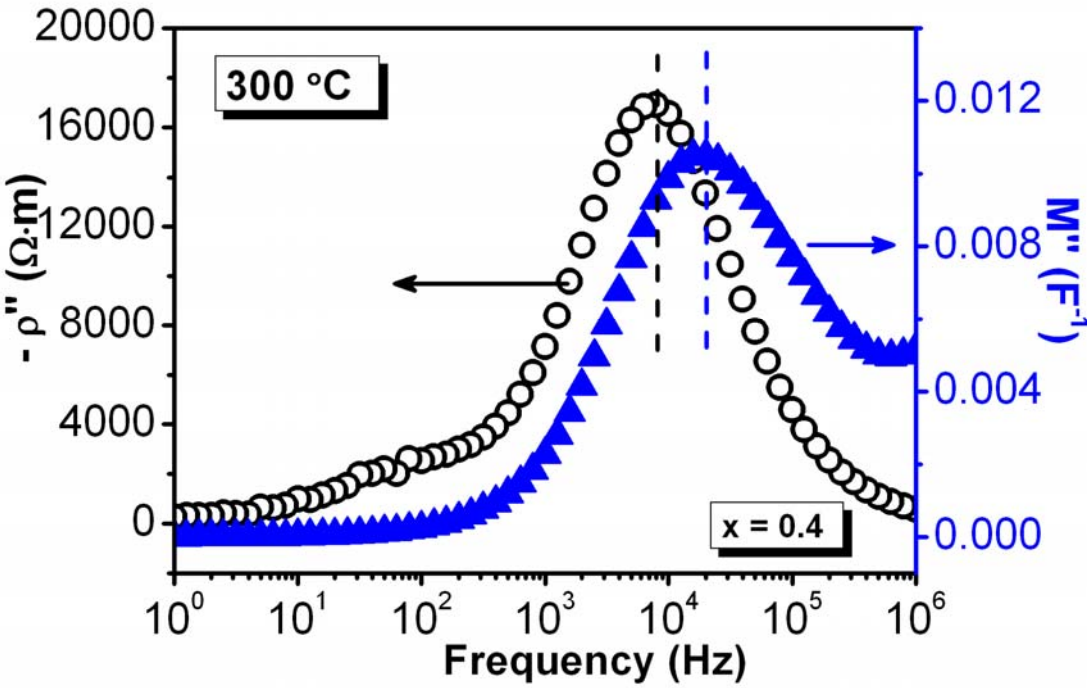

Figure 5.7 Frequency dependence of the imaginary impedance (*ρ''*) and the imaginary electric modulus (*M''*) of the solid solution (x = 0.4) at 300 ºC.

5.3.4 Composition dependence of the bulk conductivity

Figure 5.8 shows the composition dependence of the bulk conductivity of the solid solutions at various temperatures. The bulk conductivity has been corrected into fully-dense value according to Eq.(5.1). With the increase in the CeO_2 mole ratio, the conductivity first decreases, reaching a minimum around x = 0.5, and increases afterward. The "V-shape" variation of the bulk conductivity as a function of the mole

ratio of CeO_2 indicates that the ternary solid solution deteriorates the electrical conductivity of $(ZrO_2)_{0.92}(Y_2O_3)_{0.08}$ and $(CeO_2)_{0.92}(Y_2O_3)_{0.08}$ binary systems. The inset in Figure 5.8 shows the relaxation frequencies obtained from imaginary impedance and imaginary modulus and their dependence on the composition of the solid solutions at a chosen temperature. It is noticeable that $f_{Z''}$ is lower than $f_{M''}$ for all the compositions, indicating the existence of both long-range and localized relaxations in the solid solutions. On the other hand, the composition dependence of $f_{Z''}$ and $f_{M''}$ has a similar trend as the bulk conductivity.

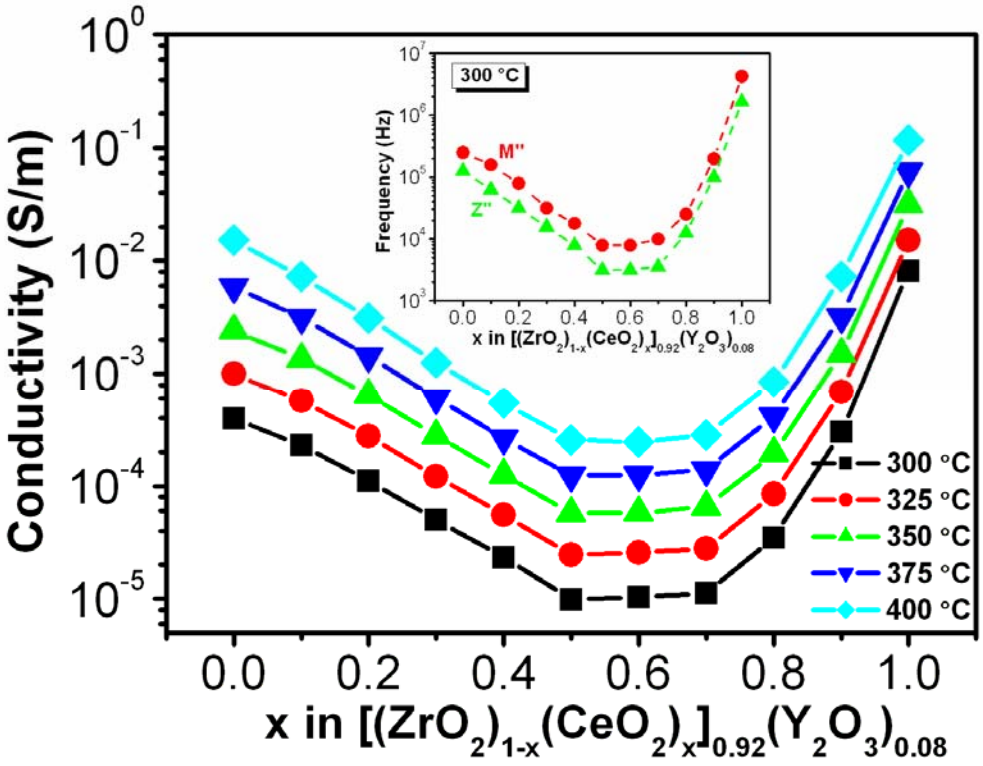

Figure 5.8 Composition dependence of the bulk conductivity of the $[(ZrO_2)_{1-x}(CeO_2)_x]_{0.92}(Y_2O_3)_{0.08}$ ($0 \leq x \leq 1$) solid solutions at various temperatures. The inset figure shows the composition dependence of relaxation frequencies obtained from imaginary modulus ($f_{M''}$) and imaginary impedance ($f_{Z''}$) at 300 ºC.

Figure 5.9 shows the composition dependence of the activation energy for the bulk conduction. The activation energy has a decreasing trend, although not linearly, with an increase in x. Slight decrease of the activation energy is observed when $x < 0.5$, while a rapid drop of the activation energy occurs when $x > 0.5$.

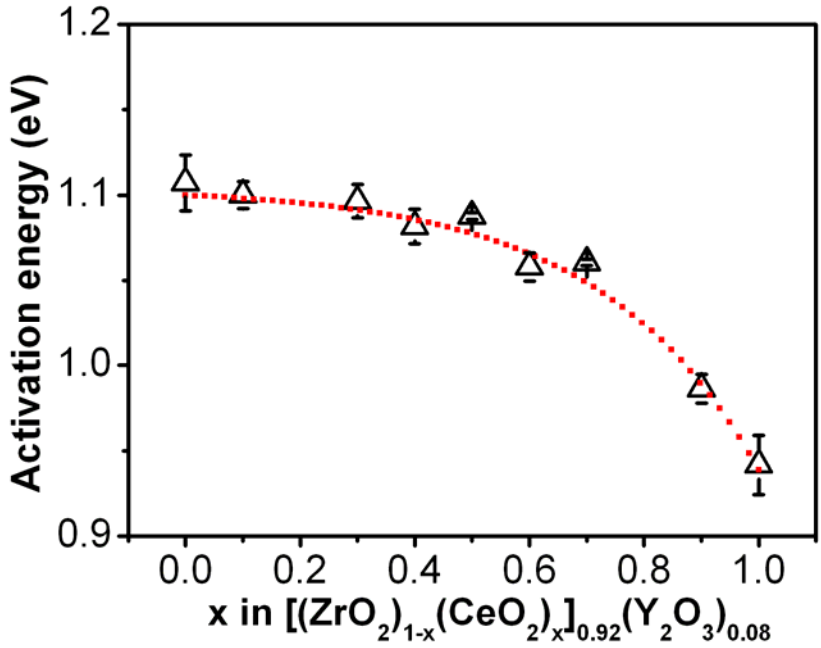

Figure 5.9 Composition dependence of the activation energy for the bulk conduction. The hollow triangles are the experimental values obtained from the Arrhenius plot of the bulk conductivity. The red dot is the trend line.

5.4 Discussions

5.4.1 Relationship between the relaxation frequencies and the conductivity

On the Bode plot (imaginary impedance *vs* frequency), a relaxation frequency is obtained where the imaginary impedance reaches its maximum value. In an ideal case of an equivalent circuit of a resistor and a capacitor in parallel connection, the imaginary impedance is expressed as:

$$-Z'' = \frac{\omega R^2 C}{1+\omega^2 R^2 C^2}, \tag{5.8}$$

where ω is the angular frequency, R is the resistance and C is the capacitance. Maximum of $-Z''$ is obtained when $\omega = \frac{1}{RC}$. The bulk resistance and capacitance are determined by its conductivity (σ), dielectric constant (ε) and its geometries (t and A as defined in Eq.(5.4) and (5.5)). Therefore the relaxation frequency $f_{Z''}$ can be expressed by:

$$f_{Z''} = \frac{1}{2\pi}\frac{1}{RC} = \frac{1}{2\pi}\frac{1}{\left(\frac{1}{\sigma}\frac{t}{A}\right)\cdot\left(\varepsilon\frac{A}{t}\right)} = \frac{1}{2\pi}\frac{\sigma}{\varepsilon}. \quad (5.9)$$

In ZrO_2 based ceramics, the dielectric constant is usually insensitive to the composition of the material [30, 31] As a result, $f_{Z''}$ is only determined by the conductivity ($f_{M''}$ has the same expression as $f_{Z''}$ in Eq.(5.9)). A direct proportional relationship can be established between the relaxation frequency and the conductivity.

In the real case, the capacitance response is not a pure capacitor, thus the expression for $f_{Z''}$ will be different from Eq.(5.9). But for bulk impedance (high frequency response on the Nyquist plot), the deviation from a capacitor is small. Therefore, Eq.(5.9) can still be used to describe the relationship between $f_{Z''}$ and σ. Comparing the relaxation frequency can be a simple method to rank the bulk conductivity of the solid solutions.

5.4.2 Origin of the localized relaxation/conduction

When ZrO_2 or CeO_2 is doped with Y_2O_3, oxygen vacancies are generated via the defect reaction as described in Eq.(5.2). However, due to the coulomb interaction, some of the oxygen vacancies $V_O^{\bullet\bullet}$ may bind to the dopant ions and form the defect associates $(Y_M^{'} - V_O^{\bullet\bullet})$. It is usually accepted the orientation of the defect associates under an applied electric field contributes to the localized relaxation [32]. On the other hand, the free oxygen vacancies also contribute to a localized conduction, as discussed below.

The ionic radii of Zr^{4+} and Y^{3+} are 0.084 and 0.1019 nm respectively [33], while the ionic radius of Ce^{4+} has different reference values, varies from 0.097 [34], 0.101 [35] to 0.110 nm [36]. However, it is clear that the ionic radius of Y^{3+} is close to Ce^{4+} but it is significantly larger than Zr^{4+}. Density functional theoretical studies by Andersson *et al.* [37] reported that the formation of an anionic vacancy is correlated to the ionic radius of the dopant ion. With respect to the dopant ion, there are three positions, named the first nearest neighbour (1NN), second nearest neighbour (2NN) and third nearest neighbour (3NN), for the oxygen vacancy to locate, as illustrated in Figure 5.10. 1NN position is

favourable for the oxygen vacancy when the dopant ion has an ionic radius closer to the host cation, and the 2NN position is favourable when the dopant ion has an ionic radius considerably larger than the host cation. Therefore, when Y^{3+} ions substitutes Zr^{4+} ions, oxygen vacancy locates at the 2NN positions (close to Zr centre); when Y^{3+} ions substitutes Ce^{4+} ions, oxygen vacancy locates at the 1NN positions (close to Y centre).

Dholabhai *et al.* calculated the activation energies for vacancy migration along different paths in Praseodymium doped ceria [38] and gadolinium doped ceria [36]. The former can be extended to represent the cases where the ionic radius dopant ion is larger than that of the host ion; while the latter can be extended to represent the case where the ionic radii of the dopant and the host have similar values. According to their calculation results, in both cases the preferred migration pathway for oxygen vacancy diffusion is between 1NN and 2NN sites. For example, in yttria-doped ceria, the oxygen vacancy is located at the 1NN position. For migration, it will jump to 2NN position first, and then it is of high possibility that it jumps back to the 1NN site because the jump from 2NN to 1NN has lower activation energy compared with the jumps from 2NN to 2NN or from 2NN to 3NN sites. The back-and-forth jump between two sites contributes to the localized conduction.

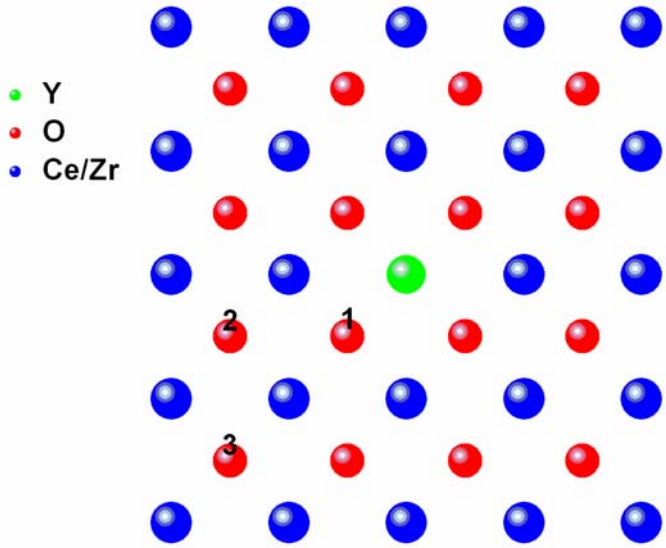

Figure 5.10 A schematic top view of the possible sites of oxygen vacancies around a dopant ion. Numbers 1, 2 and 3 represent 1NN, 2NN and 3NN oxygen ions with respect to the dopant (Y) ion.

To sum up, the localized relaxation is from the orientation of the defect associates under the electric field and the back-and-forth jump between two sites of a free oxygen vacancy.

5.4.3 Composition dependence of the ionic conductivity and the activation energy

In Figure 5.8, a "V-shape" variation of the bulk conductivity as a function of x is observed. Similar trend of the composition dependence of the electrical conductivity in ZrO_2-CeO_2-Y_2O_3 solid solutions has been reported by Ananthapadmanabhan *et al.* [24]. They attributed this V-shape variation to the increased scattering of the oxygen ions by the substitution of Zr by Ce atoms or Ce by Zr atoms, which is analogical to the mechanism of enhanced electrical resistivity in an alloy system. This interpretation is unconvincing to some point that the hopping mechanism in an ionic conductor is totally different from the scattering mechanism of electrons in metals and alloys. Kawamura *et al.* [20] also found the "V-shape" composition dependence of the conductivity in CaO doped ZrO_2-CeO_2 solid solutions, however they did not give any further explanations on the results. In the following paragraphs the composition dependence of the conductivity will be discussed.

Within the studied temperature range, the electrical conduction in the solid solutions is purely ionic. Therefore, the variation of the bulk conductivity as a function of the composition is either caused by the change of the oxygen vacancy concentration or its mobility. Here we divide the "V-shape" variation as a function of the composition in Figure 5.8 into two regions: the CeO_2-rich ($x > 0.5$) and the ZrO_2-rich ($x < 0.5$) regions and discuss them separately.

The increase of the ionic conductivity with the increase of x in the CeO_2-rich region is easier to understand to some extent. In the fluorite structure, the ionic conduction is caused by the migration of oxygen vacancies through channels formed by the neighbouring cations. As discussed by Ananthapadmanabhan *et al.* [24] and Tsoga *et al.* [20], the radius of the free channel increases with the lattice parameter. Larger channel radius is favourable for the charge carriers to migrate. Since the amount of Y_2O_3 is set constant for all the compositions, the concentration of oxygen vacancies remains almost

the same (the slight increase in the lattice volume leads to a slight decrease of the defect concentration, but this effect is negligible [24]). Therefore, the increase of ionic conductivity in the CeO_2-rich region with increasing x can be attributed to the increased oxygen vacancy mobility through a larger channel.

However, in the ZrO_2-rich region ($x < 0.5$), the increased channel radius fails to explain the decreased ionic conductivity with increasing x. The possible reason for the decreased conductivity in the ZrO_2-rich region with increasing CeO_2 mole ratio is the formation of complex defect associates or clusters. It is well known that 8 mol% YSZ has the highest electrical conductivity. Further increases in dopant concentration decrease the conductivity in YSZ because of the formation of defect associates, which bind the oxygen vacancies to the yttrium ions, making the oxygen vacancies unavailable for conduction [25]. The introduction of CeO_2 into YSZ has similar effect: when CeO_2 is introduced into ZrO_2, additional oxygen vacancies can be generated due to the significant difference of the ionic radius between Ce^{4+} and Zr^{4+} (which is called "size effect") by the following reaction [39]:

$$CeO_2 \xrightarrow{ZrO_2} Ce_{Zr}^{x} + 2V_O^{\bullet\bullet} + 2O_i^{''}. \qquad (5.10)$$

The oxygen vacancies generated by CeO_2 addition makes the formation of $(Y_{Zr}^{'}V_O^{\bullet\bullet})$ becomes more significant, and possibly leads to more complex defect associates $(Y_{Zr}^{'}V_O^{\bullet\bullet}Y_{Zr}^{'})^x$, which has been found in 9 mol% Y_2O_3 doped ZrO_2 [40]. The formation of defect associates has stronger effect over the increase in the lattice parameter, and consequently leads to a decreasing conductivity.

To sum up, the "V-shape" variation of the bulk conductivity as a function of x in the solid solutions is a competition between two factors. The first one is the formation of defect associates, which limits the mobility of the oxygen vacancies and therefore decreases the conductivity; the second one is the increase of lattice parameter, which enlarges the free channel for oxygen vacancy migration and therefore increases the conductivity. In the ZrO_2-rich region ($x < 0.5$), the formation of defect associates overshadows the effect of the increased lattice parameter, therefore the conductivity decreases with increasing x; in the CeO_2-rich region ($x > 0.5$), the increase of lattice parameter is the dominant factor which leads to an up-going trend on the conductivity.

A schematic of the defect associates profile and lattice parameter as a function of *x* and their competitive effect on the bulk conductivity of the solid solutions is shown in Figure 5.11(a).

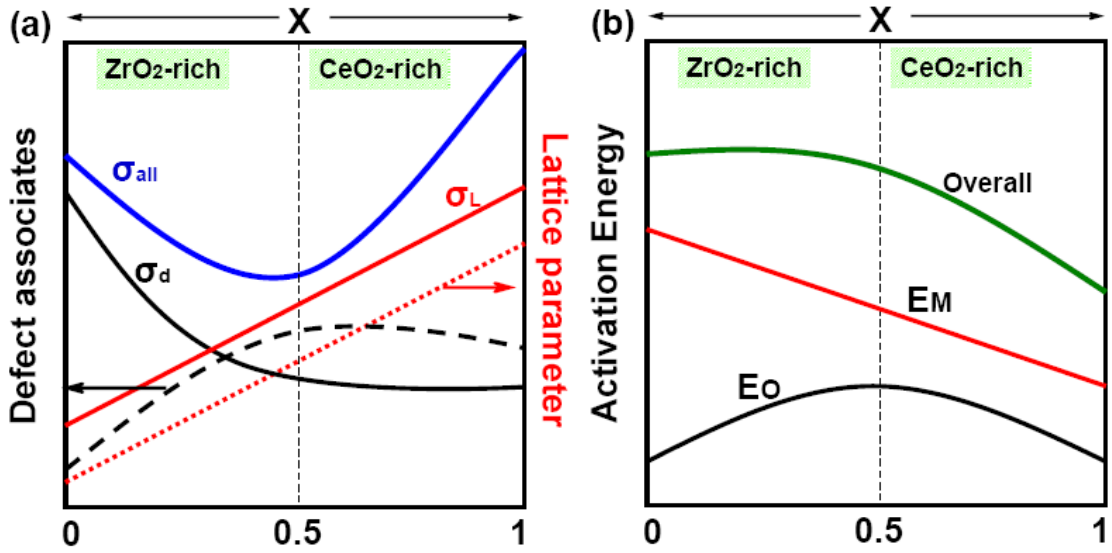

Figure 5.11 (a) Schematic of the defect associates profile (black dash line) and lattice parameter (red dot line) as a function of the composition (*x*). The black solid line illustrates the conductivity decrease caused by increasing defect associates; the red solid line illustrates the conductivity increase due to larger lattice parameter; the blue solid line shows the competitive effect of the two factors on the bulk conductivity of the solid solutions. (b) Schematic of the competitive effect of lattice parameter and the defect associates on the activation energy for the bulk conduction.

The defect associates and the lattice parameter also influence the activation energy for the bulk conduction, as illustrated in Figure 5.11(b). It is accepted that the activation energy for the oxygen diffusion (oxygen vacancy diffusion in an opposite direction) in the intermediate temperature range is comprised of migration energy for a free oxygen vacancy (E_M) and the dissociation energy (E_O) to extricate an oxygen vacancy from the defect associates. As discussed above, the increase of lattice parameter leads to more free space and makes it much easier for an oxygen vacancy to migrate, and therefore a lower E_M. E_O is dependent on the concentration of defect associates. More defect associates, more energy required to dissociate them. Therefore E_O varies as a function of *x* in the same way as the concentration of defect associates. Since E_M has higher values than E_O [41], in the ZrO_2-rich region, the increased E_O slows down the decrease

of E_M, therefore the activation energy shows quite smooth variation; while a rapid drop of the activation energy can be observed in the CeO_2-rich region because E_M and E_O both decrease as a function of x. The experimental observation in Figure 5.9 is in agreement with the above analysis.

From the above analysis it can be concluded that the "V-shape" variation of the bulk conductivity with increasing CeO_2 mole ratio is because the ionic radius of Ce^{4+} is significantly larger than Zr^{4+}. Therefore, the ionic radius of the tetravalent dopant determines the composition dependence of the ionic conductivity of the solid solutions. It can be predicted if Zr is substituted by another tetravalent element with the similar ionic radius with Zr^{4+}, "V-shape" composition dependence of the bulk conductivity may not be observed.

In order to testify the above prediction, another series of binary solid solution $[(ZrO_2)_{1-x}(HfO_2)_x]_{0.87}(Y_2O_3)_{0.13}$ ($0 \le x \le 0.8$) has been investigated. The bulk conductivity and the activation energy were obtained using the same method as the ZrO_2-CeO_2-Y_2O_3 series. The ionic radius of Hf^{4+} is 0.083 nm, almost the same as Zr^{4+} (0.084 nm), thus the substitution of Zr^{4+} by Hf^{4+} will not cause the re-arrangement of oxygen vacancies (no "size effect"). Besides at given yttria concentration, yttria-stabilized hafnia has lower ionic conductivity and higher activation energy than YSZ [42], therefore we expect a monotonously decrease of the bulk conductivity, along with a monotonously increase of the activation energy as a function of x. As shown in Figure 5.12(a) and (b), both the variations of the bulk conductivity and the activation energy as a function of x are in accordance with the expectations. No "V-shape" composition dependence of the bulk conductivity is observed, which confirms the prediction and from the other side supports the validity of the above explanation of the "V-shape" composition dependence of the bulk conductivity in ZrO_2-CeO_2-Y_2O_3 solid solutions.

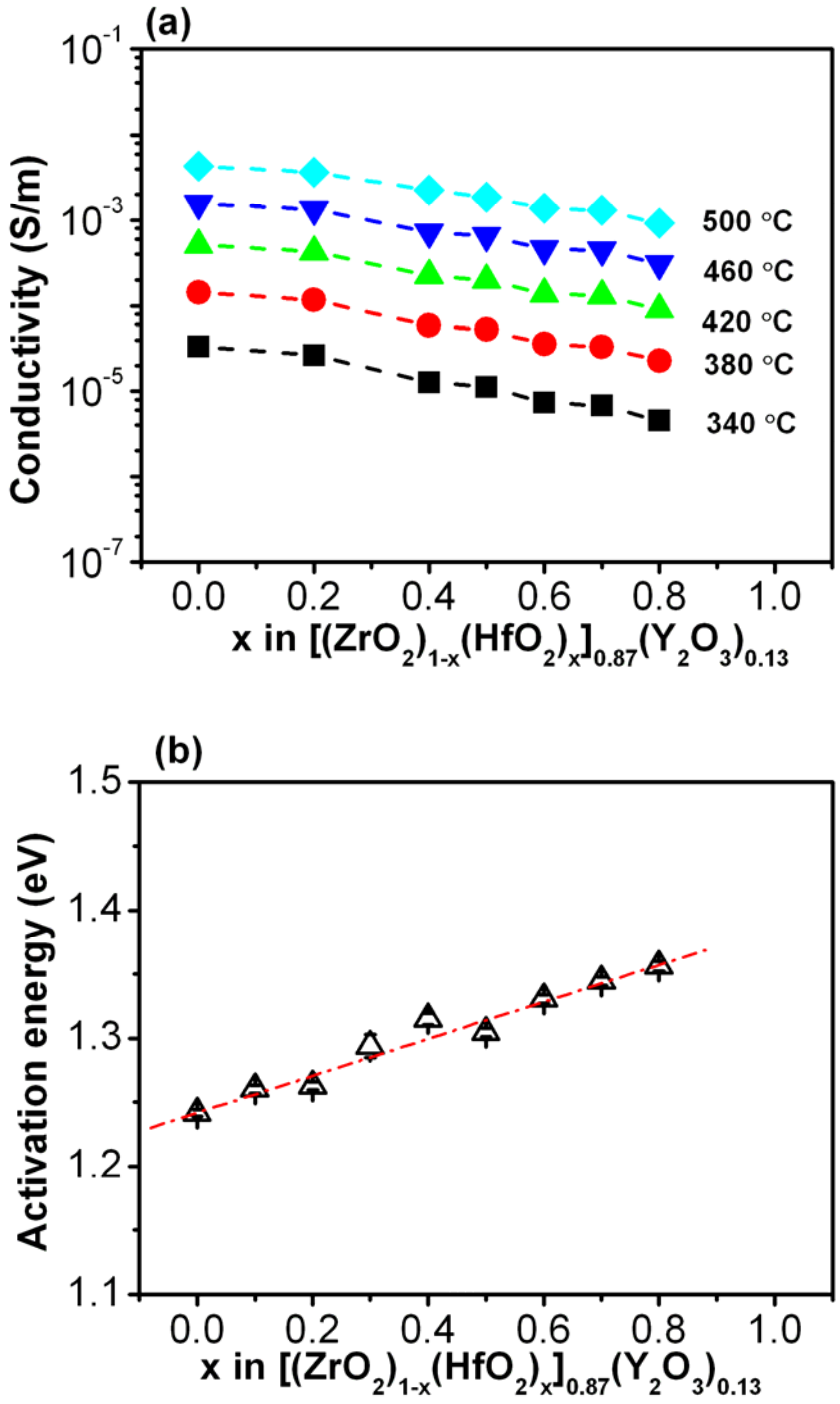

Figure 5.12 Composition dependence of (a) bulk conductivity and (b) activation energy of the $[(ZrO_2)_{1-x}(HfO_2)_x]_{0.87}(Y_2O_3)_{0.13}$ ($0 \leq x \leq 0.8$) solid solutions at various temperatures.

5.5 Conclusions

In this chapter, the bulk conduction and relaxation of the $[(ZrO_2)_{1-x}(CeO_2)_x]_{0.92}(Y_2O_3)_{0.08}$ ($0 \leq x \leq 1$) solid solutions were studied using impedance spectroscopy at intermediate temperatures (200 - 500 ºC). The main conclusions are:

(1) The impedance spectra of the solid solutions of all the compositions show similar characteristic of the well-established impedance spectra of YSZ;

(2) The relaxation frequencies determined from the Bode plots ($f_{Z''}$ and $f_{M''}$) is proportional to the bulk conductivity. Comparing the relaxation frequency can be a simple method to rank the bulk conductivity of the solid solutions;

(3) The electrical response of the solid solutions for all the compositions under the ac electrical field shows both long-range and localized relaxations. It is assumed that the localized relaxations are from the orientation of the defect associates under the electric field, as well as the back-and-forth jumping of a free oxygen vacancy between the two sites through which the diffusion path has the lowest activation energy;

(4) The bulk conductivity has a "V-shape" variation as a function of the composition: it decreases with an increase of the mole ratio of CeO_2 (x), reaching the lowest value when $x = 0.5$ (Zr/Ce = 1), and then goes up with further increase of x. The decrease of the bulk conductivity with increasing x in the ZrO_2-rich region ($x < 0.5$) is due to the formation of the defect associates which limits the mobility of the oxygen vacancies, while the increase of the bulk conductivity with increasing x in the CeO_2-rich region ($x > 0.5$) is due to the increase of the lattice parameter which enlarges the free channel for oxygen vacancy migration. These two factors also influence the activation energy for the bulk conduction;

(5) The ionic radius of the tetravalent dopant determines the composition dependence of the ionic conductivity of the solid solutions. When doping YSZ with other tetravalent dopant with similar ionic radius with Zr^{4+}, e.g., Hf^{4+}, such "V-shape" composition dependence of the bulk conductivity can not be observed.

Reference

[1] T. Hibino, A. Hashimoto, T. Inoue, J. Tokuno, S. Yoshida and M. Sano, *A low-operating-temperature solid oxide fuel cell in hydrocarbon-air mixtures*, Science **288** (2000) 2031-2033.

[2] S. C. Singhal, *Solid oxide fuel cells for stationary, mobile, and military applications*, Solid State Ionics **152-153** (2002) 405-410.

[3] W. C. Maskell, *Progress in the development of zirconia gas sensors*, Solid State Ionics **134** (2000) 43-50.

[4] A. Q. Pham and R. S. Glass, *Oxygen pumping characteristics of yttria-stabilized-zirconia*, Electrochimica Acta **43** (1998) 2699-2708.

[5] J. B. Goodenough, *Oxide-ion conductors by design*, Nature **404** (2000) 821-823.

[6] K. J. Moreno, A. F. Fuentes, M. Maczka, J. Hanuza, U. Amador, J. Santamaria and C. Leon, *Influence of thermally induced oxygen order on mobile ion dynamics in* $Gd_2(Ti_{0.65}Zr_{0.35})_2O_7$, Physical Review B **75** (2007) 184303.

[7] S. P. S. Badwal, *Zirconia-based solid electrolytes: microstructure, stability and ionic conductivity*, Solid State Ionics **52** (1992) 23-32.

[8] O. J. Dura, M. A. Lopez de la Torre, L. Vazquez, J. Chaboy, R. Boada, A. Rivera-Calzada, J. Santamaria nd C. Leon, *Ionic conductivity of nanocrystalline yttria-stabilized zirconia: grain boundary and size effects*, Physical Review B **81** (2010) 184301.

[9] X. Guo and R. Yuan, *On the grain boundaries of* ZrO_2*-based solid electrolyte*, Solid State Ionics **80** (1995) 159-166.

[10] X. Guo, W. Sigle, J. Fleig and J. Maier, *Role of space charge in the grain boundary blocking effect in doped zirconia*, Solid State Ionics **154-155** (2002) 555-561.

[11] X. Guo and R. Waser, *Space charge concept for acceptor-doped zirconia and ceria and experimental evidences*, Solid State Ionics **173** (2004) 63-67.

[12] H. Inaba and H. Tagawa, *Ceria-based solid electrolytes*, Solid State Ionics **83** (1996) 1-16.

[13] F. Zhao and A. V. Virkar, *Effect of morphology and space charge on conduction through porous doped ceria*, Journal of Power Sources **195** (2010) 6268-6279.

[14] S. Omar, E. D. Wachsman, J. L. Jones and J. C. Nino, *Crystal structure-ionic conductivity relationships in doped ceria systems*, Journal of the American Ceramic Society **92** (2009) 2674-2681.

[15] H. Yamamura, S. Takeda and K. Kakinuma, *Dielectric relaxations in the* $Ce_{1-x}Nd_xO_{2-\delta}$ *system*, Solid State Ionics **178** (2007) 1059-1064.

[16] Z. G. Lv, P. Yao, R. S. Guo and F. Y. Dai, *Study on zirconia solid electrolytes doped by complex additives*, Materials Science and Engineering A **458** (2007) 355-360.

[17] B. C. H. Steele, *Appraisal of* $Ce_{1-y}Gd_yO_{2-y/2}$ *electrolytes for IT-SOFC operation at 500 ºC*, Solid State Ionics **129** (2000) 95-110.

[18] A. Trovarelli, *Catalytic properties of ceria and* CeO_2*-containing materials*, Catalysis Reviews, Science and Engineering **38** (1996) 439-520.

[19] G. A. Tompsett and N. M. Sammes, *Ceria-yttria-stabilized zirconia composite ceramic systems for applications as low-temperature electrolytes*, Journal of the American Ceramic Society **80** (1997) 3181-3186.

[20] A. Tsoga, A. Naoumidis and D. Stöver, *Total electrical conductivity and defect structure of* ZrO_2-CeO_2-Y_2O_3-Gd_2O_3 *solid solutions*, Solid State Ionics **135** (2000) 403-409.

[21] K. Kawamura, K. Watanabe, T. Hiramatsu, A. Kaimai, Y. Nigara, T. Kawada and J. Mizusaki, *Electrical conductivities of CaO doped* ZrO_2-CeO_2 *solid solution system*, Solid State Ionics **144** (2001) 11-18.

[22] B. Cales and J. F. Baumard, Mixed conduction and defect structure of ZrO_2-CeO_2-Y_2O_3 solid solutions, Journal of the Electrochemical Society **131** (1994) 2407-2413.

[23] H. Arashi, H. Naito and M. Nakata, *Electrical properties in the* ZrO_2-CeO_2-Y_2O_3 *system*, Solid State Ionics **76** (1995) 315-319.

[24] P. V. Ananthapadmanabhan, N. Venkatramani, V. K. Rohatgi, A. C. Momin and K. S. Venkateswarlu, *Structure and ionic conductivity of solid solutions in the system* $0.9\{(ZrO_2)_{1-x}$-$(CeO_2)_x\}$-$0.1(Y_2O_3)$, Journal of the European Ceramic Society **6** (1990) 111-117.

[25] X. Guo and R. Waser, *Electrical properties of the grain boundaries of oxygen ion conductors: Acceptor-doped zirconia and ceria*, Progress in Materials Science **51** (2006) 151-210.

[26] J. Hou, R. Vaish, Y. Qu, D. Krsmanovic, K. B. R. Varma and R. V. Kumar, *Dielectric relaxation and electrical conductivity in Bi_5NbO_{10} oxygen ion conductors prepared by a modified sol-gel process*, Journal of Power Sources **195** (2010) 2613-2618.

[27] S. Saha, T. P. Sinha, *Dielectric relaxation in $SrFe_{1/2}Nb_{1/2}O_3$*, Journal of the Applied Physics **99** (2006) 014109.

[28] R. Gerhardt, *Impedance and dielectric spectroscopy revisited: distinguishing localized relaxation from long-range conductivity*, Journal of Physics and Chemistry of Solids **55** (1994) 1491-1506.

[29] A. Dutta and T. P. Sinha, *Dielectric relaxation in perovskite $BaAl_{1/2}Nb_{1/2}O_3$*, Journal of Physics and Chemistry of Solids **67** (2006) 1484-1491.

[30] X. Guo and J. Maier, *Grain boundary blocking effect in zirconia: a Schottky barrier analysis*, Journal of the Electrochemical Society **148** (2001) E121-E126.

[31] M. C. Steil, F. Thevenot and M. Kleitz, *Densification of yttria-stabilized zirconia*, Journal of the Electrochemical Society **144** (1997) 390-398.

[32] H. Yamamura, S. Takeda and K. Kakinuma, *Relationship between oxide-ion conductivity and dielectric relaxation in Sm-doped CeO_2*, Solid State Ionics **178** (2007) 889-893.

[33] M. R. Winter and D. R. Clarke, *Thermal conductivity of yttria-stabilized zirconia-hafnia solid solutions*, Acta Materialia **54** (2006) 5051-5059.

[34] R. D. Shannon and C. T. Prewitt, *Effective ionic radii in oxides and fluorides*, Acta Crystallographica Section B **25** (1969) 925-946.

[35] T. L. Wen, Z. Y. Lu and Z. Xu, *Proton conductor of $SrCe_{0.95}Ln_{0.05}O_x$ (Ln = Eu, Sm, Ho, Tm)*, Journal of Materials Science Letters **13** (1994) 1032-1034.

[36] P. P. Dholabhai, J. B. Adams, P. Crozier and R. Sharma, *A density functional study of defect migration in gadolinium doped ceria*, Physical Chemistry Chemical Physics **12** (2010) 7904-7910.

[37] D. A. Andersson, S. I. Simak. N. V. Skorodumova, I. A. Abrikosov and B. Johansson, *Optimization of ionic conductivity in doped ceria*, Proceedings of the National Academy of Sciences of the United States of America **103** (2006) 3518-3521.

[38] P. P. Dholabhai, J. B. Adams, P. Crozier and R. Sharama, Oxygen vacancy migration in ceria and Pr-doped ceria: a DFT + U study, The Journal of Chemical Physics **132** (2010) 094104.

[39] J. H. Lee, S. M. Yoon, B. K. Kim, J. Kim, H. W. Lee and H. S. Song, *Electrical conductivity and defect structure of yttria-doped ceria-stabilized zirconia*, Solid State Ionics **144** (2001) 175-184.

[40] X. Guo and Z. Wang, *Effect of niobia on the defect structure of yttria-stabilized zirconia*, Journal of the European Ceramic Society **18** (1998) 237-240.

[41] Y. Arachi, H. Sakai, O. Yamamoto, Y. Takeda and N. Imanishai, *Electrical conductivity of the ZrO_2-Ln_2O_3 (Ln = lanthanides) system*, Solid State Ionics **121** (1999) 133-139.

[42] M. F. Trubelja and V. S. Stubican, *Ionic conductivity of the fluorite-type hafnia-R_2O_3 solid solutions*, Journal of the American Ceramic Society **74** (1991) 2489-2494.

Chapter 6

Thermal conductivity of $[(ZrO_2)_{1-x}(CeO_2)_x]_{0.92}(Y_2O_3)_{0.08}$ ($0 \leq x \leq 1$) solid solutions

6.1 Introduction

Zirconia-based ceramics are the state-of-art materials for thermal barrier coatings (TBCs). Pure zirconia is not suitable for such application due to two main disadvantages. First, the thermal conductivity of pure zirconia is not low enough to meet the demand of a thermal barrier function. Second, its phase transformation from the high temperature tetragonal phase to the room temperature monoclinic phase causes volume expansion and leads to crack and failure of the coating. The above two disadvantages can be overcome by doping other metal oxides into zirconia. Numerous studies have found that dopants play an important role both in decreasing the thermal conductivity and stabilizing the high temperature tetragonal or cubic phases of zirconia [1].

The effectiveness of a dopant in the reduction of thermal conductivity of zirconia is largely dependent on the valence of its metal cation. Subtetravalent oxides are the most effective dopants in decreasing the thermal conductivity because of the existence of oxygen vacancies, which are generated to compensate the charge missing caused by the

substitution of Zr^{4+} by the lower-valent dopant cations. The oxygen vacancies strongly scatter phonons and therefore significantly decrease the thermal conductivity. A good example is yttria-stablizied zirconia (YSZ), the most successfully developed TBCs material, which shows an almost temperature-independent low thermal conductivity due to the high concentration of oxygen vacancies [2-4]. In the case of tetravalent oxides, the substitution of Zr^{4+} by homovalent cations does not create any vacancy in zirconia lattice. The reduction of thermal conductivity is only attributed to the substitutional defects on the cation sites, which have been proven to be less effective than the oxygen vacancies in decreasing the thermal conductivity [1].

It can be expected that the thermal conductivity can be further decreased by doping subtetravalent and tetravalent oxides simultaneously into zirconia, utilizing the effects from both the vacancies on the anion sites and the substitutional defects on the cation sites. Several studies have reported the thermal conductivity of zirconia co-doped with yttria and some tetravalent oxides, i.e. titania, hafnia and ceria. For example, Miyazaki [5] studied the influence of titania on the thermal property of 3 mol% yttria partially stabilized zirconia (Y-PSZ) and found a continuous reduction of thermal conductivity from ~ 4.0 W/m·K for Y-PSZ to ~ 2.1 W/m·K for up to 20 mol% titania doped Y-PSZ. The author briefly discussed the above effect and also attributed the reduction of thermal conductivity to the mass disorder at the cation site generated by substitution of Zr^{4+} or Y^{3+} by Ti^{4+}. However, phase compositions of the solid solutions vary with titania concentration: from a mixture of monoclinic, cubic and tetragonal for low titania content (< 8.0 mol%), to a mixture of cubic and tetragonal for medium titania content (8 – 16 mol%) and to tetragonal for high titania content (~ 20 mol%). The effect of Ti^{4+} substitution at the cation site could be overshadowed by the effect caused by phase composition difference.

Unlike titania, which has a solution limit of 40 mol% with zirconia [6], hafnia has complete solubility with zirconia. Winter and Clarke [7] studied the yttria-stabilized zirconia-hafnia solid solutions over the whole composition range from YSZ to yttria-stabilized hafnia (YSH) at given yttria concentrations. They found a strong alloying effect that the solid solutions with the mixed zirconia-hafnia compositions having lower thermal conductivity than either YSZ or YSH, and the lowest thermal conductivity is

obtained in the composition of approximately equimolar zirconia and hafnia. Since the yttria concentration is high enough to stabilize all the compositions to the cubic phase, the reduction of thermal conductivity is attributed to mass disorder on the cation sublattice when Zr^{4+} is partially substituted by Hf^{4+} ions.

Similar to hafnia, ceria also has a complete solubility with zirconia. Since they are all tetravalent ions, it may be expected the substitution of Zr^{4+} by Ce^{4+} in YSZ has the same effect as the substitution of Zr^{4+} by Hf^{4+} on the thermal conductivity of YSZ. The composition dependence of thermal conductivity of the ceria-zirconia-yttria ternary solid solutions at given yttria concentration might have the same tendency as the hafnia-zirconia-yttria solid solutions. However, our previous work shows ceria-zirconia-yttria and hafnia-zirconia-yttria solid solutions have totally different composition dependence of electrical conductivity [8] because of the different nature between Hf^{4+} and Ce^{4+}, therefore it is of interest to investigate the thermal conductivity of the ceria-zirconia-yttria ternary solid solutions over the full composition range at given yttria concentration, which leads to further understanding on the role of homovalent substitution on the thermal conductivity of YSZ.

Several previous studies have shown that incorporation of ceria into YSZ also decreases the thermal conductivity. For example, Huang et al. [1] added 5 mol% ceria into 7 wt% YSZ and found the thermal conductivity was lowered from 3.99 W/m·K (for YSZ) to 3.23 W/m·K at room temperature, and from 3.96 W/m·K to 3.78 W/m·K at 600 ºC. However, the introduction of ceria significantly decreases the fraction of monoclinic phase in 7 wt% YSZ. Again the phase composition difference might be responsible for the reduction of thermal conductivity rather than the substitution of Zr^{4+} by Ce^{4+}.

Therefore in this chapter, a high concentration of yttria is used to ensure the non-existence of monoclinic phase in the solid solutions. Thermal conductivities of the zirconia-ceria-yttria solid solution, covering a full composition range from YSZ to yttria-doped ceria (YDC) at a given yttria concentration, were investigated. There is a striking difference between the temperature dependence of the thermal conductivities in ZrO_2-rich ($0 \leq x \leq 0.5$) region and those in CeO_2-rich region ($0.5 \leq x \leq 1.0$) of the ZrO_2-CeO_2-Y_2O_3 ternary solid solutions. In addition, the thermal conductivity is less

dependent on the composition in the in ZrO_2-rich ($0 \le x \le 0.5$) region, but it is strongly dependent on the composition in the CeO_2-rich region ($0.5 \le x \le 1.0$) of the ZrO_2-CeO_2-Y_2O_3 ternary solid solutions. The purpose of this paper is to further understanding on the influence of homovalent substitution, size and mass of dopants on the thermal conductivity of zirconia-based materials, in particular, the effect of oxygen vacancy disorder has been indentified as a possible major factor to affect thermal conductivity of the ZrO_2-CeO_2-Y_2O_3 ternary system.

6.2 Experiments

Procedures of sample preparation and general characterizations of the samples, e.g., XRD, SEM and densities, have been described in Chapter 5. Details of the thermal diffusivity measurement can be found in Chapter 4.

The specific heat capacitance values of the solid solutions at various temperatures were calculated according to the Neumann-Kopp rule [9] based on the reference specific heat values of ZrO_2, CeO_2 and Y_2O_3. The specific heat values of selected compositions at various temperatures are listed in Table 6.1.

Thermal conductivities of the solid solutions were obtained from the density (ρ), specific heat (C_p) and thermal diffusivity (α) using the relationship:

$$k = \rho \cdot C_p \cdot \alpha \ . \tag{6.1}$$

The thermal conductivities were corrected to fully-dense values (k_{dense}) using [13]

$$\frac{k}{k_{dense}} = 1 - \frac{4}{3}\Phi , \tag{6.2}$$

where Φ is the volume fraction of porosity.

Table 6.1 The specific heat capacities of ZrO_2, CeO_2, Y_2O_3 and the solid solutions at various temperatures.

Temperature (°C)	Specific heat capacity (J g^{-1} K^{-1})									
	ZrO_2 [10]	CeO_2 [11]	Y_2O_3 [12]	x in $[(ZrO_2)_{1-x}(CeO_2)_x]_{0.92}(Y_2O_3)_{0.08}$						
				0	0.1	0.3	0.5	0.7	0.8	1.0
100	0.506	0.381	0.485	0.503	0.489	0.462	0.439	0.418	0.409	0.375
200	0.543	0.403	0.511	0.539	0.522	0.463	0.467	0.444	0.434	0.401
300	0.565	0.419	0.528	0.560	0.543	0.512	0.486	0.462	0.450	0.417
400	0.581	0.431	0.541	0.575	0.558	0.527	0.499	0.474	0.463	0.429
500	0.593	0.441	0.552	0.588	0.570	0.538	0.510	0.485	0.474	0.438
600	0.603	0.451	0.562	0.598	0.580	0.548	0.520	0.495	0.483	0.445
700	0.612	0.459	0.571	0.607	0.589	0.557	0.529	0.504	0.492	0.452
800	0.621	0.468	0.580	0.615	0.597	0.565	0.537	0.512	0.501	0.458
900	0.628	0.476	0.588	0.623	0.605	0.573	0.545	0.520	0.509	0.464

6.3 Results

Figure 6.1 shows the thermal diffusivities of the solid solutions as a function of temperatures. For all the compositions, the thermal diffusivities decrease with increasing temperature. When $x < 0.5$, the thermal diffusivity for each composition has a low value and it is close to each other. On the contrary, when $x > 0.5$, the thermal diffusivity has a distinguishable dependence on the composition: it increases with an increase in x. In addition, the effect of temperature on thermal conductivity becomes more significant with increasing x. Since the influence of porosity is included, further discussion will eliminate the effect of porosity on thermal conductivity.

Figure 6.2 shows the thermal conductivities of the solid solutions at different temperatures. All the thermal conductivity values have been corrected to the fully-dense values according to Eq.(6.2). Two features are noticeable in Figure 6.2. First, the thermal conductivities of YSZ and YDC exhibit totally different temperature dependence: thermal conductivity of YSZ has an almost temperature-independent value within the temperature range, whereas the thermal conductivity of YDC shows an obvious decrease with an increase in the temperature. Second, when $x < 0.5$, the substitution of Zr^{4+} by Ce^{4+} only slightly decreases the thermal conductivity of YSZ, and the thermal conductivities of the solid solutions are almost temperature-independent; whereas when $x > 0.5$, the substitution of Ce^{4+} by Zr^{4+} significantly decreases the thermal conductivity of YDC, and the thermal conductivities of the solid solutions all decrease with an increase in the temperature.

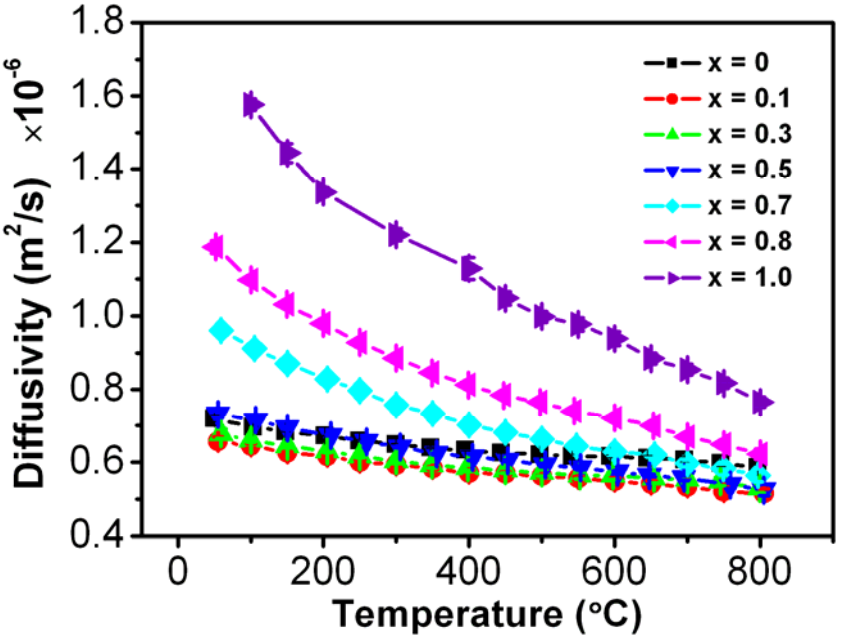

Figure 6.1 Thermal diffusivities of the of the $[(ZrO_2)_{1-x}(CeO_2)_x]_{0.92}(Y_2O_3)_{0.08}$ ($0 \leq x \leq 1$) solid solutions at different temperatures. The error bar for each sample and each temperature is quite small to be seen clearly.

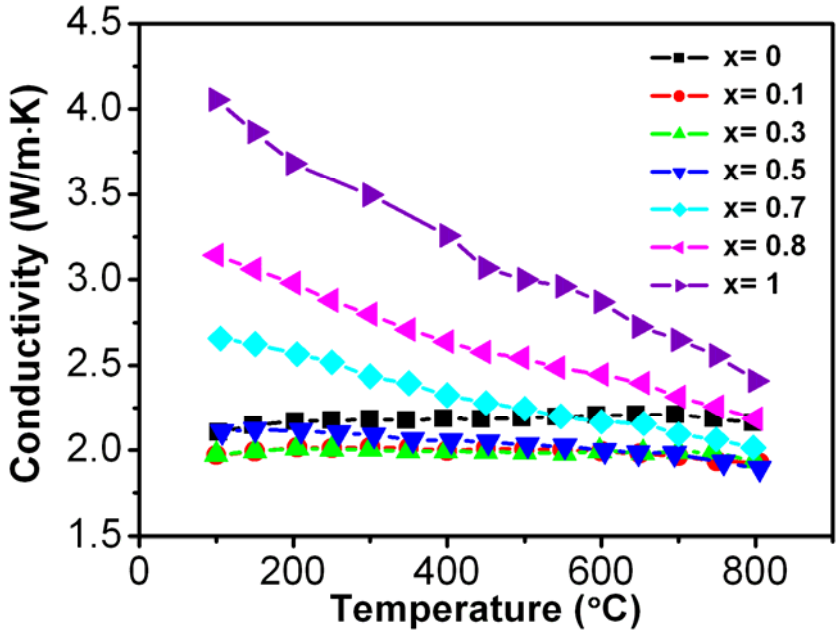

Figure 6.2 Thermal conductivities after zero-porosity correction of the $[(ZrO_2)_{1-x}(CeO_2)_x]_{0.92}(Y_2O_3)_{0.08}$ ($0 \leq x \leq 1$) solid solutions at different temperatures.

In Figure 6.3 the thermal conductivities of the solid solutions were plotted as a function of the composition (x). The thermal conductivities of the solid solutions vary nonlinearly with the composition, and they are lower than the values calculated from the rule of mixture, as suggested by the dash dot line. The solid solutions in the ZrO_2-rich region ($x < 0.5$) have lower thermal conductivities and show less temperature or composition dependence than those in the CeO_2-rich region ($x > 0.5$).

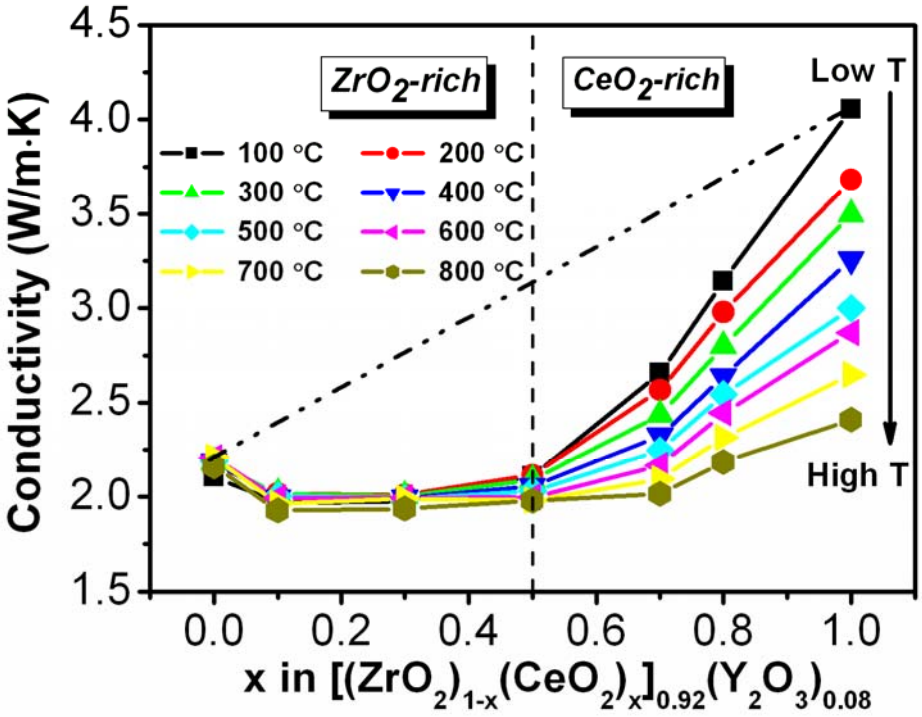

Figure 6.3 Thermal conductivities of the $[(ZrO_2)_{1-x}(CeO_2)_x]_{0.92}(Y_2O_3)_{0.08}$ ($0 \le x \le 1$) solid solutions as a function of the composition (x) at different temperatures.

6.4 Discussion

The major findings of this work are: (1) the striking difference between the temperature dependence of the thermal conductivities in ZrO_2-rich ($0 \le x \le 0.5$) region and those in CeO_2-rich region ($0.5 \le x \le 1.0$) of the ZrO_2-CeO_2-Y_2O_3 ternary solid solutions. This is quite different from the ZrO_2-HfO_2-Y_2O_3 solid solutions, in which no temperature dependence has been observed for the thermal conductivities over the entire composition range [7]; (2) the thermal conductivity is less dependent on the composition in the in ZrO_2-rich ($0 \le x \le 0.5$) region, but it is strongly dependent on the

composition in the CeO_2-rich region ($0.5 \leq x \leq 1.0$) of the ZrO_2-CeO_2-Y_2O_3 ternary solid solutions.

Therefore the main purpose of this session is to discuss the temperature dependence and the composition dependence of the thermal conductivity in the ZrO_2-CeO_2-Y_2O_3 solid solutions. In part 6.4.1, we discuss why the system exhibits totally different temperature dependence of the thermal conductivity with different composition, starting from the **binary** systems YSZ and YDC, in comparison with YSH studied previously. Then in part 6.4.2, the temperature dependence of the thermal conductivity of the ZrO_2-CeO_2-Y_2O_3 solid solutions is further discussed based on the understanding of the binary systems. Finally in part 6.4.3, discussion on the composition dependence of the thermal conductivity is carried out.

6.4.1 Temperature dependence of thermal conductivity in YSZ and YDC

In this work, YSZ and YDC have the same fluorite structure with the same concentration of oxygen vacancy, however their thermal conductivities exhibit totally different temperature dependence: k_{YSZ} is almost temperature independent, whereas k_{YDC} decreases monotonously with increasing temperature. Yttria-stablised Hafnia (YSH) with the same fluorite structure has been reported a temperature independent thermal conductivity. Why YDC behaves differently from YSZ and YSH is the first issue to be discussed. Because of the large grain sizes (~ 10 μm) in all the samples, the grain boundary effect is negligible in the following discussions.

(1) phonon-phonon and phonon-defect scattering

It is well known that in a ceramic material with point defects, the phonon mean free path $\Lambda(\omega)$ consists of two independent components and it can be written as [14]:

$$\frac{1}{\Lambda(\omega)} = \frac{1}{\Lambda_U(\omega)} + \frac{1}{\Lambda_D(\omega)}, \tag{6.3}$$

Where $\Lambda_U(\omega)$ is the mean free path due to Umklapp phonon-phonon scattering and $\Lambda_D(\omega)$ is the mean free path from the phonon-defect scattering. $\Lambda_U(\omega)$ is temperature dependent, as described by [14]:

$$\frac{1}{\Lambda_U(\omega)} = \frac{\omega^2 T}{D_U}, \tag{6.4}$$

whereas $\Lambda_D(\omega)$ is temperature independent, and it is determined by the defect concentration (c_D) by [14]:

$$\frac{1}{\Lambda_D(\omega)} = \frac{\omega^4 c_D}{D_D}, \tag{6.5}$$

where D_U and D_D are temperature and frequency-independent parameters characterizing the Umklapp process and the phonon-defect collision respectively. Therefore, when the phonon-phonon scattering (Umklapp process) dominates, the thermal conductivity decreases with increasing temperature. On the contrary, when the phonon-defect scattering dominates, the thermal conductivity is temperature-independent. In the following part, the parameters for phonon-phonon and phonon-scattering processes of YSZ, YDC and YSH are calculated and compared.

(a) Umklapp phonon-phonon process

The parameter D_U can be evaluated by the following expression [15, 16]:

$$D_U = \frac{\sqrt{2}}{4\pi}\left(\frac{v^2}{a}\right)\left(\frac{\overline{M}v^2}{\gamma^2 k_B}\right), \tag{6.6}$$

in which a^3 is the mean atomic volume, $\overline{M}$ is the mean atomic mass, γ is the Grüneisen constant and v is the averaged sound velocity which has a relationship with the Debye frequency by [16]:

$$v = a\omega_D(6\pi^2)^{-1/3}. \tag{6.7}$$

Combine Eq.(6.6) and (6.7), D_U is rewritten as:

$$D_U = \frac{\sqrt{2}}{4\pi}\left(\frac{\overline{M}a^3\omega_D^4(6\pi^2)^{-\frac{4}{3}}}{\gamma^2 k_B}\right). \tag{6.8}$$

The parameters used in Eq.(6.8) of pure zirconia, ceria and hafnia are listed in Table 6.2. Despite of the scattering reference values of Θ_D and γ, the calculated D_U of zirconia, ceria and hafnia are still within the same order of magnitude, indicating the contribution from phonon-phonon scattering to the thermal conductivity of ZrO_2, CeO_2 and HfO_2 is similar. This is in consistence with the theoretical prediction of the minimum thermal conductivities of these three oxides, which have close values with each other [17].

Table 6.2 The parameters used in Eq.(6.8) and the calculated D_U values of ZrO_2, CeO_2 and HfO_2.

	$\overline{M}$ (kg)	a (nm)	Θ_D (K)	ω_D (Hz)	γ	D_U (SI)
ZrO_2	0.685×10^{-25}	0.225	590 [18] 575 [19] 533 [20] 510 [21] 470 [22]	$(7.00 \pm 0.64)\times10^{13}$	1.4 [23]	$(3.73 \pm 1.3)\times10^{20}$
CeO_2	0.956×10^{-25}	0.236	503 [24] 480 [25] 350 [26]	$(5.62 \pm 0.91)\times10^{13}$	1.24 [27] 1.44 [28]	$(3.18 \pm 1.85)\times10^{20}$
HfO_2	1.181×10^{-25}	0.223	603 [29] 576 [30] 471 [30] 440 [30] 483 [29]	$(6.73 \pm 0.93)\times10^{13}$	1.4	$(5.29 \pm 2.88)\times10^{20}$

(b) Phonon-defect scattering

The parameter describing the phonon-defect scattering D_D, is expressed as [31]:

$$D_D = \frac{4\pi m v^4}{\Gamma \Omega_0}, \tag{6.9}$$

in which Ω_0 is the volume of the unit cell, m is the number of atoms; Γ is a scattering coefficient, which is determined by the mass difference between the substitutional atom and the host atom, in the form of $\Gamma = \left(\frac{\Delta M}{M}\right)^2$. The sound velocity v is related to the elastic modulus (E) and the density (ρ) by $v = 0.87\sqrt{\frac{E}{\rho}}$ [32]. Therefore Eq.(6.9) is rewritten as:

$$D_D = \frac{4\pi m v^4}{\Gamma \Omega_0} = \frac{4(0.87)^4 \pi m}{\Gamma \Omega_0}\left(\frac{E}{\rho}\right)^2. \tag{6.10}$$

In YSZ and YDC, there are two types of point defects. One is is the substitutional defect caused by the replacement of Zr^{4+} or Ce^{4+} by Y^{3+} at the cation site, and the other one is the oxygen vacancies generated to keep the electroneutrality. According to the defect reaction $Y_2O_3 \xrightarrow{MO_2} 2Y_M^{'} + V_O^{\bullet\bullet} + 3O_O^x$, adding b mol Y_2O_3 into MO_2 can generate $2b$ mol $Y_M^{'}$ and b mol $V_O^{\bullet\bullet}$. Thus the total defect concentration ($c_D = c_{DY} + c_{DO}$) is $3b$ mol.

Therefore, the scattering coefficient is composed of tow parts corresponding to the two types of point defects, in the form of [33]:

$$\Gamma = \frac{c_Y}{c_D}\left(\frac{\Delta M_{cation}}{\overline{M}}\right)^2_{cation} + \frac{c_V}{c_D}\left(\frac{\Delta M_{O-V}}{\overline{M}}\right)^2_{O-V} = \frac{2}{3}\left(\frac{\Delta M_{cation}}{\overline{M}}\right)^2_{cation} + \frac{1}{3}\left(\frac{\Delta M_{O-V}}{\overline{M}}\right)^2_{O-V}, \quad (6.11)$$

where $\overline{M}$ is the average atomic weight in a unit cell. For oxygen vacancies, the effective value of $\frac{\Delta M_{O-V}}{\overline{M}} = -\frac{M_O}{\overline{M}} - 2$, in which the term -2 arises because the number of broken bonds at the vacancy is twice the number of bonds per atom [31].

The parameters used for calculating D_D for YSZ, YDC and YSH, along with the calculated Γ and D_D are listed in Table 6.3. Although the calculated D_D value of YDC is the lowest, considering the scattered reference values for the Young's modulus, the D_D values are quite close for these three materials.

Comparing the D_U and D_D values of YSZ, YDC and YSH in Table 6.2 and 6.3, it can be seen that the calculated D_U and D_D values of YDC are not significantly different from those of YSZ and YSH, indicating the contributions from the phonon-phonon scattering and the phonon-defect scattering are similar in the three materials, which fails to explain the strikingly different thermal conductivity-temperature relationship of YDC compared with that of YSZ and YSH. On the other hand, this also indicates the existence of oxygen vacancies in YSZ and YSH is not the decisive factor that causes the temperature independent thermal conductivity.

Table 6.3 Parameters used in Eq.(6.10) and (6.11) and the calculated D_D values for YSZ, YDC and YSH.

	E (GPa)	ρ (Kg/m^3)	Ω_0/m (m^3)	$\overline{M}$ (g/mol)	ΔM_{cation} (g/mol)	$\Delta M_{O\text{-}V}$ (g/mol)	$\left(\frac{\Delta M_{cation}}{\overline{M}}\right)^2$	$\left(\frac{\Delta M_{O-V}}{\overline{M}}\right)^2$	Γ	D_D
YSZ	220 [34]	5.96×10^{3}	1.14×10^{-29}	41.59	2.32	99.18	3.11×10^{-3}	5.69	1.90	4.53×10^{44}
YDC	130 [35,36]	6.85×10^{3}	1.31×10^{-29}	55.83	51.22	127.66	0.84	5.23	2.30	8.60×10^{43}
YSH	240 [37]	9.50×10^{3} [7]	1.11×10^{-29}	67.00	89.59	150.00	1.79	5.01	2.86	1.45×10^{44}

(2) Ordering of defects

In a defect fluorite structure the oxygen vacancies are disordered (unlike the ordered vacancies in a pyrochlore structure). However the extent of the disordering is determined by the relative size of the dopant and the host cations. At low/medium dopant concentrations, when the ionic radius of the dopant cation is larger than that of the host cation, the oxygen vacancies are statistically distributed; on the contrary, when the dopant and the host cations have the similar radii, the long-range superstructures (ordered vacancies) are generated [38]. The ionic radii of Zr^{4+}, Hf^{4+}, Ce^{4+} and Y^{3+} are 0.084 [7], 0.083 [7], 0.097 [39] and 0.102 nm [7], respectively. In YSZ or YSH, the dopant cation (Y^{3+}) is much larger than the host cation (Zr^{4+} or Hf^{4+}), whereas in YDC the dopant and the host cations are of the similar size. Therefore at given yttria concentration, the oxygen vacancies in YDC are less disordered than those in YSZ or YSH.

An evidence for the above statement is from the nuclear magnetic resonance (NMR) spectroscopy studies on the structural disorder in YSZ and YDC [40]. The average coordination numbers of Y, Zr and Ce in YSZ and YDC obtained from the NMR spectra all deviate from their "ideal" values (which correspond to a random distribution of vacancies without any preference for any particular cation [40,41]), indicating the existence of oxygen vacancy ordering in both YSZ and YDC. In YSZ, the oxygen vacancies prefer to be associated with Zr atoms; on the contrary, in YDC the oxygen vacancies prefer to be associated with Y atoms. Also the extent of the oxygen vacancy ordering is obviously different between YSZ and YDC. At a given Y concentration (15 mol% for example), if oxygen vacancies are randomly distributed (totally disordered), the ideal coordination number $C_{ideal} = 8 - 2\times0.15 = 7.7$ [40]. The average coordination number of Zr (C_{Zr}) obtained from NMR spectroscopy of YSZ is 7.65, which is only slightly lower than C_{ideal}; however, C_Y in YDC is 7.13, which is much lower than C_{ideal}. The results indicate that at the yttria concentration in this study, the defect ordering is more severely in YDC than in YSZ. In other words, the oxygen vacancies are mostly disordered (randomly distributed) in YSZ but they are ordered to some extent in YDC.

The disordered defects are more effective at scattering phonons than the ordered ones and therefore cause the temperature independent thermal conductivity of YSZ. On the

contrary, the ordering of oxygen vacancies causes the YDC behaves like a typical crystal with point defect scattering. In other words, the defect disorder/ordering may be the decisive factor that determines the temperature dependence of thermal conductivity of YSZ and YDC.

6.4.2 Temperature dependence of thermal conductivity in ZrO_2-CeO_2-Y_2O_3 ternary solid solutions

Based on the understanding of temperature dependence of thermal conductivity of YSZ and YDC, further discussions are carried out on the ZrO_2-CeO_2-Y_2O_3 ternary solid solutions. From Figure 6.2 and 6.3, it can be seen that the thermal conductivities show totally different temperature dependences in the ZrO_2-rich region ($0 \leq x < 0.5$) and in the CeO_2-rich region ($0.5 < x \leq 1.0$). Since the intermixing of Zr^{4+} and Ce^{4+} does not create any oxygen vacancy, the concentration of oxygen vacancies remains constant within the whole composition range of the ternary solid solutions. And according to the conclusion in part 6.4.1, the temperature dependence of thermal conductivity is mainly dominated by the disorder/ordering of oxygen vacancies. Therefore in this part we will focus on the oxygen vacancy ordering in the ZrO_2-CeO_2-Y_2O_3 system to discuss the temperature dependence of thermal conductivity.

The work by Chen *et al.* has pointed out the Zr^{4+} has the ability to attract oxygen vacancies in the YSZ-YDC ternary solid solutions [42]. Therefore in the CeO_2-rich region ($0.5 < x \leq 1.0$), when ZrO_2 is doped into YDC, the Zr^{4+} traps the oxygen vacancies from the nearest neighbouring sites of Y^{3+} to the nearest neighbouring sites of Zr^{4+} and "releases" the ordered oxygen vacancies in YDC. The more ZrO_2 is doped, the more ordered oxygen vacancies are released from YDC. In other words, the undersized Zr^{4+} causes the redistribution of oxygen vacancies, which gradually change from the ordered ones in YDC to the disordered ones in the ternary solid solutions. Consequently the thermal conductivities of the solid solutions show less temperature dependence with an increase in the ZrO_2 concentration in the CeO_2-rich region.

However, in the ZrO_2-rich region ($0 \leq x < 0.5$), when CeO_2 is doped into YSZ, the oxygen vacancies are not redistributed due to the large ionic size of Ce^{4+}. NMR study [43] reveals that when CeO_2 is doped into YSZ, the oxygen vacancies are still located at the nearest neighbouring sites of Zr^{4+} (or Ce^{4+}). The average coordination number of the tetravalent cations remains nearly constant with an increase of the CeO_2 concentration and it is close to the ideal coordination number corresponding to a random distribution of oxygen vacancies. Therefore, in the ZrO_2-rich region, the oxygen vacancies are randomly distributed around the Zr^{4+} or Ce^{4+} ions, which is similar to the oxygen vacancy distribution in YSZ. Consequently the thermal conductivities of the solid solutions in this region have similar temperature dependence with YSZ.

To sum up, the different temperature dependence of the thermal conductivity in ZrO_2-rich region and in CeO_2-rich region is attributed to the significantly different ionic size between Zr^{4+} and Ce^{4+}, which causes different oxygen vacancy distribution in the two regions.

6.4.3 Composition dependence of thermal conductivity in ZrO_2-CeO_2-Y_2O_3 ternary solid solutions

As illustrated in Figure 6.2 and 6.3, the composition dependence of the thermal conductivity of the solid solutions could also be divided into two regions. In the ZrO_2-rich region where $x < 0.5$, substitution of Zr^{4+} by Ce^{4+} has marginal effect in decreasing the thermal conductivity of YSZ. On the contrary, in the CeO_2-rich region where $x > 0.5$, substitution of Ce^{4+} by Zr^{4+} significantly decreases the thermal conductivity of YDC.

In the ZrO_2-CeO_2-Y_2O_3 ternary solid solutions, similar as in the binary systems, the phonons are scattered both from the cation site (Zr, Ce, Y) and the anion site (O and oxygen vacancy $V_O^{\bullet\bullet}$). The scattering coefficient of the ternary solid solution is also determined from Eq.(6.11). However, in the case of ternary solid solutions, there are three types of atoms on the cation sites. The scattering coefficient of the cation site is expressed as [44, 45]:

$$\Gamma_{(Zr,Ce,Y)} = \Gamma_Y + \Gamma_{Zr} + \Gamma_{Ce}$$
$$= \left(\frac{M_{(Zr,Ce,Y)}}{\overline{M}}\right)^2 \left[0.148\left(\frac{M_Y - M_{(Zr,Ce,Y)}}{M_{(Zr,Ce,Y)}}\right)^2 + 0.852(1-x)\left(\frac{M_{Zr} - M_{(Zr,Ce,Y)}}{M_{(Zr,Ce,Y)}}\right)^2 + 0.852x\left(\frac{M_{Ce} - M_{(Zr,Ce,Y)}}{M_{(Zr,Ce,Y)}}\right)^2\right]. \quad (6.12)$$

where $M_{(Zr,Ce,Y)}$ is the average mass of the cation site and $\overline{M}$ is the average mass of $(Zr_{1-x}Ce_x)_{0.852}Y_{0.148}O_{1.926}$.

In Figure 6.4, the scattering coefficient of each scattering site has been plotted as a function of x. The scattering coefficient of the cation site increases with an increase of x, reaching its highest value when Zr and Ce are around equal molar ($x \approx 0.5$), and decreases with further increase of x. At the anion site, the scattering coefficient slightly decreases due to the increase of average mass of the solid solution. The overall scattering coefficient calculated from Eq.(6.11) has the same trend with that of the cation site $\Gamma_{(Zr,Ce,Y)}$. Because the thermal conductivity $k = \propto \left(\frac{\Omega_0 \Gamma}{v^4}\right)^{-1}$, it is expected that the thermal conductivity has a V-shape variation as a function of x. This is generally in agreement with the experimental observations as shown in Figure 6.3. Specifically it accords with the experimental results in the CeO_2-rich region, but shows deviation in the ZrO_2-rich region, where thermal conductivity has little composition dependence.

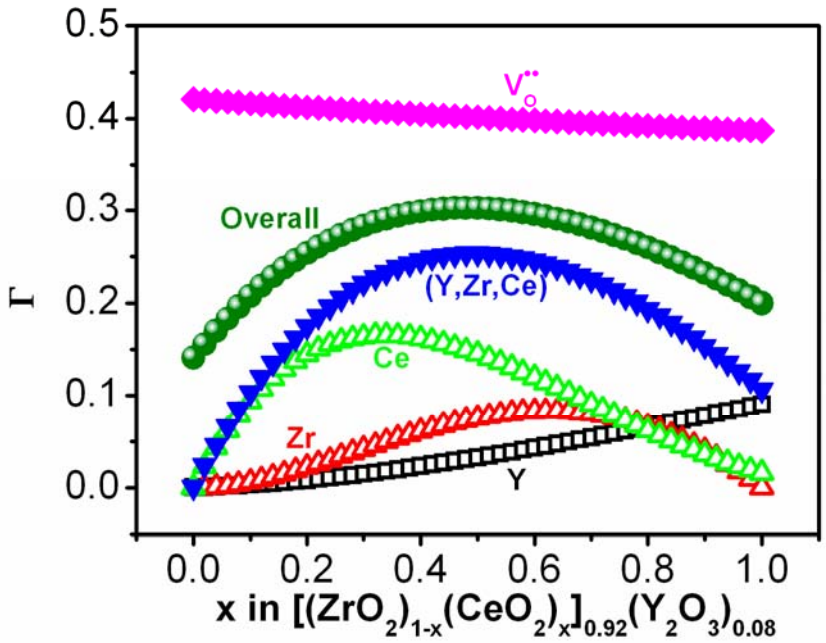

Figure 6.4 Scattering coefficient Γ as a function of the composition x at constant yttria concentration.

The possible reason for the deviation in the ZrO_2-rich region is that the contribution from the ionic size difference between Zr^{4+} and Y^{3+}, which causes the lattice strain, is not considered when calculating the scattering coefficient. The ionic size difference decreases with an increase in the CeO_2 concentration because of the similar size between Y^{3+} and Ce^{4+}. It can be predicted that the scattering coefficient caused by the ionic size difference monotonously decreases with *x*. This part of contribution smoothes the sharp increase of $\Gamma_{(Zr,Ce,Y)}$ in the ZrO_2-rich region and consequently causes the composition independent thermal conductivity in the ZrO_2-rich region.

6.4.4 Comparison with the ZrO_2-HfO_2-Y_2O_3 solid solutions

Now we briefly compare the thermal conductivities of zirconia-ceria-yttria with the reported zirconia-hafnia-yttria solid solutions. One common feature exists in these two series of solid solutions that the intermixing of Zr^{4+} with either Hf^{4+} or Ce^{4+} can decrease the thermal conductivity of YSZ, YSH and YDC, indicating the effectiveness of mass disorder at the cation site in scattering phonons.

A striking difference between these two series is that the zirconia-hafnia-yttria series has almost temperature independent thermal conductivity within the whole temperature range; however, the zirconia-ceria-yttria series has clear temperature dependence in the CeO_2-rich region. Because of the significantly larger ionic size of Y^{3+} than that of Zr^{4+} and Hf^{4+}, the oxygen vacancies are randomly distributed (disordered) in the solid solutions, which causes the temperature independent thermal conductivity; on the contrary, the similar ionic size of Y^{3+} and Ce^{4+} causes a long range ordering of oxygen vacancies, which leads to a typical temperature dependence of crystal with point defects.

The comparison between these two series of ternary solid solutions indicates the both the atomic mass and the ionic size of the tetravalent cations are important factors that influence the thermal conductivity of the solid solutions.

6.5 Conclusions

Thermal conductivities of $[(ZrO_2)_{1-x}(CeO_2)_x]_{0.92}(Y_2O_3)_{0.08}$ ($0 \leq x \leq 1$) solid solutions were investigated in this study. The main conclusions are:

(1) The incorporation of ZrO_2 and CeO_2 in the solid solutions decreases the thermal conductivity compared with their end members (YSZ and YDC). The lowest thermal conductivity is obtained at the compositions of x = 0.3~ 0.5, which is around 10% lower than YSZ and 33% lower than YDC at 500 ºC.

(2) The thermal conductivities of the solid solutions in ZrO_2-rich region are almost temperature-independent, and show marginal composition dependence. On the contrary, the thermal conductivities of the solid solutions in CeO_2-rich region decrease with increasing temperature, and show significant composition dependence.

(3) The reduction of thermal conductivity due to doping should be mainly caused by the mass disorder at the cation site; the different temperature dependence of thermal conductivity may be due to the significant different ionic size between Zr^{4+} and Y^{3+} which leads to highly disordered oxygen vacancies, whereas the similar ionic size between Ce^{4+} and Y^{3+} which leads to a long range ordering of oxygen vacancies.

(4) A comparison with the ZrO_2-HfO_2-Y_2O_3 series indicates that both the atomic mass and the ionic size of the tetravalent cations are important factors that influence the temperature and composition dependence of thermal conductivity in the ternary solid solutions.

Reference

[1] X. Huang, D. Wang, M. Lamontagne and C. Moreau, *Experimental study of the thermal conductivity of metal oxides co-doped yttria stabilized zirconia*, Materials Science and Engineering B **149** (2008) 63-72.

[2] D. R. Clarke and S. R. Phillpot, *Thermal barrier coating materials*, Materials Today **8** (2005) 22-29.

[3] X. Q. Cao, R. Vassen and D. Stoever, *Ceramic materials for thermal barrier coatings*, Journal of the European Ceramic Society **24** (2004) 1-10.

[4] N. P. Padture, M. Gell and E. H. Jordan, *Thermal barrier coatings for gas-turbine engine applications*, Science **296** (2002) 280-284.

[5] H. Miyazaki, *Influence of TiO_2 solid solution on the thermal property and ionic conductivity of partially stabilized zirconia*, International Journal of Applied Ceramic Technology **5** (2008) 490-498.

[6] F. H. Brown and P. Duwez, *The zirconia-titania system*, Journal of the American Ceramic Society **37** (1954) 129-132.

[7] M. R. Winter and D. R. Clarke, *Thermal conductivity of yttria-stabilized zirconia-hafnia solid solutions*, Acta Materialia **54** (2006) 5051-5059.

[8] F. Yang, X. Zhao and P. Xiao, *Bulk conduction and relaxation in $[(ZrO_2)_{1-x}(CeO_2)_x]_{0.92}(Y_2O_3)_{0.08}$ ($0 \leq x \leq 1$) solid solutions at intermediate temperatures*, Journal of Power Sources **196** (2011) 4943-4949.

[9] H. Kopp, *Investigations of the specific heat of solid bodies*, Philosophical Transactions of the Royal Society London **155** (1865) 71-202.

[10] J. P. Coughlin and E. G. King, *High-temperature heat contents of some zirconium-containing substances*, Journal of the American Chemistry Society **72** (1950) 2262-2265.

[11] V. Viswanathan, R. Filmalter, S. Patil, A. Deshpande and S. Seal, *High-temperature oxidation behavior of solution precursor plasma sprayed nanoceria coating on martensitic steels*, Journal of the American Ceramic Society **90** (2007) 870-877.

[12] Y. A. Landa, Y. A. Polonskii, B. S. Glazachev, and T. V. Milovidova, *The enthalpy and specific heat of yttrium oxide at 1300 -2100 ºK*, Refractories and Industrial Ceramics **15** (1974) 86-88.

[13] C. Wan, W. Zhang, Y. Wang, Z. Qu, A. Du, R. Wu and W. Pan, *Glass-like thermal conductivity in ytterbium-doped lanthanum zirconate pyrochlore*, Acta Materialia **58** (2010) 6166-6172.

[14] R. Mevrel, J. C. Laizet, A. Azzopardi, B. Leclercq, M. Poulain, O. Lavigne and D. Demange, *Thermal diffusivity and conductivity of $Zr_{1-x}Y_xO_{2-x/2}$ (x = 0, 0.084 and 0.179) single crystals*, Journal of the European Ceramic Society **24** (2004) 3081-3089.

[15] M. Roufosse and P. G. Klemens, *Thermal conductivity of complex dielectric crystals*, Physical Review B **7** (1973) 5379-5386.

[16] J. F. Bisson and D. Fournier, *Thermal conductivity of yttria-zirconia single crystals, determind with spatially resolved infrared thermography*, Journal of the American Ceramic Society **83** (2000) 1993-1998.

[17] C. G. Levi, *Emerging materials and processes for thermal barrier systems*, Current Opinion in Solid State and Materials Science **8** (2004) 77-91.

[18] C. Degueldre, P. Tissot, H. Lartigue and M. Pouchon, *Specific heat capacity and Debye temperature of zirconia and its solid solution*, Thermochimica Acta **403** (2002) 267-273.

[19] M. V. Nevitt, Y. Fang and S. Chan, *Heat capacity of monoclinic zirconia between 2.75 and 350 K*, Journal of the American Ceramic Society **73** (1990) 2502-2504.

[20] D. N. Argyriou, *Measurement of the static disorder contribution to the temperature factor in cubic stabilized ZrO_2*, Journal of Applied Crystallography **27** (1994) 155-158.

[21] T. Shirakami, T. Tojo, T. Atake, T. Mori and H. Yamamura, *Low temperature heat capacities of zirconia and yttria-doped zirconia $(ZrO_2)_{1-x}(Y_2O_3)_x$ (x = 0, 0.0200, 0.00396*), Thermochimica Acta **267** (1995) 415-420.

[22] W. N. Lawless, *Low-temperature specific heat of a ZrO_2: Y_2O_3 oxygen conductor*, Physical Review B **21** (1980) 585-588.

[23] E. Kisi and M. Yuxiang, *Debye temperature, anharmonic thermal motion and oxygen non-stoichiometry in yttria stabilized cubic zirconia*, Journal of physics:

Condensed Matter **10** (1998) 3823-3832.

[24] L. Sun, Y. Cheng and G. Ji, *Elastic and optical properties of CeO_2 via first-principles calculations*, Journal of Atomic and Molecular Sciences **1** (2010) 143-151.

[25] T. Hisashige, Y. Yamamura and T. Tsuji, *Thermal expansion and Debye temperature of rare earth-doped ceria*, Journal of Alloys and Compounds **408-412** (2006) 1153-1156.

[26] V. Kanchana, G. Vaitheeswaran, A. Svane and A. Delin, *First-principles study of elastic properties of CeO_2, ThO_2 and PoO_2*, Journal of Physics: Condensed Matter **18** (2006) 9615-9624.

[27] J. R. McBride, K. C. Hass, B. D. Poindexter and W. H. Weber, *Raman and x-ray studies of $Ce_{1-x}RE_xO_{2-y}$, where RE= La, Pr, Nd, Eu, Gd, and Tb*, Journal of Applied Physics **76** (1994) 2435-2441.

[28] A. S. Lermontov, V. K. Ivanov, M. S. Yakimova, A. E. Baranchikov, O. S. Polezhaeva and Y. D. Tret'yakov, *Size effect in CO Oxidation on CeO_{2-x} nanoparticles*, Doklady Chemistry **430** (2010) 4-7.

[29] M. A. Caravaca, J. C. Mino, V. J. Perez, R. A. Casali and C. A. Ponce, *Ab initio study of the elastic properties of single and polycrystal TiO_2, ZrO_2 and HfO_2 in the cotunnite structure*, Journal of Physics: Condensed Matter **21** (2009) 015501.

[30] C. A. Ponce, R. A. Casali and M. A. Caravaca, *Ab initio study of mechanical and thermo-acoustic properties of tough ceramics: applications to HfO_2 in its cubic and orthorhombic phase*, Journal of Physics: Condensed Matter **20** (2008) 045213.

[31] P. G. Klemens, *The scattering of low-frequency lattice waves by static imperfections*, Proceedings of the Physical Society of London Section A **68** (1955) 1113-1128.

[32] D. R. Clarke, *Materials selection guidelines for low thermal conductivity thermal barrier coatings*, Surface Coatings and Technology **163-164** (2003) 67-74.

[33] J. Wu, N. P. Padture, P. G. Klemens, M. Gell, E. Garcia, P. Miranzo and M. I. Osendi, *Thermal conductivity of ceramics in the ZrO_2-$GdO_{1.5}$ system*, Journal of Materials Research **17** (2002) 3193-3200.

[34] S. Giraud and J. Canel, *Young's modulus of some SOFCs materials as a function of*

temperature, Journal of the European Ceramic Society **28** (2008) 77-83.

[35] K. Sato, H. Yugami and T. Hashida, *Effect of rare-earth oxides on fracture properties of ceria ceramics*, Journal of Materials Science **39** (2004) 5765-5770.

[36] E. Wachtel and I. Lubomirsky, *The elastic modulus of pure and doped ceria*, doi: 10.1016/j.scriptamat.2010.09.021

[37] J. Wang, H. P. Li and R. Stevens, *Review: Hafnia and hafnia-toughened ceramics*, Journal of Materials Science **27** (1992) 5397-5430.

[38] F. Frey, H. Boysen and I. Kaiser-Bischoff, *Diffuse scattering and disorder in zirconia*, Zeitschrift fur Kristallographie **220** (2005) 1017-1026.

[39] R. D. Shannon and C. T. Prewitt, *Effective ionic radii in oxides and fluorides*, Acta Crystallographica Section B **25** (1969) 925-946.

[40] P. Jain, H. J. Avila-Paredes, C. Gapuz, S. Sen and S. Kim, *High-resolution ^{89}Y and ^{45}Sc spectroscopic study of short-range structural order in nanocrystalline Y- and Sc-doped CeO_2 and ZrO_2*, Journal of Physical Chemistry C **113** (2009) 6553-6560.

[41] K. Kawata, H. Maekawa, T. Nemoto and T. Yamamura, *Local structure analysis of YSZ by Y-89 MAS-NMR*, Solid State Ionics **177** (2006) 1687-1690.

[42] W. Chen, A. Navrotsky, Y. P. Xiong and H. Yokokawa, *Energetics of cerium-zirconium substitution in the $xCe_{0.8}Y_{0.2}O_{1.9}$-$(1-x)Zr_{0.8}Y_{0.2}O_{1.9}$ system*, Journal of the American Ceramic Society **90** (2007) 584-589.

[43] H. Maekawa, K. Kawata, Y. P. Xiong, N. Sakai and H. Yokokawa, *Quantification of local oxygen defects around yttrium ions for yttria-doped ceria-zirconia ternary system*, Solid State Ionics **180** (2009) 314-319.

[44] B. Abeles, *Lattice thermal conductivity of disordered semiconductor alloys at high temperatures*, Physical Review **131** (1963) 1906-1911.

[45] C. L. Wan, W. Pan, Q. Xu, Y. X. Qin, J. D. Wang , Z. X. Qu and M. H. Fang, *Effect of point defects on the thermal transport properties of $(La_xGd_{1-x})_2Zr_2O_7$: Experiment and theoretical model*, Physical Review B **74** (2006) 144109.

Chapter 7

Conclusions and future work

7.1 Conclusions

The electrical and thermal properties of YSZ/Al_2O_3 composites and ZrO_2-CeO_2-Y_2O_3 solid solutions are investigated in this thesis. The main conclusions are:

(1) The electrical conductivity of the YSZ/Al_2O_3 composite shows the typical characteristics expected from the percolation theory, with a critical YSZ volume fraction of 13.9 ± 0.4 % for the onset of conduction. Above this YSZ volume fraction, the activation energy has a similar value with pure YSZ and it is independent on the Al_2O_3 fraction because the electrical (ionic) conduction is mainly dominated by the YSZ phase.

(2) The information of the YSZ/Al_2O_3 interface can be obtained indirectly from the low frequency response on the impedance spectroscopy. The electrical conductivity of the YSZ/Al_2O_3 interface is higher than YSZ grain boundary but similar to, or lower than the YSZ grain.

(3) The thermal conductivity of the composites increases with an increase in the Al_2O_3 volume fraction, and it can be fitted well by the Maxwell theoretical model. The consistency of the thermal conductivity of the composite with the predicted values indicates the absence of interfacial thermal resistance in the composite.

(4) The absence of a Kapitza resistance of the YSZ/Al_2O_3 interface is due to the "clean" and coherent nature of the YSZ/Al_2O_3 interface, together with the small difference between the elastic properties of YSZ and Al_2O_3.

(5) The electrical conductivity of ZrO_2-CeO_2-Y_2O_3 ternary solid solutions has a "V-shape" variation as a function of the composition: it decreases with an increase of the mole ratio of CeO_2 (x), reaching the lowest value when x = 0.5 (Zr/Ce = 1), and then goes up with further increase of x. The ionic radius of the tetravalent dopant determines the composition dependence of the ionic conductivity of the solid solutions. When doping YSZ with other tetravalent dopant with similar ionic radius with Zr^{4+}, e.g., Hf^{4+}, such "V-shape" composition dependence of the bulk conductivity can not be observed.

(6) The incorporation of ZrO_2 and CeO_2 in the solid solutions decreases the thermal conductivity compared with their end members (YSZ and YDC), which is mainly due to the mass disorder at the cation site.

(7) The temperature and composition dependence of thermal conductivities of the solid solutions show different features in ZrO_2-rich region and in CeO_2-rich region, which is correlated to the different ionic size between Ce^{4+} and Zr^{4+}. A comparison with the ZrO_2-HfO_2-Y_2O_3 series indicates that both the atomic mass and the ionic size of the tetravalent cations are important factors that influence the temperature and composition dependence of thermal conductivity in the ternary solid solutions.

7.2 Future work

(1) Study the defect structures in ZrO_2-CeO_2-Y_2O_3 solid solutions by high temperature Raman spectroscopy.

The conclusions of Chapter 5 and 6 indicate that both electrical and thermal properties of the ZrO_2-CeO_2-Y_2O_3 solid solutions are closely related to the oxygen vacancy disorder/order at the anion site. Since Raman spectroscopy is sensitive to the anions and it can reflect the vibration modes of the lattice, it could be an effective way to investigate the defect structure in the ternary solid solutions. The relationship between

defect structure and the material properties, especially the thermal conductivity, could be established.

(2) Study the thermal conductivity of YSZ/Pt composites.

The conclusion of Chapter 4 indicates that large interfacial resistance exists when the two components have significantly different elastic properties (e.g., Young's modulus, density, etc.). This leads to the thought of utilizing the YSZ/metal interface to decrease the thermal conductivity of YSZ. Pt is stable at high temperatures and thus is the first candidate metal material. There are two ideal structures of this composite. One is nano-size Pt agglomerations evenly distributed inside the YSZ matrix to generate large amount of interfaces. The other one is Pt segregates inside the YSZ grain boundaries to "strengthen" the grain boundary-phonon scattering. The difficulty of this thought is how to produce dense bulk samples of the above two structures.

(3) Study the thermal conductivity of multilayer TBC system.

TBC has a multilayer structure. Some issues related to the thermal conductivity of the real TBC system, for example, how the bond coat/TGO interface or the bond coat/YSZ interface influences the heat conduction through the TBCs, are still unclear. Finite element modelling can be employed to assist understanding of the experimental results.